

UNIVERSITÀ DEGLI STUDI DI NAPOLI “FEDERICO II”

**Generation and manipulation of laser
beams carrying orbital angular
momentum for classical and quantum
information applications**

by

Ebrahim Karimi

Tutors:

Prof. Lorenzo Marrucci & Prof. Enrico Santamato

Thesis for the Doctor of Philosophy degree

in the

Optics in Soft-Matter

Dipartimento di Scienze Fisiche

November 2009

Declaration of Authorship

I, Ebrahim Karimi, declare that this thesis titled, “Generation and manipulation of laser beams carrying orbital angular momentum for classical and quantum information applications” and the work presented in it are my own. I confirm that:

- This work was done wholly or mainly while in candidature for a research degree at this University.
- No part of this thesis has previously been submitted for a degree or any other qualification at this University or any other institution.
- Where I have consulted the published work of others, this is always clearly attributed.
- Where I have quoted from the work of others, the source is always given. With the exception of such quotations, this thesis is entirely my own work.
- I have acknowledged all main sources of help.

Signed: Ebrahim Karimi

Date: 26 November 2009

“Human subtlety will never devise an invention more beautiful, more simple or more direct than does nature because in her inventions nothing is lacking, and nothing is superfluous.”

Leonardo da Vinci
*An Italian **polymath** (1452 - 1519)*

Abstract

Optics in Soft-Matter

Dipartimento di Scienze Fisiche

Doctor of Philosophy

by [Ebrahim Karimi](#)

Light orbital angular momentum (OAM) has been recognized as a new promising resource for classical and quantum information applications. In contrast to the spin angular momentum, the OAM is an inherently multidimensional. Thus, the information can be encoded in the higher-dimensional OAM alphabets. Recently, Marrucci et al. have invented a new device named q-plate (QP), made of liquid crystal cell patterned in such a way to introduce a topological charge q at the transverse plane, which is able to generate a well-defined values of photon OAM. My research has been aimed at investigating the physics of the QP, of the optical fields that it generates and of its possible applications for optical communication and quantum information. We studied both theoretically and experimentally a novel set of non-orthogonal but over-complete paraxial modes, named Hypergeometric-Gaussian modes, that is typically associated with OAM-carrying optical fields. We have also found the light propagation kernel inside the QP and we have shown analytically that if small losses due to reflection, absorption, and scattering are neglected, the QP can convert the photon spin into OAM with up to 100 % efficiency. We implemented a technique to control the QP optical retardation by tuning the QP temperature. At the optimal temperature, the QP can generate a beam with up to 97% efficiency. Moreover, the OAM state generated by QP can be rotated easily in the 2D OAM Hilbert space by proper manipulation of the input polarization state, a fact which opens a new way of beam shape controlling in MHz scale. We also performed a novel way to encode and read two bits information on the 4D OAM space by using only one QP. Finally, we experimentally demonstrated the transfer of quantum information from spin to OAM and vice versa, including the case of bi-photon states having quantum correlations. Furthermore, by exploiting these quantum information transfer devices, we demonstrated the Hong-Ou-Mandel effect and the optimal quantum cloning with OAM-carrying photons.

Preface

The classical regime of orbital angular momentum of light has been developed significantly during the last three decades with progress in such diverse fields as manipulation of small particles, microfluidic optical pump, astronomy, and classical communications. The quantum applications of light orbital angular momentum has been more recently developing.

In my thesis, I organized the content according to the logical development, rather than separating my own contribution from previous work in distinct chapters. However, in order to clearly indicate where my own work is reported, I added a reference to my papers in the corresponding section's title.

Ebrahim Karimi

27 November 2009, Napoli

Acknowledgements

I wish to thank my supervisors **Prof. Lorenzo Marrucci** and **Prof. Enrico Santamato** for their patience, offering valuable advices and especially giving me a special opportunity to study in Italy. I thank **Dr. Bruno Piccirillo** for his notable advices in the laboratory, and **Dr. Sergei Slusarenko** for his help in laboratory and for reading my thesis.

Many thanks to my professors at the university of Naples “Federico II”: especially **Prof. Salvatore Solimeno** and **Prof. Paolo Aniello** for their notable advise. I must say thanks to a great man that, as a saint spends all his time for all physics students at the university of Naples, **Mr. Guido Celentano**, a man who always embraced all of our requests with lovely smiles.

Also, I must thank all of my friends for creating me a nice, friendly and comfortable environment in the university of Naples “Federico-II”.

Most of all, I thank my wife, **Rahil Golipour** for her practical assistance during my PhD research.

Contents

Declaration of Authorship	i
Abstract	iii
Preface	iv
Acknowledgements	v
List of Figures	viii
List of Tables	x
Abbreviations	xi
Physical Constants	xiii
Symbols	xiv
1 Introduction	1
1.1 Introduction	1
1.2 Angular momentum of light	2
2 Light angular momentum	8
2.1 Introduction	8
2.2 Multipole Radiation and Light angular momentum	9
2.3 Decomposition of the light angular momentum	13
2.4 Angular momentum of the quantized electromagnetic field	15
2.5 Paraxial Wave Equation	17
2.5.1 Paraxial wave equation and decomposition of angular momentum .	17
2.5.2 Paraxial wave equation and its orbital angular momentum eigen-	
states	20
2.5.2.1 Laugerre-Gaussian modes	21
2.5.2.2 Hypergeometric-Gaussian modes (Karimi et al. [13]) . . .	23
2.5.2.3 Hypergeometric-Gaussian type-II modes (Karimi et al.	
[14])	25

3	Generation and detection of the orbital angular momentum of light	29
3.1	Introduction	29
3.2	Spiral phase plate	30
3.3	Cylindrical lenses Mode converter	32
3.4	Pitch-fork hologram and computer generated holograms	36
3.5	q -plate	41
3.5.1	Manufacturing a q -plate	43
3.5.2	Thermal tuning of the q -plate and its characterizations (Karimi et al. [45])	44
3.5.3	q -plate as a mode sorter (Karimi et al. [45])	47
3.5.4	Schemes for generating higher orders of OAM	49
4	The OAM propagation and classical application	50
4.1	Introduction	50
4.2	Outgoing wave from the pitch fork hologram (Karimi et al. [13])	51
4.3	Propagation of wave inside the q -plate (Karimi et al. [46])	56
4.4	OAM Poincarè sphere and geometrical phase (Karimi et al. [53])	66
4.5	Generation of needle beams (Karimi et al. [14])	73
4.6	Classical communication (Slussarenko et al. [64])	76
4.6.1	Experimental setup	77
5	Quantum information application of OAM	79
5.1	Introduction	79
5.2	q -plate: single photon quantum formalism	80
5.3	Holograms and quantum state tomography (Nagali et al. [66])	81
5.4	q -plate as OAM quantum information transfer (Nagali et al. [66])	82
5.4.1	Quantum transferrer from SAM to OAM	84
5.4.2	Quantum transferrer from OAM to SAM	86
5.4.3	Bidirectional transfer SAM-OAM-SAM	87
5.4.4	Manipulation of OAM in the subspace $ m = 4$	89
5.5	Hong-Ou-Mandel effect via OAM (Nagali et al. [32])	90
5.6	OAM quantum cloning (Nagali et al. [33])	94
5.7	q -box (Slussarenko et al. [67])	95
A	Spherical wave solution of scalar wave equation	98
B	Integrals containing confluent hypergeometric functions	101
C	Published articles related to my thesis	103
	Bibliography	105

List of Figures

1.1	SAM and OAM	4
2.1	The $LG_{0,2}$ free space propagation	22
2.2	Intensity pattern of the LG mode	22
2.3	Phase pattern of the LG mode	23
2.4	Intensity pattern of the HyGG modes	25
2.5	Phase pattern of the HyGG modes	26
2.6	HyGG-II intensity pattern	27
2.7	HyGG-II phase pattern	28
2.8	HyGG-II variation	28
3.1	Schematic of a Spiral phase plate illuminated by a TEM_{00} beam and its outgoing wave	30
3.2	Decomposition of the LG and astigmatism HG modes on the HG basis	33
3.3	π -Mode converter	34
3.4	$\pi/2$ -Mode converter	35
3.5	π and $\pi/2$ mode converters analogy	36
3.6	Holograms in order to generate helical beams	37
3.7	Beams generated by a sinusoidal pitch fork holograms	38
3.8	Different type of holograms	39
3.9	q -plate topology for different values of q	42
3.10	The fringes of q -plates sandwiched between two crossed polarizers.	44
3.11	Interference patterns of outgoing beams from the q -plate with planar and spherical TEM_{00} beams.	44
3.12	Setup to measure the STOC efficiency	45
3.13	STOC power	46
3.14	Far-field patterns	47
4.1	The free-air propagation of the outgoing beam from a pitch-fork hologram.	53
4.2	Experimentally observed intensity distributions of the $ HyGG\rangle_{-m,m}$ mode	54
4.3	The experimental ring diameter d of the $ HyGG\rangle_{-m,m}$ mode at fixed plane.	55
4.4	The ratio between the diameter $d(z)$ of the $ HyGG\rangle_{-3,3}$ mode and the $1/e^2$ intensity radius $w(z)$ of the generating TEM_{00} gaussian beam as a function of z	55
4.5	Beating of SAM and OAM	64
4.6	Intensity profile for (a) full STOC (b) no STOC in the 1-plate.	65
4.7	Intensity profile in the far-field beyond the 1-plate after free-air propagation.	66
4.8	The intensity profile of outgoing beams from the q -plate	67

4.9	Experimental setup for generating polarization-controlled linear combinations of LG ₂ beams	68
4.10	Trajectory along the equator of the Poincaré's sphere.	69
4.11	Trajectory along a meridian of the Poincaré's sphere.	69
4.12	A possible closed path over the OAM-Poincaré sphere. The path starts and ends at the pole.	72
4.13	Interference patterns for two different closed trajectories on the Poincaré sphere.	72
4.14	Intensity profile of the longitudinal and radial field components at the focal point of a high numerical aperture lens	74
4.15	Density plots of intensity distribution for radial and longitudinal components.	75
4.16	Classical communication setup	78
5.1	Schematic of q -plate action	80
5.2	Patterns of the holograms used for quantum tomography.	82
5.3	Schematic representation of the experimental setup	84
5.4	Experimental density matrices ρ measured for the output of the $\pi \rightarrow o_2$ qubit transfer.	85
5.5	Experimental density matrices ρ measured for the output of the $o_2 \rightarrow \pi$ qubit transfer.	87
5.6	Experimental density matrices ρ measured for the output of the $\pi \rightarrow o_2 \rightarrow \pi$ qubit transfer.	88
5.7	Experimental density matrices measured in the OAM basis $\{ +4\rangle, -4\rangle\}$	90
5.8	Patterns of the holograms used for quantum tomography.	92
5.9	Experimental Hong-Ou-Mandel effect via holograms.	93
5.10	Experimental setup of the cloning process of the OAM states.	95
5.11	Experimental Hong-Ou-Mandel effect.	96
5.12	The scheme of the q -box	97

List of Tables

2.1	Classification of modes families.	20
3.1	Ideal efficiency of different types of grating and different kind of holograms.	40
3.2	The QP's efficiency as a mode sorter.	49
4.1	The outgoing beam power spectrum from a pitch fork hologram in the LG modes basis. ℓ indicates the topological charge of hologram and q shows the LG radial index number.	53
4.2	Four possible combinations of QWP angles and their corresponding beam's OAM values.	78
5.1	Fidelity values between the experimental states generated by the $\pi \rightarrow o_2$ transferrer and the theoretical ones expected after the conversion in the OAM degree of freedom of the qubit initially encoded in the polarization.	85
5.2	Fidelity values between the experimental states generated by the $o_2 \rightarrow \pi$ transferrer and the theoretical ones expected after the conversion in polarization degree of freedom of the qubit initially encoded in the OAM.	86
5.3	Fidelity values between the input and output states for the bidirectional $\pi \rightarrow o_2 \rightarrow \pi$ transferrer.	88
5.4	Fidelity values between the expected and the experimental states generated by the $\pi \rightarrow o_4$ transferrer.	90

Abbreviations

AM	A ngular M omentum
BBO	β - B arium B Orate
BG	B essel - G aussian
CGH	C omputer G enerated H ologram
EM	E lectro M agnetic
GOA	G eometric O ptics A pproximation
HG	H ermite - G aussian
HOM	H ong O u M andel
HWP	H alf W ave P late
HyG	H yper G eometric
HyGG	H yper G eometric - G aussian
LC	L iquid C rystal
LCD	L iquid C rystal D isplay
LG	L augerre - G aussian
OAM	O rbital A ngular M omentum
PC	P ockel C ell
PWE	P araxial W ave E quation
QP	Q - P late
QWP	Q uarter W ave P late
SAM	S pin A ngular M omentum
SLM	S patial L ight M odulators
SPCM	S ingle P hoton C ounter M odule
SPDC	S pontaneous P arametric D own C onversion
SPP	S piral P hase P late
STOC	S AM- T o- O AM C onversion

UUG **U**niversal **U**nitary **G**ate

Physical Constants

Reduced Planck's Constant	\hbar	=	1.0544×10^{-34}	J s
Speed of Light	c	=	2.9979×10^8	ms ⁻¹
Vacuum Permittivity	ϵ_0	=	8.8541×10^{-12}	AsV ⁻¹ m ⁻¹
Vacuum Permeability	μ_0	=	1.2566×10^{-6}	VsA ⁻¹ m ⁻¹

Symbols

A	magnetic vector potential	Vsm^{-1}
B	inductive magnetic field	$\text{NC}^{-1}\text{m}^{-1}\text{s}^{-1}$
D	electric displacement vector	Cm^{-2}
E	electric field	Vm^{-1}
H	magnetic field	Am^{-1}
k	wave vector	m^{-1}
L	orbital angular momentum	Nms
<i>P</i>	power	$\text{W} (\text{Js}^{-1})$
<i>q</i>	topological charge	dimensionless
S	spin angular momentum	Nms
w_0	beam waist	m
z_R	Rayleigh parameter	m
λ	wavelength	m
Φ	scalar potential	V
ω	angular frequency	rads^{-1}

To my wife
Rahil
and my parents
Mohammad and Khadijeh

Chapter 1

Introduction

“If you are going to be a physicist, you will have a lot to study: two hundred years of the most rapidly developing field of knowledge that there is. So much knowledge, in fact, that you might think that you cannot learn all of it in four years, and truly you cannot.” [1].

Richard P. Feynman

1.1 Introduction

It is almost impossible to mention whole work on the orbital angular momentum in this thesis and surely I have missed many important works in this field. I apologize to those researches whose works I did not mention here!

As an introduction to my thesis, I would like to start with my feeling and my experience about light. My first touch to light was at primary school where a small dark and white structures (nowadays known as a fringes for me) were a surprising toys when I tried to close my “thumb” and “index finger”. I learnt that light is one of the essential keys to having life on the universe and without light is impossible to live on the earth. The reflection and spectrum were a nice play to produce some nice structures at home with mirrors and plastic pens. After my B.Sc., I had a *magic-like* feeling for a light as an essential particle which can change the behavior when one is going to detect or propagate it. A massless particle or an electromagnetic wave! Photon was an attractive concept in my mind in such a way that I changed my field from a mathematical physicist to an optician physicist. At the beginning of my new research field, it was surprising to see that light look like a particle has rotational behavior. More exciting result were

to see that its properties almost 100% are predicted by quantum mechanics. I was so excited to see that after many calculations and projections over many bases when I tried to do the quantum tomography. It seemed to me that photons have already perused my calculations and tried to follow the calculations precisely.

1.2 Angular momentum of light

From both classical (wave) and quantum (particle) point of view light has mechanical properties. Kepler proposed that the tail of comets are due to the light radiation pressure of the sun and he could prove it by observing the tail and the sun positions for different comets (of course, there is another tail due to the electrostatic interaction of ionic particles of the comets and the sun which is not our interest in this case). The first quantitative development on the electromagnetism theory has been done by Maxwell which nowadays are still using by physicists. Maxwell has proved that a light beam is made of a transverse time-position oscillating orthogonal electric and magnetic fields which are traveling in the space with speed of c [2]. Poynting shows that an electromagnetic wave also carries linear momentum and well-defined energy flux which passes through a transverse plane. This quantity is equal to $\mathbf{E} \times \mathbf{H}$ and is a linear momentum per unit of volume. From quantum point of view, each photon carries a well-defined linear momentum which is equal to $\hbar\mathbf{k}$, where \hbar and \mathbf{k} are the reduced Planck's constant and photon wave vector, respectively. The angular momentum at the position of \mathbf{r} with respect to beam axes, then, is given classically by $\mathbf{r} \times (\mathbf{E} \times \mathbf{H})$ and quantum mechanically by $\mathbf{r} \times \hbar\mathbf{k}$. Poynting in analogy with the wave notation associated to a line of dots marked on a rotating cylindrical shaft showed that a circularly polarized light beam must carry angular momentum. He showed that a circularly polarized beam carries a flux of angular momentum equal to $\frac{\lambda}{2\pi} u$, where u and λ are the average energy density and the beam wavelength, respectively [3]. In the quantum formalism, $u = n\hbar\omega$, where n is the number of photon per unit volume [4]. So, a circularly polarized beam carries angular momentum of \hbar per photon.

Twenty years after Poynting dead, Beth has experimentally proved that a circularly polarized beam carries a finite angular momentum and he measured corresponding torque over a quarter wave plate with a help of a suspended mirror [5].

The polarization (spin) angular momentum is not the only type of angular momentum which an electromagnetic wave can carry. Photon looks like all particles and can also carry orbital angular momentum. In fact, a transverse component of linear momentum can produce an angular momentum in the direction of propagation. A careful examination of angular momentum shows that the total angular momentum can be divided in sum of two different angular momenta; spin and angular momentum [4].

Humblet showed that the total angular momentum of an electromagnetic wave can be decomposed into two terms

$$S_i = \frac{1}{2\mu_0\omega} \sum_{j,k} \int E_j^* (-i\epsilon_{ijk}) E_k d^3\mathbf{r},$$

$$L_i = \frac{1}{2\mu_0\omega} \sum_j \int E_j^* (-i\mathbf{r} \times \nabla)_i E_j d^3\mathbf{r}$$

The first term, named spin angular momentum, is completely independent on the frame coordinate and it just depends on the electric field. The second term, instead, is frame dependent and in analogy to the quantum mechanics is called orbital angular momentum. Later on it has been understood that the z-component of OAM in the paraxial regime is also independent of the frame origin [6]. SAM is independent of the coordinate and is only depend on the electric field. In contrast, as we see the OAM in analogy to quantum mechanics is frame dependent (in general). The z-component of angular momentum is our interest here and it can be shown that the z-component of SAM is $S_z \propto (E_L^2 - E_R^2)$ and the z-component of OAM is $L_z \propto -i(E_L^* \partial_\phi E_L + E_R^* \partial_\phi E_R)$, where $E_{L,R}$ are corresponding to electric field of *Left* and *Right* circular polarizations. The SAM is associated to the vectorial property of electric field. In the quantum point of view, Left or Right circularly polarized photon carry angular momentum of $+\hbar$ or $-\hbar$ in the direction of propagation, respectively (see figure 1.1-(a)). The OAM, instead, is independent of the vectorial property of the field and depends on the optical phase front. A beam with helical phase front $e^{i\ell\phi}$ carries OAM of $\ell\hbar$ per photon in the direction of propagation (see figure 1.1-(b)). Apart some similarities between SAM and OAM, they are conceptually different. Nevertheless in the case of light waves SAM and OAM can be classically distinguished only in the paraxial approximation. In the general case, instead, it is impossible to distinguish the SAM and OAM of an electromagnetic field in vacuum (in absence of matter). The difference arises only when are interacting with matter. Let us consider a small particle located in the waist of a light beam possessing SAM and OAM together. The SAM part of the angular momentum causes a rotation of the particle around its own axis and the OAM part causes a rotation around the beam axis. An identification of OAM is suggested also by the analogy between paraxial optics and quantum mechanics where the Schrödinger wave equation is identical to the paraxial wave equation (PWE) just by replacing time t by z . In this case the operator of OAM can be written in the form of $L_z = -i\frac{\partial}{\partial\phi}$ in units of \hbar . A physically realizable example of beam which carries OAM is a Laugerre-Gaussian (LG) beam in the paraxial regime. However, LG beams are not the only eigenstates of OAM and there are several families of the PWE which are eigenstate of OAM such as; Mathieu [7], Bessel [8], Bessel-Gaussian [9], Ince-Gaussian [10], Circular [11], Hypergeometric [12], Hypergeometric-Gaussian type-I and type-II beams [13, 14]. Allen and his coworkers

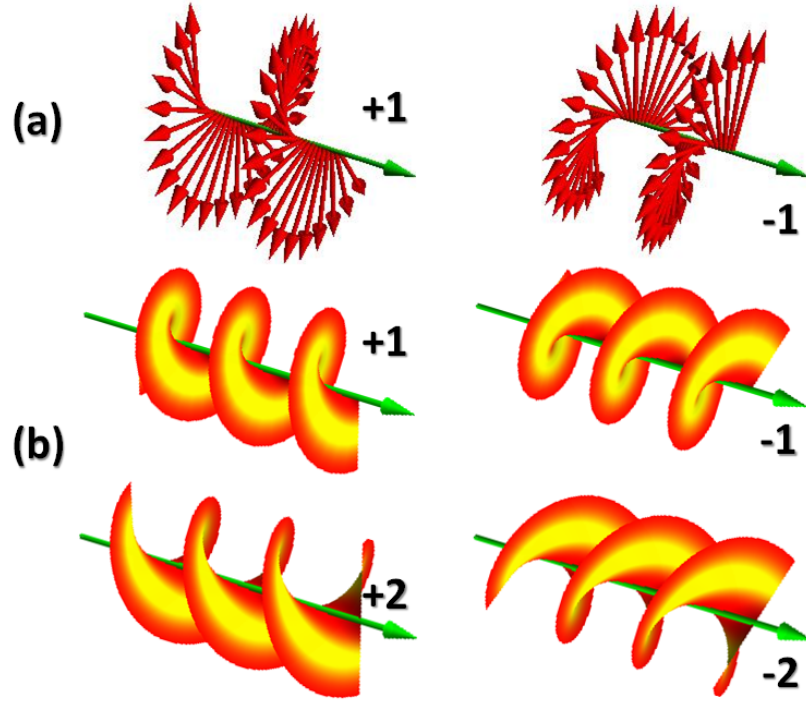


FIGURE 1.1: (a) The optical field structure of Left and Right circularly polarized beam, respectively. (b) The helical phase front of beams carrying different values of OAM.

were the first group to show that a beam with a helical phase front has a definite value of OAM in the direction of propagation [15]. They used a set of proper aligned cylindrical lenses to convert Hermite-Gaussian modes into LG modes. The LG and HG modes are two important solutions of the PWE in cylindrical and cartesian coordinates, respectively [16]. Both LG and HG are complete set of modes in their appropriate coordinates. So, there is a possible expansion of LG modes in the HG basis and *vice versa*. In a similar way, diagonal HG modes can be expanded in the HG basis too. The only difference between diagonal HG and LG mode expansion is the relative phase factor between each terms of expansion coefficients. If an astigmatic system introduces a relative phase factor between the expansion coefficients, the diagonal HG mode will be converted into the LG modes.

There is another possible way to produce a beam which posses OAM. Beijersbergen et al used a new device, called spiral phase plate (SPP), to imprint helical structure over impinging beam [17]. SPP is an optical element made of a glass with an optical thickness that increases with azimuthal angle, such that, upon transmission, an incident plane wave emerges with a helical phase front. In order to having a proper topological charge and optical retardation, the SPP is keeping inside a liquid with a refractive index close to the SPP material. When the final increase of the optical thickness is tuned to

multiples of λ , TEM_{00} beam transfers directly into a beam with a well-defined value of OAM.

Holography is also another way to produce a beam with OAM [18]. Let us make an interference of a tilted helical beam with a plane-wave reference beam. The interference pattern is called pitch-fork hologram. One can use this hologram to generate helical modes (a beam which carries OAM). When the pitch-fork hologram is illuminated by a TEM_{00} beam part of power is diffracted. In the first two diffraction orders we have a helical beam with opposite OAM values. Due to diffraction process, hologram unlike Mode converters and SPP has a low efficiency. However, owing to the presence of commercially programable spatial light modulators (SLM) holograms are now widely used to generate and detect OAM in real time.

Recently, a novel method has been introduced by Marrucci et al. in which one can introduce a topological charge in the phase front of a beam depending on the initial polarization state of the beam [19]. The heart of this process is an anisotropic birefringent plate made of liquid crystal with a well-defined topological charge in the transverse plane, named q -plate. So, when a circularly polarized beam traverses the plate an overall phase equal to twice of plate topological charge is introduced in the beam phase front and the polarization of the input beam is flipped. Therefore, at the output we gain an value of OAM. When the polarization of the input beam changes the values of the output OAM is reversed accordingly.

All OAM generators, especially SPP, pitch-fork hologram and q -plate do not produce a pure LG mode [20]. The output beam, indeed, is a superposition of infinite LG mode with a fixed values of OAM and different radial number. We have shown experimentally and theoretically that typical emerging beams from a pitch-fork hologram are particular solutions of the PWE and the transverse profile of optical field given by a confluent-hypergeometric and gaussian functions [13]. This set of new PWE solution are overcomplete, non-orthogonal set of modes. This situation can be extended to the case of non-truncated SPP [21]. We have also solved the Maxwell wave equation inside the q -plate and we showed that for a good paraxial beam and low birefringent material there is an analytical solution which shows the spin-to-orbit conversion and foresees the emerging beam profile for any plate optical retardation of the plate.

Sato et al. were the first group to use the OAM to rotate and align microscopic objects [22]. The first explicit demonstration of the transfer of light angular momentum to microscopic objects, however, was performed by optical tweezers by Higurashi and coworkers on (1994) [23].

In 2002 Padgett and his coworkers showed experimentally that for particles held away from the axis of beam, the SAM and OAM components of the light angular momentum

behaved differently. Transfer of SAM to the particles resulted in a spinning rotation of particle about its own axis, while transfer of OAM caused an orbiting rotation of the particle around the beam axis where the phase singularity is located [24]. When acting on a superposition of smaller particles this OAM transfer created a swingling flow or pumping action. The torque due to the SAM transfer is limited to \hbar per photon while by increasing the beam winding number the OAM transfer torque can be increased at will. Leach and coworkers, on (2006), used the SAM conservation to increase the torque due to SAM transferring on two half wave micro spheres [25]. They were able to make an optically driven pump for microfluidics.

SAM is inherently binary and only a bit of information can be encoded in the beam SAM. Instead, OAM dimensionality is infinite. So, in the OAM space more alphabets are available. More recently, Gibson et al. used the multi-dimensionality of OAM to encode information for free space telecommunication [26].

Apart classical applications, SAM and OAM have quantum perspective. 30 years ago, Aspect and coworkers showed that AM of two photons can be entangled. In such way that a measurement on the polarization of one of the photons appears to modify instantaneously the polarization state of the other photon [27]. This process can be done irrespective of the distance between the particles. The polarization of the entangled photon pair has the following form

$$|\psi\rangle = \frac{1}{\sqrt{2}} (| \circ \rangle_i | \circ \rangle_s + | \circ \rangle_i | \circ \rangle_s)$$

where $| \circ \rangle$, $| \circ \rangle$ denote the left and right polarization states, and i , s are the idler and signal photons. They experimentally demonstrated a violation of the Bell's inequality on the entangles pairs of photons. The evidence of this experiments strongly supports quantum mechanics and provides convincing existence of entangled states. SAM entangled states are the basis of many impressive quantum processes such as; quantum teleportation, quantum cloning, quantum communication, quantum cryptography and ... [28-30].

The entanglement of OAM in photon pair has been demonstrated in spontaneous parametric down conversion (SPDC) by Zeilinger and coworkers on (2001) [31]. The SPDC can generate an entangled state over whole OAM states;

$$|\psi\rangle = \frac{1}{\sqrt{2}} \sum_{\ell=-\infty}^{+\infty} (| -\ell \rangle_i | \ell \rangle_s + | \ell \rangle_i | -\ell \rangle_s)$$

where $| \ell \rangle$ denotes the OAM state. In this experiment signal and idler photons were projected over a well known OAM state by means of computer generated holograms

and single mode optical fibers. This experiment confirmed that OAM of light is a quantum variable associated with a single photon. Recently, Leach et al. rebuilt the same experiment with a dynamically changeable holograms. They were able to violate the Bell's inequality for two photons entangled on the OAM state [32].

Recently, we were able to show experimentally that two identical photons will bunch where they have the same value of OAM. This photon bunching has been observed in a beam splitter and also in terms of detecting via a proper holograms [33, 34]. We were able to destroy the coalescence of photons just by making a delay between signal and idler photons.

Chapter 2

Light angular momentum

2.1 Introduction

The main traits of the electromagnetic wave can be explained via the four important laws that James Clerk Maxwell (a Scottish scientist 1831 – 1879) collected and corrected them in 19 century; Coulumb's law ($\nabla \cdot \mathbf{D} = \rho$), Gauss law for the magnetism which comes from the Biot-Savar law ($\nabla \cdot \mathbf{B} = 0$), Farady's law ($\nabla \times \mathbf{E} = -\frac{\partial \mathbf{B}}{\partial t}$) and Ampere's law ($\nabla \times \mathbf{H} = \mathbf{J} + \frac{\partial \mathbf{D}}{\partial t}$). Maxwell in a smart way collected them and especially corrected the Ampere's law by adding the drift current, the last term, to the free current source.

In this chapter based on the Maxwell's equations, we show that the electromagnetic waves possess three important quantities; energy, linear momentum and angular momentum as the same as a particle has. Then, we focus our attention to the electromagnetic angular momentum of a multipole radiation. Indeed, the light angular momentum can be divided into two parts: spin angular momentum (SAM) which is position independent and orbital angular momentum (OAM) which depends on the position. After that, we show that these definitions can also be extended to the quantized light angular momentum field. The SAM and OAM of a beam are also written in terms of creation and annihilation operators. Finally, we consider a subfamily of the scalar wave equations, named paraxial wave equations (PWE). A general solution of this PWE is presented which covers a large families of PWE such as, Laguerre-Gauss, elegant Laguerre-Gauss, Bessel, Hypergeometric, Hypergeometric-Gauss type I, Hypergeometric-Gauss type II,

2.2 Multipole Radiation and Light angular momentum

The full description of the electromagnetic wave can be done by Maxwell's equations; the Gauss's law for electric and magnetic field, Maxwell - Faraday's equation and Ampère's law. The Maxwell's equations in the vacuum, in the absence of free charges and currents, are given by;

$$\left\{ \begin{array}{l} \nabla \cdot \mathbf{E} = 0 \\ \nabla \cdot \mathbf{B} = 0 \\ \nabla \times \mathbf{E} = -\frac{\partial \mathbf{B}}{\partial t} \\ \nabla \times \mathbf{B} = \epsilon_0 \mu_0 \frac{\partial \mathbf{E}}{\partial t} \end{array} \right. \quad (2.1)$$

where \mathbf{E} , \mathbf{B} , ϵ_0 and μ_0 are the electric field, magnetic field, permittivity and permeability of free space, respectively [2]. Note that we have chosen **SI** system in this section. Without loss of the generality, by using the Fourier theorem, we can express electric and magnetic field as

$$\left\{ \begin{array}{l} \mathbf{E}(\mathbf{x}; t) \\ \mathbf{B}(\mathbf{x}; t) \end{array} \right\} = \int_{-\infty}^{+\infty} \left\{ \begin{array}{l} \mathbf{E}(\mathbf{x}; \omega) \\ \mathbf{B}(\mathbf{x}; \omega) \end{array} \right\} e^{-i\omega t} dt \quad (2.2)$$

where ω is the frequency of electromagnetic field. By substituting Eq. (2.2) in the Maxwell's equations we will have obtain

$$\left\{ \begin{array}{l} \nabla \cdot \mathbf{E} = 0 \\ \nabla \cdot \mathbf{B} = 0 \\ \nabla \times \mathbf{E} = i\omega \mathbf{B} \\ \nabla \times \mathbf{B} = -\frac{i\omega}{c^2} \mathbf{E} \end{array} \right. \quad (2.3)$$

where c is the speed of light in vacuum and is equal to $1/\sqrt{\epsilon_0 \mu_0}$. One can easily show that electric and magnetic fields obey vector Helmholtz's equation.

$$(\nabla^2 + k^2) \left\{ \begin{array}{l} \mathbf{E} \\ \mathbf{B} \end{array} \right\} = \mathbf{0} \quad (2.4)$$

with constraints $\nabla \cdot \mathbf{E} = 0$ and $\nabla \cdot \mathbf{B} = 0$. Each equation is made of three scalar Helmholtz's equations. The solution of the scalar Helmholtz's equation in the spherical coordinates is given in Appendix (A). For our purpose it is convenient to avoid solving these three scalar equations. So, I prefer to solve the vectorial Helmholtz's equation rather than scalar one. There are several methods to achieve the right solutions of vectorial Helmholtz's equation. I choose the Casimir's way [35]. For a well-behaved

vector field, \mathbf{A} , the following equation is valid

$$\nabla^2(\mathbf{x} \cdot \mathbf{A}) = \mathbf{x} \cdot (\nabla^2 \mathbf{A}) + 2\nabla \cdot \mathbf{A} \quad (2.5)$$

By using this equation, one can show that $\mathbf{x} \cdot \mathbf{E}$ and $\mathbf{x} \cdot \mathbf{B}$ also satisfying the scalar wave equation

$$(\nabla^2 + k^2) \begin{Bmatrix} \mathbf{x} \cdot \mathbf{E} \\ \mathbf{x} \cdot \mathbf{B} \end{Bmatrix} = \mathbf{0} \quad (2.6)$$

We divided the general solution into two cases; transverse electric (TE) and transverse magnetic (TM) fields. These two set of solutions together are general and complete. The general solution of equation (2.6) is a given in Appendix (A). For the TE field, we may consider

$$\mathbf{x} \cdot \mathbf{B}_{l,m}^M = \left(A_{l,m}^{(1)} h_l^{(1)}(kr) + A_{l,m}^{(2)} h_l^{(2)}(kr) \right) Y_{l,m}(\theta, \phi) \quad (2.7)$$

and

$$\mathbf{x} \cdot \mathbf{E}_{l,m}^M = 0 \quad (2.8)$$

where $A_{l,m}^{(1,2)}$ are the constant coefficients, $h_l^{(1,2)}$ are the Hankel functions, and $Y_{l,m}(\theta, \phi)$ is the spherical harmonic (see Appendix A). From the Maxwell's 3rd equation, we can show that

$$\mathbf{L} \cdot \mathbf{E}_{l,m}^M = \omega \left(A_{l,m}^{(1)} h_l^{(1)}(kr) + A_{l,m}^{(2)} h_l^{(2)}(kr) \right) Y_{l,m}(\theta, \phi) \quad (2.9)$$

where $\mathbf{L} = \frac{1}{i} \mathbf{x} \times \nabla$ is the angular momentum operator.

In equation (2.9), $\mathbf{L} \cdot \mathbf{E}_{l,m}^M$ is given in terms of the spherical harmonic with a given l and m . Furthermore, angular momentum's operator does not change the l index of spherical harmonic and it acts only on the azimuthal index, i.e. m . So, we can conclude that

$$\begin{aligned} \mathbf{E}_{l,m}^M &= \omega \left(A_{l,m}^{(1)} h_l^{(1)}(kr) + A_{l,m}^{(2)} h_l^{(2)}(kr) \right) Y_{l,m}(\theta, \phi) \\ \mathbf{B}_{l,m}^M &= -\frac{i}{\omega} \nabla \times \mathbf{E}_{l,m}^M \end{aligned} \quad (2.10)$$

The same analogy can be used to find the TM modes. A possible solution for the TM modes is

$$\mathbf{B}_{l,m}^E = \omega \left(B_{l,m}^{(1)} h_l^{(1)}(kr) + B_{l,m}^{(2)} h_l^{(2)}(kr) \right) Y_{l,m}(\theta, \phi)$$

$$\mathbf{E}_{l,m}^E = \frac{ic^2}{\omega} \nabla \times \mathbf{B}_{l,m}^M \quad (2.11)$$

where $A_{l,m}^{(1,2)}$ are the constant coefficients. Therefore, we can write the general solution to the Maxwell equations

$$\begin{aligned} \mathbf{B} &= \sum_{l,m} \left(a_{E(l,m)} f_l(kr) \mathbf{X}_{l,m} - \frac{i}{\omega} a_{M(l,m)} \nabla \times g_l(kr) \mathbf{X}_{l,m} \right) \\ \mathbf{E} &= \sum_{l,m} \left(\frac{ic^2}{\omega} a_{E(l,m)} \nabla \times f_l(kr) \mathbf{X}_{l,m} + a_{M(l,m)} g_l(kr) \mathbf{X}_{l,m} \right) \end{aligned} \quad (2.12)$$

where $a_{E(l,m)}$, $a_{M(l,m)}$ are specifying the electric and magnetic multipole strength which are determined by the source and boundary conditions, $f_l(kr) = A_{l,m}^{(1)} h_l^{(1)}(kr) + A_{l,m}^{(2)} h_l^{(2)}(kr)$ and $g_l(kr) = B_{l,m}^{(1)} h_l^{(1)}(kr) + B_{l,m}^{(2)} h_l^{(2)}(kr)$ are superposition of Henkel's functions (see appendix A). $\mathbf{X}_{l,m}$ is the vector spherical harmonic with following orthogonal property

$$\int \mathbf{X}_{l,m} \cdot \mathbf{X}_{l',m'}^* d\Omega = \delta_{l,l'} \delta_{m,m'} \quad (2.13)$$

As we have already discussed the EM waves possess energy, linear momentum and angular momentum. We use multipole field radiation Eq. (2.12) to calculate energy and angular momentum carried by the radiation. The energy and angular momentum densities of the EM fields are given by the following well-known formulas;

$$\begin{aligned} u &= \frac{1}{2} \left(\epsilon_0 E^2 + \frac{1}{\mu_0} B^2 \right) \\ \mathbf{j} &= \frac{1}{\mu_0} (\mathbf{r} \times (\mathbf{E} \times \mathbf{B})) \end{aligned} \quad (2.14)$$

For harmonically oscillating fields, e.g. monochromatic field, the time averaged energy and angular momentum densities are

$$\begin{aligned} \langle u \rangle &= \frac{1}{4} \left(\epsilon_0 E^2 + \frac{1}{\mu_0} B^2 \right) \\ \langle \mathbf{j} \rangle &= \frac{1}{2\mu_0} (\mathbf{r} \times (\mathbf{E} \times \mathbf{B}^*)) \end{aligned} \quad (2.15)$$

where $\langle \rangle$ denotes the time average. Now, we are considering two spherical shells with radius r and $r + dr$ in the radiation zone, i.e. $kr \gg 1$. The radiation energy and angular momentum in between these shells are equal to

$$\frac{dU}{dr} = \frac{\mu_0}{2k^2} \sum_{l,m} (|a_{E(l,m)}|^2 + |a_{M(l,m)}|^2)$$

$$\begin{aligned} \frac{d\mathbf{J}}{dr} &= \frac{\mu_0}{2\omega k^2} \Re \sum_{l,m,l',m'} \left\{ \left(a_{E(l,m)} a_{E(l',m')}^* + a_{M(l,m)} a_{M(l',m')}^* \right) \int (\mathbf{L} \cdot \mathbf{X}_{l',m'})^* \mathbf{X}_{l,m} d\Omega \right. \\ &\quad \left. + i^{l-l'} \left(a_{M(l,m)} a_{E(l',m')}^* - a_{M(l',m')}^* a_{E(l,m)} \right) \int (\mathbf{L} \cdot \mathbf{X}_{l',m'})^* \mathbf{n} \times \mathbf{X}_{l,m} d\Omega \right\} \quad (2.16) \end{aligned}$$

where $\mathbf{n} = \frac{\mathbf{r}}{r}$ is a unit vector in the radial direction. As we expected, the total energy is an incoherent superposition over all multipoles strength. The first term in the angular momentum expression is given by the sum of the electric and magnetic multipoles separately. The second term is an interference between electric and magnetic multipoles. It can be shown that the interference term between electric and magnetic multipole appears for integer l values differing by one. This “golden-like” rule can be shown also by using the parity properties of the multipoles radiation.

Now, we pass to discuss some issues of angular momentum. Let us consider a purely transverse electric field with a fixed l number and superposition over all m multipoles. For such kind of wave the energy is

$$\frac{dU}{dr} = \frac{\mu_0}{2k^2} \sum_m |a_{E(l,m)}|^2 \quad (2.17)$$

and angular momentum components are given

$$\begin{aligned} \frac{dJ_x}{dr} &= \frac{\mu_0}{4\omega k^2} \Re \sum_m \left(\sqrt{(l-m)(l+m+1)} a_{E(l,m+1)}^* + \sqrt{(l+m)(l-m+1)} a_{E(l,m-1)}^* \right) a_{E(l,m)} \\ \frac{dJ_y}{dr} &= \frac{\mu_0}{4\omega k^2} \Im \sum_m \left(\sqrt{(l-m)(l+m+1)} a_{E(l,m+1)}^* - \sqrt{(l+m)(l-m+1)} a_{E(l,m-1)}^* \right) a_{E(l,m)} \\ \frac{dJ_z}{dr} &= \frac{\mu_0}{2\omega k^2} \sum_m m |a_{E(l,m)}|^2 \quad (2.18) \end{aligned}$$

where \Re and \Im denote the *real* and *imaginary* part of the expression, respectively. It is clear that just the z -component of angular momentum for a given l has a simple form. If we fix m , i.e. for a pure multipole mode, the transverse components of angular momentum are zero while the z -component is equal to

$$\frac{dJ_z}{dr} = \frac{m}{\omega} \frac{dU}{dr} \quad (2.19)$$

This shows that, for a pure multipole mode, the amount of z -component of the angular momentum is proportional to the amount of energy with a coefficient which is proportional to the azimuthal number of the multipole mode. Moreover, Eq. (2.19) has a simple quantum interpretation: the radiation from a multipoles of order (l, m) carries $m\hbar$ unit of z -component of angular momentum per photon. We would expect from the quantum theory that the ratio of square of total angular momentum of EM wave to the

square of energy must be

$$\frac{J^{(q)^2}}{U^2} = \frac{l(l+1)}{\omega^2} \quad (2.20)$$

But, from Eq.(2.18) can be seen easily that for a pure (l, m) multipoles mode the classical value is

$$\frac{J^{(c)^2}}{U^2} = \frac{m^2}{\omega^2} \quad ! \quad (2.21)$$

This difference lies on the quantum nature of the EM field for a photon. If the z -component of the angular momentum of a single photon is known precisely, the uncertainly principle requires that the other components of angular momentum must be uncertain with a mean square values such the Eq. (2.20) holds. On the other hand, for a radiation state containing many photons the mean square values of the transverse components of angular momentum can be made negligible compared to the square of the z -component. It can be shown, in fact, that for a (l, m) multipoles field containing N photons we have hence

$$\frac{J^{(q)}(N)^2}{U(N)^2} = \frac{Nm^2 + Nl(l+1) - m^2}{N\omega^2} \quad (2.22)$$

This expression covers the classical (2.21) (N large) and quantum (2.20) behavior of angular momentum [36].

2.3 Decomposition of the light angular momentum

It is a common feature of quantum mechanics that angular momentum can be naturally decomposed into SAM an OAM part. The two Gauss laws for the electric and magnetic fields allow us to write the electromagnetic field in terms of a scalar and vector potential [2].

$$\begin{cases} \mathbf{E} = -\nabla\Phi - \frac{\partial\mathbf{A}}{\partial t} \\ \mathbf{B} = \nabla \times \mathbf{A} \end{cases} \quad (2.23)$$

where Φ is the scalar and \mathbf{A} is the vector potential. Due to the gauge freedom, \mathbf{A} (or Φ) can be chosen in such away that obeys the radiation gauge (Coulomb's gauge), i.e. $\nabla \cdot \mathbf{A} = 0$ and $\Phi = 0$, The electromagnetic field, then, can be rewritten

$$\begin{cases} \mathbf{E} = -\frac{\partial\mathbf{A}}{\partial t} \\ \mathbf{B} = \nabla \times \mathbf{A} \end{cases} \quad (2.24)$$

Substituting these field in terms of vector potential into the classical expression of angular momentum and expanding the vector triple product we have

$$J_i = \frac{1}{\mu_0} \epsilon_{i,j,k} \int A_j \dot{A}_k d^3\mathbf{r} + \frac{1}{\mu_0} \epsilon_{i,j,k} \int x_j \partial_k (\dot{A}_p) \dot{A}_p d^3\mathbf{r} \quad (2.25)$$

where $\epsilon_{i,j,k}$ is the Levi-Civita semi tensor, and \dot{A} denotes the partial time derivative of A . The first term obviously is independent of the coordinate. The second term is frame dependent, in contrast. The second term, however, has the quantum orbital angular momentum operator form, i.e. $L_i = \epsilon_{i,j,k} x_j \partial_k$. Therefore, we may decompose the light angular momentum into two parts of the SAM and OAM;

$$\mathbf{J} = \mathbf{S} + \mathbf{L} \quad (2.26)$$

where

$$\begin{aligned} \mathbf{S} &= \frac{1}{\mu_0} \int \mathbf{A} \times \dot{\mathbf{A}} d^3\mathbf{r} \\ \mathbf{L} &= \frac{1}{\mu_0} \sum_{i=x,y,z} \int A_i (\mathbf{r} \times \nabla \dot{A}_i) d^3\mathbf{r} \end{aligned} \quad (2.27)$$

This decomposition is not the unique representation of SAM and OAM. Furthermore, \mathbf{A} vector is not physically measurable quantity, and it is not unique and any $\mathbf{A} + \nabla\chi$ gives the same electromagnetic fields. So, these SAM and OAM are obviously not gauge invariant. In the following, we mention other two different angular momentum decompositions; Humblet and standard decomposition of optical angular momentum which are the closest to what people could measure in practice [37–40]. Humblet replaced the magnetic field in terms of electric field curl, via Faraday's law Eq. (2.3), on the angular momentum expression and he showed that it can be rewritten as

$$\begin{aligned} S_i &= \frac{1}{\mu_0} \int E_j^* (-i\epsilon_{i,j,k}) E_k d^3\mathbf{r} \\ L_i &= \frac{1}{\mu_0} \sum_{j=x,y,z} \int E_j^* (-i\mathbf{r} \times \nabla)_i E_j d^3\mathbf{r} \end{aligned} \quad (2.28)$$

In this form the OAM is strictly similar to the quantum mechanics one where the OAM operator is sandwiched between two wave functions, i.e. electric field. The SAM is appropriately named. It is independent on the frame coordinates and is only dependent on the optical field. Moreover, the operator inside parenthesis ($\Sigma_i = -i\epsilon_{i,j,k}$) is the spin 1 particle operator. The Humblet decomposition explicitly depends on the electric field and vector potential does not play any role here. So, it is obviously gauge invariant.

In the standard decomposition, the magnetic field is replaced by the curl of the vector potential (see 2.24), instead of the Fraday's law. Then

$$\begin{aligned} S_i &= \frac{1}{\mu_0} \int E_j^* (\epsilon_{i,j,k}) A_k d^3 \mathbf{r} \\ L_i &= \frac{1}{\mu_0} \sum_{j=x,y,z} \int E_j^* (-i \mathbf{r} \times \nabla)_i A_j d^3 \mathbf{r} \end{aligned} \quad (2.29)$$

This decomposition also is gauge invariant. To show that it is convenient to write electromagnetic fields and vector potential in terms of longitudinal and transverse parts. The gauge transformation, then, is given

$$\begin{aligned} \mathbf{A}_{\parallel} &\rightarrow \mathbf{A}_{\parallel} + \nabla \chi \\ \mathbf{A}_{\perp} &\rightarrow \mathbf{A}_{\perp} \end{aligned} \quad (2.30)$$

where \mathbf{A}_{\perp} and \mathbf{A}_{\parallel} denote the transverse and longitudinal part of the vector potential. The total angular momentum also can be divided into two transverse and longitudinal parts. The longitudinal part can be attributed to the angular momentum of the charged particles in the source of the field. The transverse part is equal to

$$\mathbf{J}_{\perp} = \frac{1}{\mu_0} \int \mathbf{E}_{\perp}^* \times \mathbf{A}_{\perp} d^3 \mathbf{r} + \frac{1}{\mu_0} \sum_{j=x,y} \int \mathbf{E}_{\perp j}^* (\mathbf{r} \times \nabla)_i \mathbf{A}_{\perp j} d^3 \mathbf{r} \quad (2.31)$$

which is obviously gauge invariant.

2.4 Angular momentum of the quantized electromagnetic field

The quantized electric and magnetic field are given in terms of the photon creation and annihilation operators [4];

$$\begin{aligned} \widehat{\mathbf{E}}(\mathbf{r}; t) &= \sum_{\mathbf{k}, s} \sqrt{\frac{\hbar \omega}{2 \epsilon_0 V}} \left(\epsilon_{\mathbf{k}, s} \widehat{a}_{\mathbf{k}, s} e^{i(\mathbf{k} \cdot \mathbf{r} - \omega t)} + H.C. \right) \\ \widehat{\mathbf{B}}(\mathbf{r}; t) &= \sum_{\mathbf{k}, s} \sqrt{\frac{\hbar}{2 \omega \epsilon_0 V}} \left((\mathbf{k} \times \epsilon_{\mathbf{k}, s}) \widehat{a}_{\mathbf{k}, s} e^{i(\mathbf{k} \cdot \mathbf{r} - \omega t)} + H.C. \right) \end{aligned} \quad (2.32)$$

where *H.C.* denotes the Hermitian Conjugate of the preceding term, V is the volume, $\epsilon_{\mathbf{k}, s}$ is the polarization unit vector, $\widehat{a}_{\mathbf{k}, s}^{\dagger}$ and $\widehat{a}_{\mathbf{k}, s}$ are the creation and annihilation operators for photon in the mode \mathbf{k} and polarization state s , respectively. In this notation we did not care about spatial properties of photon and we have only kept its vectorial characteristic. The creation and annihilation, of course, are not commuting. Their

commutation relations are

$$\begin{aligned} \left[\hat{a}_{\mathbf{k},s}, \hat{a}_{\mathbf{k}',s'}^\dagger \right] &= \delta_{\mathbf{k},\mathbf{k}'}^3 \delta_{s,s'} \\ \left[\hat{a}_{\mathbf{k},s}, \hat{a}_{\mathbf{k}',s'} \right] &= 0 \\ \left[\hat{a}_{\mathbf{k},s}^\dagger, \hat{a}_{\mathbf{k}',s'}^\dagger \right] &= 0 \end{aligned} \quad (2.33)$$

It can be shown that, using the above commutation relations, that the electromagnetic field also are not commuting

$$\begin{aligned} \left[\hat{E}_l(\mathbf{r}; t), \hat{B}_m(r'; t) \right] &= -\frac{i\hbar}{\mu_0 c^2} \partial_n \delta^3(\mathbf{k} - \mathbf{k}') \\ \left[\hat{E}_i(\mathbf{r}; t), \hat{B}_i(r'; t) \right] &= 0 \end{aligned} \quad (2.34)$$

where l, m, n form a cyclic permutation of x, y, z . Substituting the quantized electromagnetic field in the classical expression of the energy, we obtain

$$U = \sum_{\mathbf{k},s} \hbar\omega \left(\hat{a}_{\mathbf{k},s}^\dagger \hat{a}_{\mathbf{k},s} + \frac{1}{2} \right) \quad (2.35)$$

where the summation is over all modes and polarization states. The $\frac{\hbar\omega}{2}$ term is the well-known *zero point energy*. Note that the transformation from classical expression of the energy to the quantum one does not need Hermiticity. This formula is already Hermitian. With this representation of the quantized electromagnetic field we can just find an explicit expression for the spin angular momentum. To find an elegant expression for OAM part we must quantize the transverse spatial space. We have postponed it to the paraxial wave equation's section.

The classical expression of the SAM unlike the energy is not Hermitian. So, we must first make it Hermitian. A proper Hermitian expression is given by

$$\hat{\mathbf{S}} = \frac{1}{4\pi} \int \left(\hat{\mathbf{E}} \times \hat{\mathbf{A}} - \hat{\mathbf{A}} \times \hat{\mathbf{E}} \right) d^3\mathbf{r} \quad (2.36)$$

Substituting the quantized field (2.32) into the above equation we have

$$\hat{\mathbf{S}} = i \sum_{\mathbf{k}} \hbar \mathbf{u}_{\mathbf{k}} \left(\hat{a}_{\mathbf{k},H}^\dagger \hat{a}_{\mathbf{k},V} - \hat{a}_{\mathbf{k},V}^\dagger \hat{a}_{\mathbf{k},H} \right) \quad (2.37)$$

where $\mathbf{u}_{\mathbf{k}}$ is the unit vector in the propagation direction, H and V are the Horizontal and Vertical polarization states. $\hat{\mathbf{S}}$ is off diagonal in terms of the *Fock states* in the HV polarization basis. It is much more convenient and elegant to rewrite the SAM operator in the Left (L) and Right (R) circular basis.

$$\hat{\mathbf{S}} = \sum_{\mathbf{k}} \hbar \mathbf{u}_{\mathbf{k}} \left(\hat{a}_{\mathbf{k},L}^\dagger \hat{a}_{\mathbf{k},L} - \hat{a}_{\mathbf{k},R}^\dagger \hat{a}_{\mathbf{k},R} \right)$$

$$= \sum_{\mathbf{k}} \hbar \mathbf{u}_{\mathbf{k}} (\hat{n}_{\mathbf{k},L} - \hat{n}_{\mathbf{k},R}) \quad (2.38)$$

where $\hat{n}_{\mathbf{k},i} = \hat{a}_{\mathbf{k},i}^\dagger \hat{a}_{\mathbf{k},i}$ is the number operator in the Fock space, L and R are the left and right polarization states, respectively, and are defined by

$$\begin{aligned} \epsilon_{\mathbf{k},L} &= \frac{1}{\sqrt{2}} (\epsilon_{\mathbf{k},H} + i\epsilon_{\mathbf{k},V}) \\ \epsilon_{\mathbf{k},R} &= \frac{1}{\sqrt{2}} (\epsilon_{\mathbf{k},H} - i\epsilon_{\mathbf{k},V}) \end{aligned} \quad (2.39)$$

Eq. (2.38) shows that the SAM with any wave vector is quantized, $\hbar \mathbf{u}_{\mathbf{k}}$, and is proportional to the difference between number of Left circularized photon and right circularized photon. Furthermore, for a plane wave the SAM is in the direction of propagation and for the Left (Right) circularly polarized photon is equal to \hbar ($-\hbar$). In general, the projection of the SAM over the propagation direction is called *helicity*. These two eigenvalues of helicity are characteristics of spin 1 particle of zero mass.

2.5 Paraxial Wave Equation

2.5.1 Paraxial wave equation and decomposition of angular momentum

In the last sections, we discussed a general approach to the Maxwell's wave equations without any approximation and we extended these characteristics to the quantized electromagnetic field. In the following, we paid particular attention to the practical solution of wave equation, for "paraxial waves". Then we present explicit expression for the both spin and angular momentum in the paraxial regime of light. Paraxial wave optics is a class of the wave's optics which deals with the propagation of light beams whose transverse dimensions are much smaller than the typical longitudinal distance over which the field changes applicably in magnitude. The transverse and longitudinal magnitude are of order of the beam waist (w_0) and Rayleigh parameter ($z_R = kw_0^2/2$), respectively. So, the paraxiality can be measured by the ratio z_R/w_0 [16].

For a monochromatic beam which propagates along the z -direction, the electric field can be chosen as

$$\mathbf{E}(\mathbf{r}) = e^{ikz} \tilde{\mathbf{E}}(\mathbf{r}) \quad (2.40)$$

Substituting this ansatz into the Helmholtz wave equation (2.4) we have

$$(\nabla_{\perp}^2 + 4i\partial_{\zeta}) \tilde{\mathbf{E}}(\mathbf{r}) = 0 \quad (2.41)$$

where $\nabla_{\perp}^2 := \partial_{\xi,\xi} + \partial_{\eta,\eta}$ is the transverse laplacian, and $(\xi = x/w_0, \eta = y/w_0, \zeta = z/z_R)$ are the dimensionless coordinates. To derive this equation we have used the paraxial approximation, $|\frac{\partial^2 \tilde{\mathbf{E}}(\mathbf{r})}{\partial z^2}| \ll k|\frac{\partial \tilde{\mathbf{E}}(\mathbf{r})}{\partial z}|$. The paraxial approximation may be interpreted in the momentum space too. In the momentum space paraxiality is equal to neglecting of the transverse components of wave vector with respect to the longitudinal component [41]. Furthermore, in the paraxial regime, it can be shown via the Gauss law that the z -component of the $\tilde{\mathbf{E}}(\mathbf{r})$ is smaller than the transverse part by the scale of w_0/z_R , i.e. $\tilde{E}_z = -\frac{i}{k} \nabla_{\perp} \cdot \tilde{\mathbf{E}}$. Then, we may neglect the z -component of the electric field and just kept the transverse components until we explicitly said.

According to the uncertainty principle just the z -component of angular momentum will be the subject of our discussion. The z -component of angular momentum in the paraxial regime

$$J_z = \frac{\Re \left\{ -i\hbar \iint d\sigma_{\perp} \left(\tilde{\mathbf{E}}^* \cdot (\mathbf{u}_z \cdot (-i\mathbf{r} \times \nabla)) \tilde{\mathbf{E}} \right) + \mathbf{u}_z \cdot \tilde{\mathbf{E}}^* \times \tilde{\mathbf{E}} \right\}}{\Re \left\{ \iint d\sigma_{\perp} \tilde{\mathbf{E}}^* \cdot \tilde{\mathbf{E}} \right\}} \quad (2.42)$$

where \mathbf{u}_z is the unit vector in the z -direction, $\tilde{\mathbf{E}}$ is the transverse part of paraxial field and $d\sigma_{\perp}$ is the transverse surface element. This expression is quite similar to the Humblet decomposition of angular momentum which was derived without paraxial approximation and is valid for three dimensional beams. It is appropriate to use the circular basis

$$\begin{aligned} |E\rangle &= \begin{pmatrix} E_L \\ E_R \end{pmatrix} \\ &= \frac{1}{\sqrt{2}} \begin{pmatrix} E_x + iE_y \\ E_x - iE_y \end{pmatrix} \end{aligned} \quad (2.43)$$

Then we can rewrite the Eq. (2.42)

$$J_z = \frac{\langle \tilde{\mathbf{E}} | \hat{L}_z | \tilde{\mathbf{E}} \rangle + \langle \tilde{\mathbf{E}} | \hat{S}_z | \tilde{\mathbf{E}} \rangle}{\langle \tilde{\mathbf{E}} | \tilde{\mathbf{E}} \rangle} \quad (2.44)$$

with

$$\hat{S}_z = \hbar \begin{pmatrix} 1 & 0 \\ 0 & -1 \end{pmatrix}, \quad \hat{L}_z = -i\hbar (\mathbf{r} \times \nabla) \quad (2.45)$$

The denominator is just a normalization factor. So, without losing of generality we may consider it *unity*, i.e. $\langle \tilde{\mathbf{E}} | \tilde{\mathbf{E}} \rangle = 1$. Equation (2.44) is the well-known expression for

angular momentum in the quantum theory. Unlike the general theory of light angular momentum (2.3), this decomposition is not based on the position-dependent separation. In another words, linear momentum in the paraxial approximation is almost longitudinal and the averages of the transverse components are almost zero. So, changing of the coordinate's origin over the transverse plane does not change the z -component of the orbital angular momentum. Therefore, both z -component of angular momenta (SAM and OAM) are origin invariant and they do not change by shifting the coordinate's origin in the transverse plane. However, the SAM depends on the photon polarization state, while the OAM depends on the spatial profile of the transverse field.

$$\begin{aligned} S_z &= \hbar \int d\sigma_{\perp} (|E_L|^2 - |E_R|^2) \\ L_z &= \hbar \int d\sigma_{\perp} (E_L^* \partial_{\phi} E_L + E_R^* \partial_{\phi} E_R) \end{aligned} \quad (2.46)$$

where ϕ is the azimuthal variable (we have already considered a normalized beam). S_z can have values of $\pm\hbar$ associated to the left and right circular polarized beam, respectively. L_z is related to the spatial structure of beam, especially is depending on the azimuthal structure. For instance, a light beam with a helical structure ($e^{im\phi}$) possesses $m\hbar$ angular momentum per photon. Moreover, it has been shown that OAM is associated to the dislocation lines in the optical field or singular optics. Let us show it by choosing a special class of paraxial beams family, named "spiral beams" with the beam waist w_0 at the pupil

$$\psi(\rho, \phi; 0) = \sum_{m=0}^{\ell} f_m r^m e^{-\frac{\rho^2}{2w_0^2} + im\phi} \quad (2.47)$$

where (ρ, ϕ) are the cylindrical coordinates. Substituting (2.47) into (2.46) we have

$$L_z = \langle m \rangle \hbar$$

with

$$\langle m \rangle = \frac{\sum_{m=0}^{\ell} m m! |f_m|^2 w_0^{2m}}{\sum_{m=0}^{\ell} m! |f_m|^2 w_0^{2m}} \quad (2.48)$$

For a pure phase mode we have $L_z = \ell\hbar$. It is an interesting example to distinguish optical dislocation lines and the OAM eigenvalue.

TABLE 2.1: Classification of modes families.

a	b	$p(\zeta)$	$w(\zeta)$	Mode class
0	0	0	1	Bessel Modes
0	1/2	0	$\sqrt{\zeta}$	HyG Modes[12]
0	1	ζ	$\sqrt{1 + \zeta^2}$	LG Modes
-i/2	0	ζ	$\sqrt{\zeta(i + \zeta)}$	HyGG Modes[13]
i/2	0	0	$\sqrt{1 + i\zeta}$	HyGG type-II Modes[14]

2.5.2 Paraxial wave equation and its orbital angular momentum eigenstates

We showed that the SAM is related to the beam vectorial properties (polarization states) of the transverse optical field. The azimuthal part of the complex optical field is also defining the beam OAM. However, the radial part of the optical field in the paraxial regime also plays an important role in the photon classical and quantum information theory. The radial part like azimuthal and unlike spin, is inherently infinite dimensional. We, then, consider the scalar paraxial wave equation instead of vectorial one. Let us start to find some interesting families of the scalar PWE. We look for some solutions which are already the eigenstates of OAM. Our suggested ansatz has the following form

$$\psi(\rho, \phi; \zeta) = \frac{1}{w(\tau)} u\left(\frac{\rho}{w(\tau)}, \tau\right) e^{-ip(\tau)\frac{\rho^2}{w^2(\tau)} + im\phi} \quad (2.49)$$

where $\tau := \tau(\zeta)$ is a function of ζ , $w(\tau)$ and $p(\tau)$ are two dimensionless functions of τ which are associated to the diffraction effects. Inserting this ansatz into the scalar PWE, yields a partial differential equation for $u(r, \tau)$. We can cast this differential equation similar to the standard Schrödinger equation

$$i\partial_\tau u(r, \tau) = \hat{\mathcal{H}}(\tau)u(r, \tau) \quad (2.50)$$

where τ -depend Hamiltonian is

$$\begin{aligned} \hat{\mathcal{H}}(\tau) := & -\frac{1}{4} \left(\hat{P} + 4 \left(\frac{\partial_\tau w(\tau)}{w(\tau)} - p(\tau) \right) \hat{Y} - \frac{|m|^2}{\rho^2} \right) \\ & + \rho^2 \left(\partial_\tau p(\tau) + p^2(\tau) - 2p(\tau) \frac{\partial_\tau w(\tau)}{w(\tau)} \right) \end{aligned} \quad (2.51)$$

with

$$\begin{aligned} \hat{P} & := \partial_{\rho, \rho} + \frac{\partial_\rho}{\rho} + \frac{\partial_{\phi, \phi}}{\rho^2} \\ \hat{Y} & := -i\rho \partial_\rho - i \end{aligned} \quad (2.52)$$

are two Hermitian operators with respect to the measure $\rho d\rho$. $\widehat{\mathcal{H}}(\tau)$ is Hermitian if $w(\tau)$ and $p(\tau)$ are real valued functions of parameter τ . It is convenient to work out with the stationary Schrödinger equation and define these two arbitrary parameters

$$\begin{aligned} \frac{\partial_\tau w(\tau)}{w(\tau)} - p(\tau) &= a \\ \partial_\tau p(\tau) + p^2(\tau) - 2p(\tau) \frac{\partial_\tau w(\tau)}{w(\tau)} &= b \end{aligned} \quad (2.53)$$

which are defining the Hermiticity of the Hamiltonian and the solution families. These two parameters and initial conditions for the diffraction property effects, i.e. $p(\tau)$ and $w(\tau)$, define the wave class of the scalar PWE. Table (2.1) shows some classes of the PWE solution based on proper choice of these four values. Due to complexity of $w(\tau)$, some families such as HyGG and HyGG type-II are not orthogonal set of modes.

2.5.2.1 Laugerre-Gaussian modes

For instance, by choosing $a = 0$, $b = 0$, $p(0) = 0$ and $w(0) = 1$, we will get the well-known Laugerre-Gaussian modes which are the famous solution of the scalar PWE in the cylindrical coordinate

$$|\text{LG}\rangle_{p,m} = \sqrt{\frac{2^{|m|+1}p!}{\pi(p+|m|)!}} \left(\frac{i}{\zeta+i}\right)^m \left(\frac{i-\zeta}{i+\zeta}\right)^p \rho^{|m|} e^{-\frac{i\rho^2}{\zeta+i}} L_p^{|m|} \left(\frac{2\rho^2}{1+\zeta^2}\right) \quad (2.54)$$

where m is a integer valued and defining the OAM eigenvalues, p is the integer number $p \geq 0$ and is defining the radial nodes in the transverse plane, and $L_p^{|m|}$ is the generalized Laguerre polynomial. The LG modes are important solution of PWE, because they are orthogonal set of PWE's solution, i.e. ${}_{p',m'}\langle \text{LG} | \text{LG} \rangle_{p,m} = \delta_{p,p'} \delta_{m,m'}$ and they carry a finite power[16]. Indeed, they are shape invariant modes under free propagation. In another word, while beam propagates along ζ , its intensity pattern does not change and is just scaled. Figure (2.1) shows the propagation of $\text{LG}_{0,2}$ in interval of $-2 < \zeta < +2$. Moreover, they are eigenvalues of OAM and they possess a well-defined values of OAM. The intensity and phase profiles of several LG modes are shown in Fig. (2.2) and (2.3). As you can see the intensity profile for positive and negative values of OAM are the same and just the phase patterns are reversed.

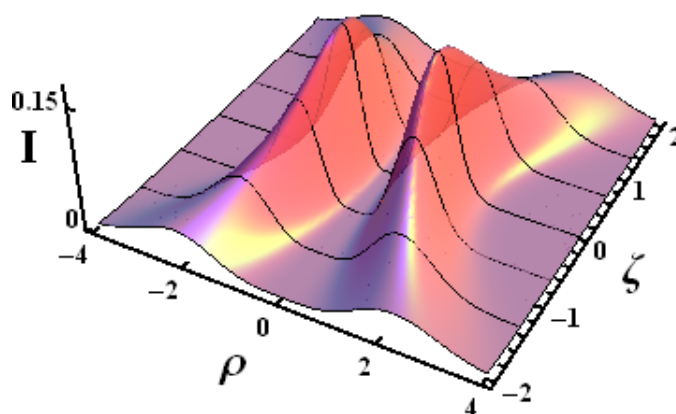


FIGURE 2.1: Propagation of the $LG_{0,2}$ in interval of $-2 < \zeta < +2$. As you can see by propagation the transverse profile, mesh lines, are the same and just is scaled.

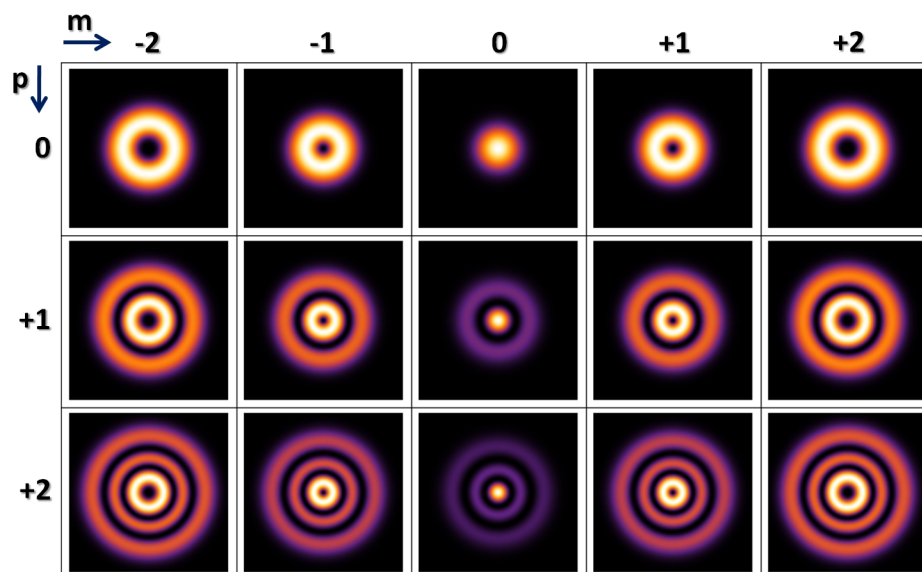


FIGURE 2.2: The LG intensity profiles for different radial and azimuthal number at the distance of $\zeta = 0.25$. The intensity profiles for absolute values of OAM are the same. The rows and column are defining the azimuthal and radial number, respectively.

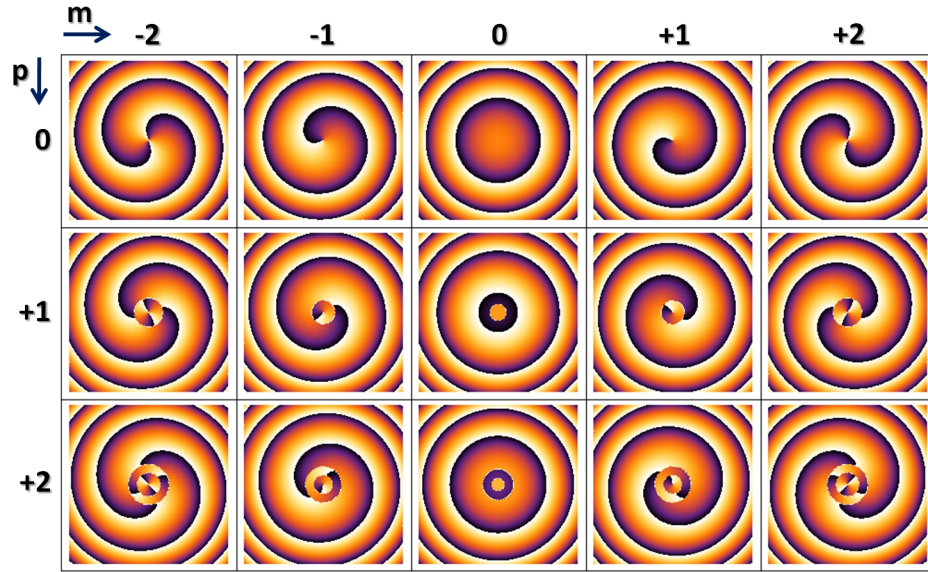


FIGURE 2.3: The LG phase structures for different radial and azimuthal number at the distance of $\zeta = 0.25$. The phase patterns for absolute values of OAM are reversed. The rows and column are defining the azimuthal and radial number, respectively. Black and yellow colors are corresponding to 0 and 2π .

2.5.2.2 Hypergeometric-Gaussian modes (Karimi et al. [13])

A novel family of the scalar PWE can be found by setting $a = -i/2$, $b = 0$, $p(0) = 0$ and $w(0) = 0$,

$$\begin{aligned}
 |\text{HyGG}\rangle_{pm} &= \sqrt{\frac{2^{p+|m|+1}}{\pi\Gamma(p+|m|+1)} \frac{\Gamma(1+|m|+\frac{p}{2})}{\Gamma(|m|+1)}} i^{|m|+1} \zeta^{\frac{p}{2}} (\zeta+i)^{-(1+|m|+\frac{p}{2})} \\
 &\times \rho^{|m|} e^{-\frac{i\rho^2}{\zeta+i}} e^{im\phi} {}_1F_1\left(-\frac{p}{2}, |m|+1; \frac{\rho^2}{\zeta(\zeta+i)}\right)
 \end{aligned} \quad (2.55)$$

where m is integer, $p \geq -|m|$ is real valued, $\Gamma(x)$ is the gamma function and ${}_1F_1(a, b; x)$ is the confluent hypergeometric function [42]. The amplitude of this novel modes are proportional to confluent hypergeometric function, so, we called them *Hypergeometric-Gaussian* (HyGG). $w(\tau)$ is not real function (see Table 2.1), so, the HyGG modes are not orthogonal set of modes

$${}_{p',m'}\langle \text{HyGG} | \text{HyGG} \rangle_{p,m} = \delta_{m,m'} \sqrt{\frac{\Gamma(p/2 + p'/2 + |m| + 1)}{\Gamma(p' + |m| + 1)\Gamma(p + |m| + 1)}}$$

. Nevertheless, the HyGG modes carry a finite power. The HyGG modes can be expanded in the complete basis of the LG modes. In general, the mode HyGG_{pm} is a superposition of the infinite LG_{qm} modes with same m and any integer $q \geq 0$. In fact, when both the HyGG and the LG modes are normalized (2.54,2.55), we have

$|\text{HyGG}\rangle_{pm} = \sum_{q=0}^{\infty} A_{pq} |\text{LG}\rangle_{qm}$ with coefficients A_{pq} given by

$$A_{pq} = \sqrt{\frac{(q+|m|)!}{q! \Gamma(p+|m|+1)}} \frac{\Gamma(q-p/2) \Gamma(p/2+|m|+1)}{\Gamma(-p/2) \Gamma(q+|m|+1)}. \quad (2.56)$$

The HyGG modes can exhibit different features when the mode parameters p and m are changed. It is then convenient to separate the HyGG modes in a few subfamilies having similar properties.

1. $p = m = 0$

This mode is the well known Gaussian mode TEM_{00} .

2. $p = -|m|$, odd.

At planes $\zeta > 0$ the modes are linear combinations of the modified Bessel functions $I_0(x)$ and $I_1(x)$, where $x = \rho^2/2\zeta(\zeta + i)$. We call this subfamily of modes the modified Bessel Gauss (MBG) modes. Unlike the well known Bessel modes, these modes carry a finite power and are not diffraction free. When $\rho \rightarrow \infty$ at fixed $\zeta > 0$, the intensity of these modes vanishes according to $|u_{pm}|^2 \propto \rho^{-4}$.

3. $p = -|m|$, even.

At planes $\zeta > 0$ the modes are linear combinations of exponential ρ -dependent terms. We call this subfamily of modes the Modified Exponential Gauss (MEG) modes. When $\rho \rightarrow \infty$ at fixed ζ , the intensity of these modes vanishes according to $|u_{pm}|^2 \propto \rho^{-4}$.

4. $p \geq 0$, even.

When p is a non negative even integer, the confluent hypergeometric function reduces to a Laguerre polynomial. We will refer to these modes as to the modified Laguerre-Gauss modes (MLG). The asymptotic behavior of the intensity of the MLG modes as $\rho \rightarrow \infty$ at fixed $\zeta > 0$ is the same as for the usual LG modes (i. e. $|\text{HyGG}_{pm}|^2 \propto \rho^{2(p+|m|)} e^{-2\rho^2/(1+\zeta^2)}$). Unlike the LG_{pm} modes, however, the MLG_{pm} modes have a single-ring intensity profile for any admitted value of p . The MLG_{pm} modes can be expressed as the linear superposition of a finite number of LG_{qm} modes, namely, the LG_{qm} modes having the same m and integer $0 \leq q \leq p/2$. In fact, when p is a non negative even integer, Eq. (2.56) reduces to

$$A_{pq} = (-1)^q \frac{(p/2)! (p/2+|m|)!}{(p/2-q)! \sqrt{q!} (p+|m|)! (q+|m|)!} \quad (2.57)$$

where $0 \leq q \leq p/2$, p even. The quantities A_{pq} form the entries of a non singular $(p/2+1) \times (p/2+1)$ matrix. It is then obvious that this sub-family of HyGG modes

forms a complete, yet not orthogonal, set of functions in the transverse plane and that the full set of HyGG modes is therefore overcomplete.

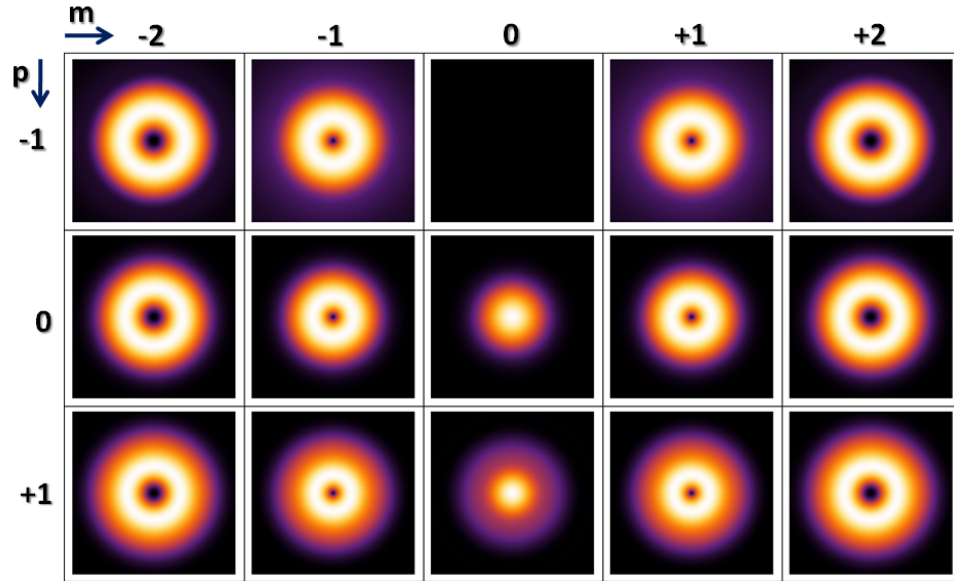


FIGURE 2.4: The HyGG intensity profiles for different radial and azimuthal number at the distance of $\zeta = 1$. The intensity profiles for the negative and positive values of the same OAM are equal. The rows and column are defining the azimuthal and radial number, respectively.

The HyGG modes are not shape invariant under free propagation. While beam propagates a dramatic change of intensity profile can be seen. We will mention further important properties of this family in the following chapters.

2.5.2.3 Hypergeometric-Gaussian type-II modes (Karimi et al. [14])

There is another novel solution family of the scalar Helmholtz PWE in the cylindrical coordinates. This family can be found by setting $a = i/2$, $b = 0$, $p(0) = 0$ and $w(0) = 1$,

$$\begin{aligned}
 |\text{HyGG-II}\rangle_{pm} = & \sqrt{\frac{2^{p+|m|+1}}{\pi\Gamma(p+|m|+1)}} \frac{\Gamma(1+|m|+\frac{p}{2})}{\Gamma(|m|+1)} \left(\frac{1}{1+i\zeta}\right)^{p/2+|m|+1} \\
 & \times \rho^{|m|} e^{-\frac{\rho^2}{(1+i\zeta)}} e^{im\phi} {}_1F_1\left(-\frac{p}{2}, |m|+1; \frac{\rho^2}{(1+i\zeta)}\right), \quad (2.58)
 \end{aligned}$$

where m is an integer, p is a real number. We named this novel family *Hypergeometric-Gaussian type-II* modes. We see that $|\text{HyGG-II}\rangle_{pm}$ stays finite as long as p is so that $p \geq -|m|$, which ensures that the power carried by HyGG-II beams is finite. It can be shown that the HyGG-II modes, like the HyGG modes [13] (but unlike the HyG

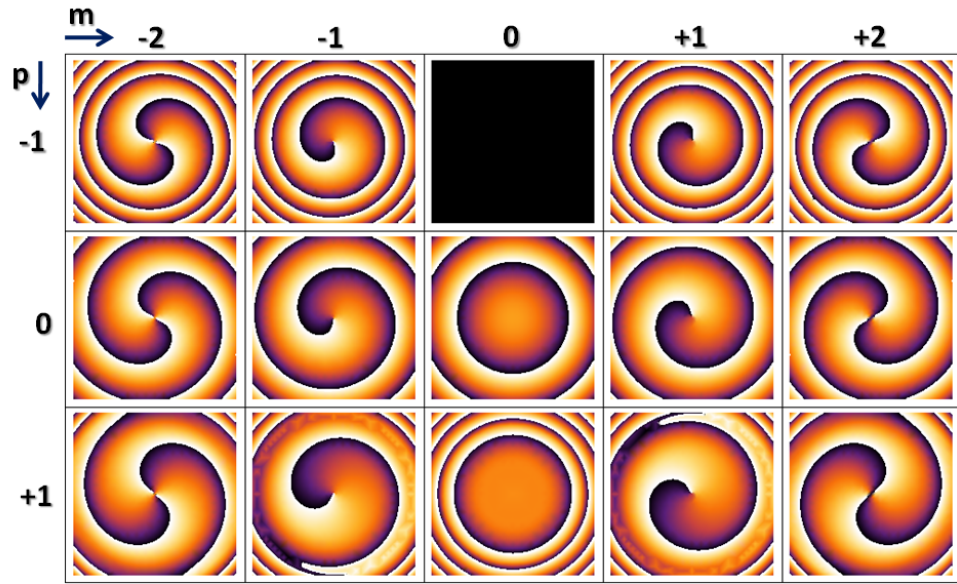


FIGURE 2.5: The HyGG phase structures for different radial and azimuthal number at the distance of $\zeta = 1$. The phase patterns for absolute values of OAM are reversed. The rows and column are defining the azimuthal and radial number, respectively. Black and yellow colors are corresponding to 0 and 2π .

modes [12]), form a non-orthogonal set, i.e.

$${}_{p'm'}\langle \text{HyGG-II} | \text{HyGG-II} \rangle_{pm} = \delta_{mm'} \frac{\Gamma(p/2 + p'/2 + |m| + 1)}{\sqrt{[\Gamma(p' + |m| + 1)\Gamma(p + |m| + 1)]}}$$

. Moreover, the HyGG-II modes, unlike the HyGG and HyG ones, have no singularity at the pupil, i.e. at $\zeta = 0$.

Because all zeros of the hypergeometric function are on the real axis, the intensity of the HyGG-II modes never vanishes in the transverse plane for $\zeta > 0$, except at $\rho = 0$ where the vortex singularity is located when $m \neq 0$. Finally, we will discuss briefly some possible subfamilies of the HyGG-II modes.

1. $p = |m| = 0$,

In this case the mode is the gaussian TEM₀₀ beam.

2. $p = -|m|$ a negative integer number

The HyGG-II can be expanded as a superposition of two modified-Bessel beams;

$$\begin{aligned} |\text{HyGG-II}\rangle_{-|m|,m}(\rho, \phi; \zeta) &= \frac{1}{\sqrt{2}} \left(\frac{1}{1+i\zeta} \right)^{3/2} e^{im\phi} \rho e^{-\frac{\rho^2}{2(1+i\zeta)}} \\ &\times \left[I_{\frac{|m|-1}{2}} \left(\frac{\rho^2}{2(1+i\zeta)} \right) - I_{\frac{|m|+1}{2}} \left(\frac{\rho^2}{2(1+i\zeta)} \right) \right] \end{aligned} \quad (2.59)$$

We call this sub-family “modified Bessel Gauss modes of type-II” (MBG-II), for distinguishing them from those introduced in [13].

3. For $p \geq 0$ even integer number

One can easily show that

$$u_{2n,m}(\rho, \phi; \zeta) = \sqrt{\frac{2^{2n+|m|+1}}{\pi\Gamma(2n+|m|+1)}} \Gamma(n+1) \left(\frac{1}{1+i\zeta}\right)^{n+|m|+1} \times e^{-\frac{\rho^2}{1+i\zeta}} \rho^{|m|} e^{im\phi} L_n^{|m|}\left(\frac{\rho^2}{1+i\zeta}\right). \quad (2.60)$$

which are the well-known “elegant Laguerre-Gauss” (eLG) beams [11].

4. For $p > 0$ odd integer number

The HyGG-II modes reduce to a polynomial superposition of the modified Bessel functions $I_0(x)$ and $I_1(x)$. We call this sub-family “modified-polynomial Bessel-Gauss” (MPBG) beams.

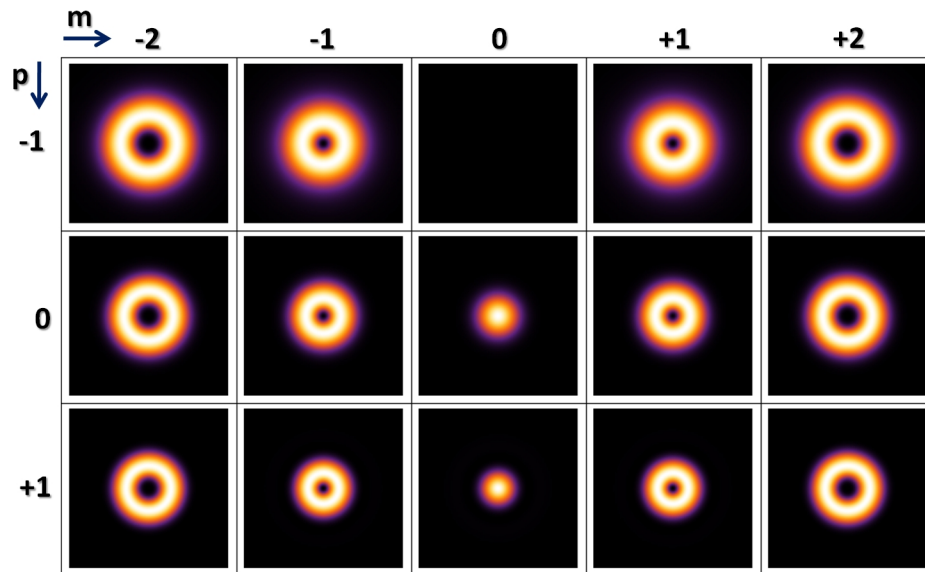


FIGURE 2.6: The HyGG type-II intensity profiles for different radial and azimuthal number at the distance of $\zeta = 0.25$. The intensity profiles for the negative and positive values of the same OAM are equal. The rows and column are defining the azimuthal and radial number, respectively.

A very interesting property of HyGG-II modes is that they suffer very low diffraction. In fact, the divergence angle at waist of the HyGG-II modes is smaller than for the BG and LG modes. Figure (2.7) compares the variation of the maximum intensity radius of HyGG-II, BG and LG beams while they propagate along the z -axis. We see that HyGG-II has a slope 12.5% lower than LG beam and 28% lower than BG beam, where

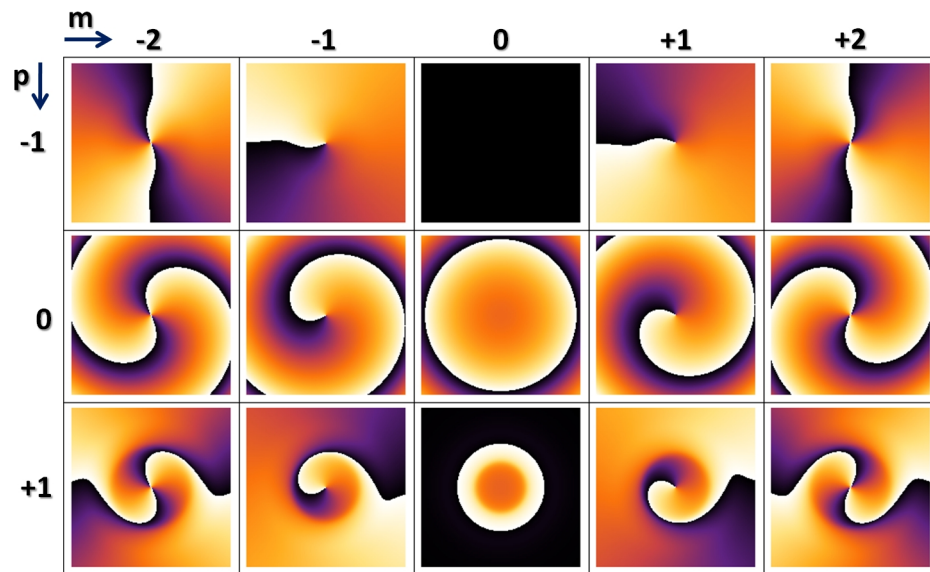


FIGURE 2.7: The HyGG type-II phase structures for different radial and azimuthal number at the distance of $\zeta = 0.25$. The phase patterns for absolute values of OAM are reversed. The rows and column are defining the azimuthal and radial number, respectively. Black and yellow colors are corresponding to 0 and 2π .

we define slope = $\frac{w(z_R) - w_0}{z_R}$. We will show in chapter (4) that one can use this property to generate a needle beam below the diffraction limit.

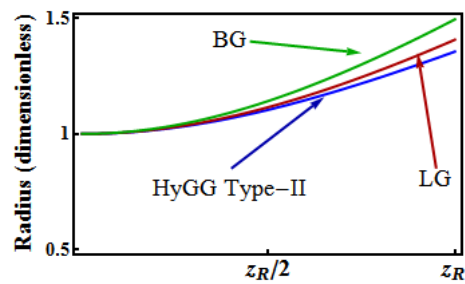


FIGURE 2.8: Variation of maximum intensity radius during the propagation for $LG_{0,1}$, BG_1 , $HyGG-II_{-1,1}$

Chapter 3

Generation and detection of the orbital angular momentum of light

3.1 Introduction

We have shown that a light beam, besides energy and linear momentum, possesses two “rotational” like degrees of freedom: SAM and OAM. The SAM is related to the vectorial properties of optical field and it could take $+\hbar$ or $-\hbar$ in the direction of propagation for Left or Right circular polarized beam, respectively. The OAM is associated to the spatial structure of the complex optical field. Especially, a beam with a helical phase-front, i.e. whose complex field expression includes the phase factor $e^{im\phi}$, where m is an integer and ϕ the azimuthal coordinate around the beam axes is endowed with a well-defined value of OAM per photon in the propagation direction, given by $m\hbar$. The OAM Hilbert space is hence inherently infinite-dimensional while SAM’s Hilbert space is binary.

It is well-known that the SAM (polarization state) can be generated and manipulated by using birefringent wave plates. As we will show in section (4.4) all possible polarization states in the SAM’s Hilbert space can be easily generated by using a half-wave plate sandwiched between two quarter wave plates.

In this chapter we review some recent novel techniques to generate and manipulate the OAM of a given light beam. The same techniques with small variations can be also used as detectors of specific given values of OAM.

3.2 Spiral phase plate

The spiral phase plate (SPP) is a transparent dielectric plate with one plane and one spiral surface. The SSP thickness increases proportional to the azimuthal angle, ϕ , around a point at the center of plate. So, the surface resembles a turn of a staircase, i.e. the spiral surface forms a period of helix. Such a thin transparent plate typically has strips or radial sectors that can be obtain by coating or etching a substrate. Figure (3.1) shows a schematic of a SPP illuminated by a TEM_{00} beam and its outgoing wave. In this example the step is designed to generate OAM beam with OAM equal to \hbar per photon. When a light beam of wavelength λ passes through the SPP, the helical surface can be

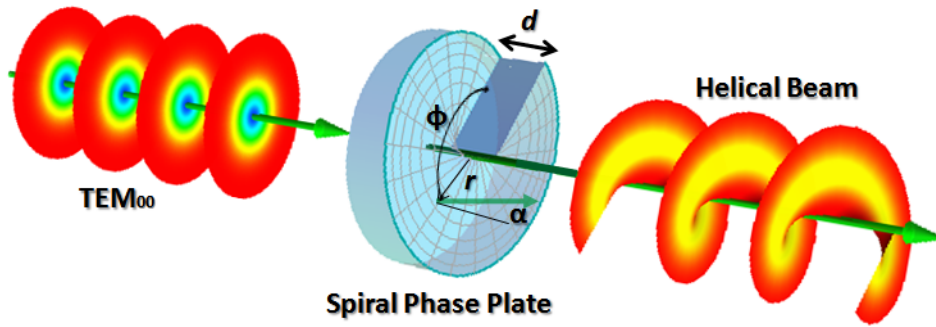


FIGURE 3.1: Schematic of a SPP illuminated by a TEM_{00} beam and its outgoing wave. In this example, the step is designed to generate OAM beam with OAM equal to \hbar per photon.

expected to give a helical structure to the beam wavefront. In fact, SPP introduces in the outgoing beam a phase shift, δ , which depends on the azimuthal angle ϕ

$$\delta = \frac{(n_1 - n_2)d}{\lambda} \phi \quad (3.1)$$

where n_1 , n_2 are the refractive indices of the SPP and surrounding medium, respectively, and d is the physical step height at $\phi = 0$. For generating a beam with a well-defined value of OAM, e.g. $\ell\hbar$, the total phase delay around the SPP must be an integer multiple of 2π , i.e. $2\pi\ell$. Thus, to produce this beam, the physical height of the step in the SPP is given by

$$d = \frac{\ell\lambda}{(n_1 - n_2)}. \quad (3.2)$$

When the step height is not an integer number of wavelength, the phase of beam is discontinuous at the step and this discontinuity breaks the ring intensity pattern. Beijersbergen et al. [17] modelled the detuning of the step height through the transmission from one helical mode to another one. In their small-angle approximation the converter

only changes the phase pattern of beam and it does not change the beam's intensity. The annular intensity pattern arises from the far field diffraction of the beam's screw dislocation. However, the beam produced is not a pure LG mode, but is an infinite superposition of the LG mode with fixed azimuthal index and summed over whole radial numbers [20]. A rigorous calculation of the SPP operation would require vector-diffraction theory. For beam with small divergence and with a height of step that is sufficiently small we remain in the paraxial regime. So, the effect of the SPP can be considered to be an operation acting on the field phase only. We have decided to calculate the action of SPP by using the ray optics analysis [43]. We just use the ray optics model to gain insight into how OAM content of the beam arises from the SPP. Although the OAM is property of the beam as a whole. It is useful to consider this in terms of two equivalent angular momentum per photon.

Let us consider a ring of radius r projected on the spiral surface. The angle, θ , of the local azimuthal slope of the spiral surface is then given by

$$\tan \theta = \frac{d}{2\pi r}. \quad (3.3)$$

A ray parallel to, but a distance r from, the optical axes will be refracted as it emerges from the spiral surface. The deflection angle, α , may be found using *Snell's* law

$$n_2 \sin(\alpha + \theta) = n_1 \sin \theta$$

before refraction, the beam has a linear momentum of $n_2 \frac{\hbar}{2\pi\lambda}$ per photon. After refraction, there is a component of linear momentum in the azimuthal direction

$$P_\phi = \frac{n_2 \hbar}{2\pi\lambda} \sin \alpha. \quad (3.4)$$

There is a transfer of angular momentum, L , between the SPP and the beam of light of

$$L_z = \frac{n_2 \hbar r}{2\pi\lambda} \sin \alpha \quad (3.5)$$

per photon in the beam. For a small angle than we can be shown that the OAM transfer from the plate to the light is equal to

$$L_z \approx \ell \hbar \quad (3.6)$$

per photon in the direction of beam. This agrees with the result for LG beam derived from the analysis of Maxwell's equations (2.5.2.1).

3.3 Cylindrical lenses Mode converter

The essential understanding of the cylindrical lens mode converter is lying under the Laugerre-Gaussian and Hermite-Gaussian mode relations. Indeed, the expansion formula for the LG mode in the basis of Hermite-Gaussian will be the essential understanding of the mode converter's action.

A possible solution of the scalar wave equation in the cartesian coordinates is given by the HG modes:

$$\begin{aligned}
 |\text{HG}\rangle_{m,n} &= \sqrt{\frac{2}{2^{(m+n)}\pi m!n!}} \frac{1}{\sqrt{1+\zeta^2}} e^{-i(m+n+1)\arctan\zeta} \\
 &\times e^{-\left(\frac{1+i\zeta}{1+\zeta^2}\right)(\eta^2+\xi^2)} H_m\left(\sqrt{\frac{2}{1+\zeta^2}}\eta\right) H_n\left(\sqrt{\frac{2}{1+\zeta^2}}\xi\right)
 \end{aligned} \quad (3.7)$$

where $H_n(x)$ is the Hermite polynomials of order n , (ξ, η, ζ) are the dimensionless coordinates (2.5). The HG modes are an orthogonal set of modes and they carry finite power

$${}_{m',n'}\langle\text{HG}|\text{HG}\rangle_{m,n} = \delta_{m,m'}\delta_{n,n'} \quad (3.8)$$

The Gouy phase here is the sum over the two Gouy phases for η and ξ axis. It will be convenient to rewrite the LG modes (2.54) according to mode order $N := m + n$;

$$\begin{aligned}
 |\text{LG}\rangle_{m,n} &= (-1)^{\min(m,n)} \sqrt{\frac{2}{\pi m!n!}} \frac{1}{\sqrt{1+\zeta^2}} e^{-i(m+n+1)\arctan\zeta} \\
 &\times e^{-\left(\frac{1+i\zeta}{1+\zeta^2}\right)\rho^2} e^{i(m-n)\phi} \left(\sqrt{\frac{2}{1+\zeta^2}}\right)^{|m-n|} L_{\min(m,n)}^{|m-n|}\left(\frac{2\rho^2}{1+\zeta^2}\right)
 \end{aligned} \quad (3.9)$$

where $\min(m, n)$ denotes the minimum between m and n . The indices we used here differ from those normally used in the previous chapter (2.54). The radial index p normally used is $\min(m, n)$ and the azimuthal index m is $m - n$. This notation has advantages with respect to the normal notation. We will show that a cylindrical mode converter transforms a $\text{HG}_{m,n}$ mode into a $\text{LG}_{m,n}$ mode and *vice versa*. Both HG and LG modes carry finite power and they form an orthogonal and complete set of modes. So, it is possible to expand one of them in the base of the others. Using the relation between Hermite and Laugerre polynomials, one can easily show that a LG beam can be expanded into a set of HG modes of the same order:

$$|\text{LG}\rangle_{m,n} = \sum_{k=0}^N i^k b(m, n; k) |\text{HG}\rangle_{N-k,k} \quad (3.10)$$

where $b(m, n; k)$ are the real expansion coefficients and are given by

$$b(m, n; k) = \sqrt{\frac{(N-k)!k!}{2^{m+n}n!m!}} \frac{1}{k} \frac{d^k}{dt^k} ((1-t)^n(1+t)^m) |_{t=0} \quad (3.11)$$

The factor i^k corresponds to a $\frac{\pi}{2}$ relative phase different between successive components. Figure (3.2) shows this mode decomposition for the first two mode orders. A HG mode

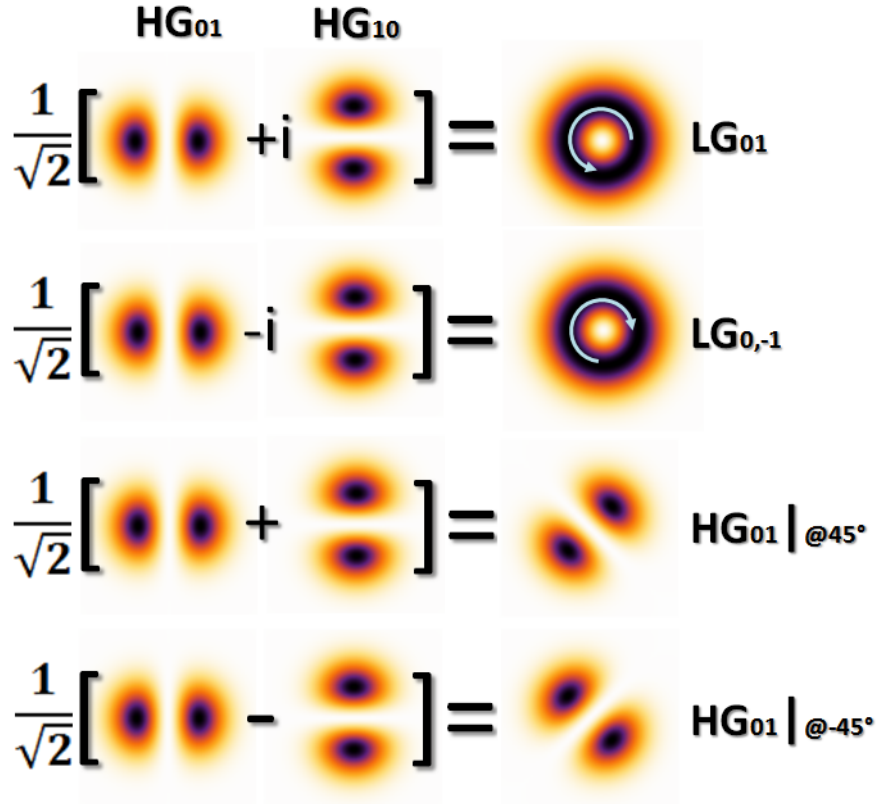


FIGURE 3.2: Decomposition of the $LG_{0,1}$, $LG_{0,-1}$, $HG_{0,1}|_{@45^\circ}$ and $HG_{0,1}|_{@-45^\circ}$ modes in the HG basis. N indicates the mode order.

whose principal axis is rotated about 45° degree around the propagation axes, i.e. ζ , can be similarly expanded in the HG basis, by using the following relation the product of Hermite polynomials;

$$|HG\rangle_{m,n}|_{@45^\circ} = \sum_{k=0}^N i^k b(m, n; k) |HG\rangle_{N-k,k} \quad (3.12)$$

where $@45^\circ$ denotes the orientation of the mode principal axis, with exactly the same real coefficients $b(m, n; k)$ of Eq. (3.11). The only difference between this expansion (3.12) and the previous one (3.10) is the relative phase between successive terms. In this expansion, instead, all terms are in phase. Figure (3.2) shows this mode decomposition for the first two mode orders. It is quite clear from these two Equations (3.10), (3.12),

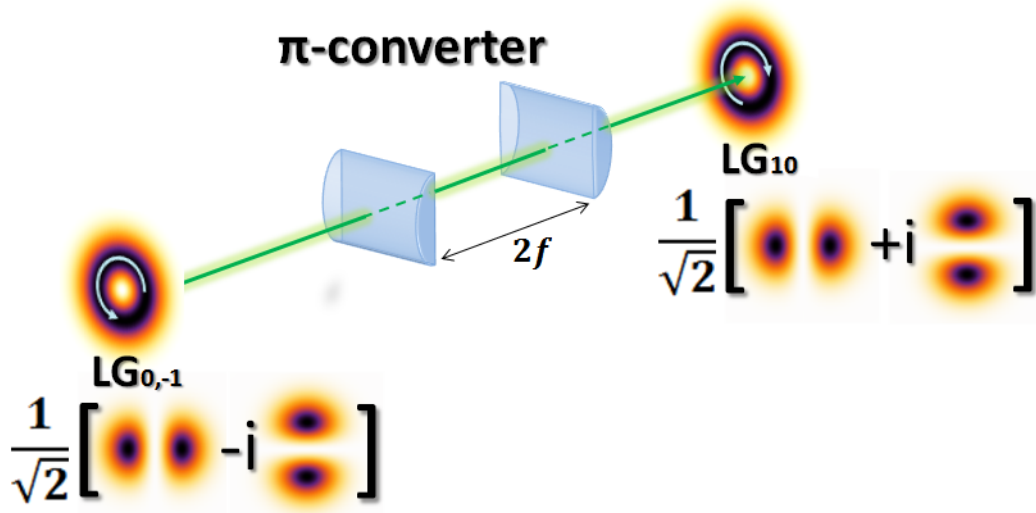


FIGURE 3.3: The schematic of π mode converter. The distance between two cylindrical lenses is $2f$. The π mode converter converts $LG_{0,\ell}$ to $LG_{0,-\ell}$. f indicates the lenses focal length.

that in order to invent a mode converter from a diagonal (or anti-diagonal) HG to the proper LG mode of the same order, one must rephase the terms in the expansion. This rephasing can be obtained via the Gouy phase.

First consider an astigmatic beam which has its nodal lines parallel to the astigmatism. Such kind of beam can be produced by passing the HG mode through a cylindrical lens aligned along the axes of the mode pattern. The amplitude of the mode can be considered separately in two beams in the (η, ζ) and (ξ, ζ) plane. In each plane, the beam is characterized by the ζ -coordinate and the Rayleigh range of the waist. Of course, these two beams waists, used hence the two Rayleigh parameters are different in general. Instead, for non-astigmatic HG beam these two waists coincide, therefore, their Rayleigh ranges are equal. So, non-astigmatic HG beam of the same order $N = m + n$ has the same Gouy phase. Nevertheless, for the astigmatic HG beam the dependence of the field directions that a parallel and orthogonal to the lens axes have different Gouy phases. Therefore, a relative phase as a function of propagation and mode order will appear between parallel and orthogonal beams.

In order to exploit the Gouy phase to construct a mode converter the beam should be made astigmatic in a confined region only while it must be non-astigmatic outside this region. When the beam is passed through this region a definite phase difference will be introduced between the HG mode components which are oriented along the axes of astigmatism. In order to transform a HG into the proper LG mode, an i factor must be introduced for each expansion terms. This i factor is corresponding to a $\pi/2$ phase difference between the successive terms. Only two types of mode converters are

interesting for our purposes; $\frac{\pi}{2}$ and π -mode converter. The first one can be used to transform HG modes into LG modes of the same order, and the second one to reverse the azimuthal index of LG mode or to change a diagonal HG mode into the corresponding anti-diagonal one. It has been shown that these two configurations of mode converters can be achieved by a properly aligned set of two cylindrical lenses in the $\frac{f}{\sqrt{2}}$ and confocal configurations, respectively, where f denotes the focal length of the lens.

The working principle of these type of mode converters is easy. A diagonal (or anti-diagonal) HG mode of order N can be decomposed into orthogonal and parallel (with respect to principal axes of the cylindrical lenses) HG modes (see figures 3.3 and 3.4). As they pass through the mode converters, they will acquire a phase difference that

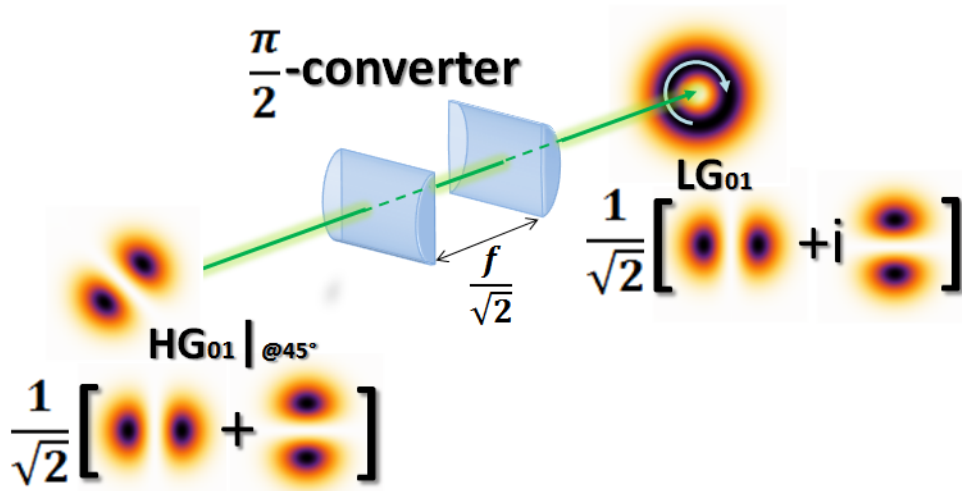


FIGURE 3.4: The schematic of $\pi/2$ mode converter. The distance between two cylindrical lenses is $\frac{f}{\sqrt{2}}$. The $\pi/2$ mode converter converts diagonal $\text{HG}_{0,1}|_{@45^\circ}$ to $\text{LG}_{0,1}$. f indicates the lenses focal length.

varies according to their mode order. An i^k or $(-1)^k$ phase factor can be obtained based on the distance between the lenses, which must be set to $\frac{f}{\sqrt{2}}$ and $2f$ for a $\pi/2$ and π converter, respectively. An analogy with the wave plates action on the polarization can be used. A QWP transforms a diagonal polarization state with no SAM in a circular polarization which possesses a SAM equal to $\pm\hbar$, and a HWP can switch the helicity of the polarization, e.g. it changes left ($+\hbar$) circular polarized light to the right ($-\hbar$) circular polarization and *vice versa*. Similarly, a $\frac{\pi}{2}$ -converter, like a QWP, transforms a diagonal HG into the proper LG beam which possesses a well-defined value of OAM, and a π -converter, like a HWP, just switches the sign of OAM. This analogy is illustrated also in figure (3.5).

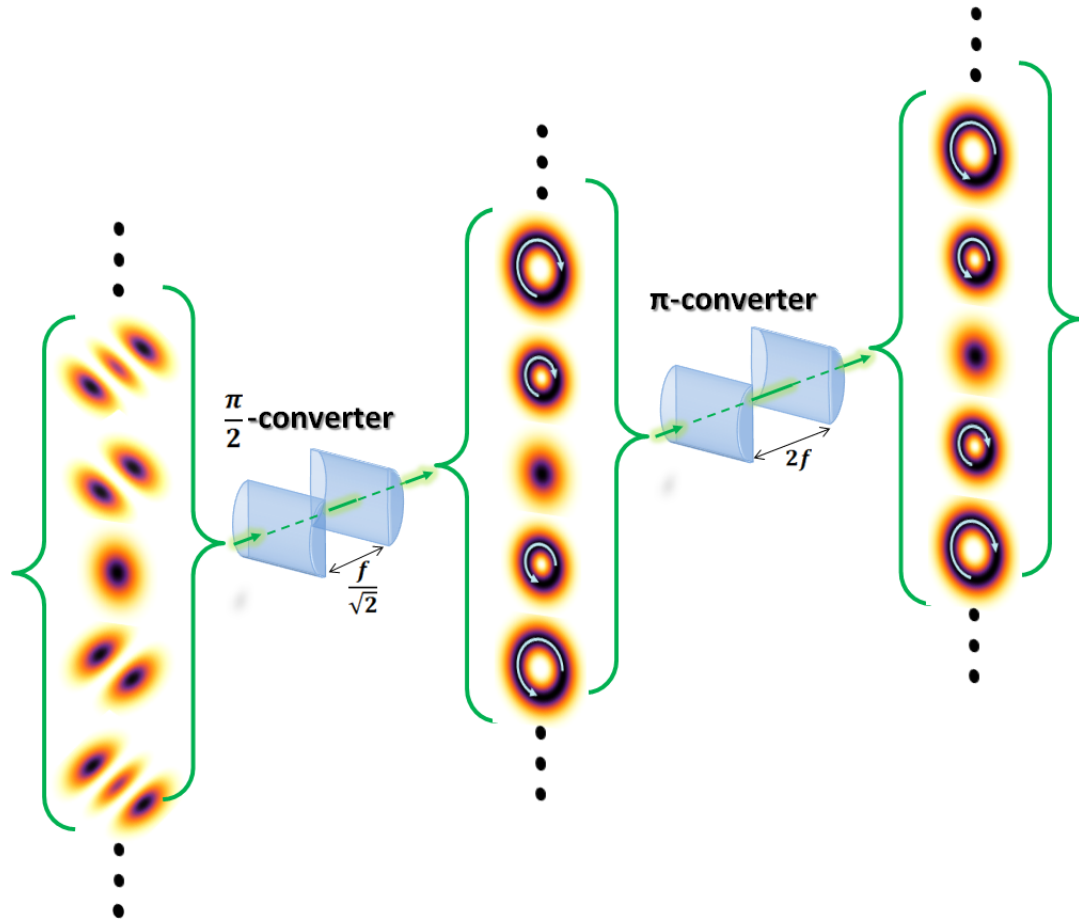


FIGURE 3.5: The schematics of $\pi/2$ and π mode converters. $\pi/2$ -converter is similar to QWP (in the OAM space) and it transfers diagonal HG into LG beams and π -converter like HWP switches the sign of helical beams.

3.4 Pitch-fork hologram and computer generated holograms

As we have shown, OAM is associated to a helical wavefront of the beam. If we generate a beam having helical wavefront, indeed, such beam would also have a well-defined value of OAM. A possible and simple method to record and generate an arbitrary beam wavefront is holography. In the holography technique, the interference pattern between an interesting and a simple reference beam is recorded over a plate named “hologram”. In general we have two possible kind of hologram: amplitude and phase hologram. For both kinds of hologram, the interference pattern is the same. An amplitude hologram transmits the light in the transparent fringes and absorbs it in the opaque ones. The amplitude-modulated outgoing light is diffracted in such a way that the beam acquire a prescribed phase-front defined by the fringes pattern. In contrast, the phase hologram does not absorb light. Instead, it changes the optical retardation spatially based on the printed phase pattern. An useful quantity to characterize a hologram is the hologram

efficiency, which is the ratio of the fraction of power located in the first order of diffraction, P_1 that is the wave component which has acquired the desired wavefront, to the impinging power on the hologram, P_0 , i.e. $E = \frac{P_1}{P_0}$. It is clear that an amplitude hologram, in the average absorbs about half of impinging power assuming total absorption in the opaque fringes. So, we expect a lower efficiency for the amplitude holograms with respect to the phase holograms.

In order to plot a hologram that generates a helical phase front starting from a planar reference we must consider the interference pattern of these two beams in a given plane, for example $x - y$.

Let us consider a plane reference beam

$$E_r = E_0 e^{i(k_x x + k_z z)} \quad (3.13)$$

with an incident angle $\alpha = \arcsin \frac{k_x}{k}$ and intensity $|E_0|^2$. At the $z = 0$ plane, the interference pattern with a helical beam, $E_\ell = E_0 e^{i\ell\phi}$, is given by

$$I = 2|E_0|^2 (1 + \cos(k_x x - \ell\phi)) \quad (3.14)$$

where we have considered that these two beams have uniform and equal intensities. Eq. (3.14) gives the required interference pattern. Figure (3.6) shows the intensity pattern of interference between a helical and plane wave beams for several different values of singularity charges. A photographic plate recordings of these patterns can now act as

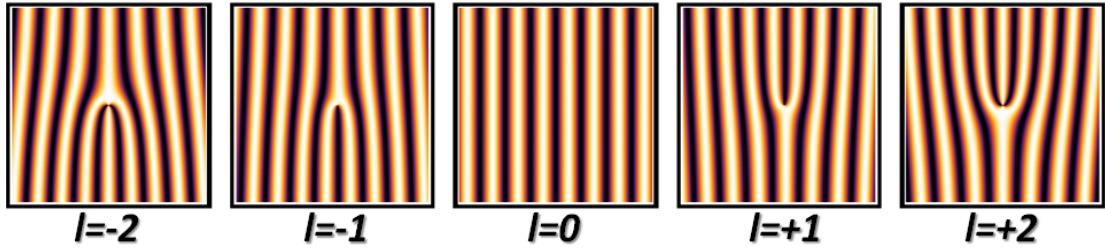


FIGURE 3.6: The intensity density pattern of interference between helical with a planar beam for several different values of the charge singularities.

holograms capable of reconstructing the original helicon beam when they are illuminated by a beam with a plane wavefront. For the case of a plane-wave input traveling along the z axis, immediately after the exit face of the hologram the optical field is given by

$$\begin{aligned} E_t &= A_0 T(x, y) \\ &= \frac{A_0}{2} (1 + \cos(k_x x - \ell\phi)) \end{aligned} \quad (3.15)$$

where $|A_0|^2$ is the intensity of illuminating beam and $T(x, y)$ is the spatial transmittance of the hologram (we have considered an amplitude hologram). By simplifying this field, we can rewrite (3.15) as

$$E_t = \frac{A_0}{2} \left(1 + \frac{1}{2} e^{(k_x x - \ell \phi)} + \frac{1}{2} e^{-(k_x x - \ell \phi)} \right) \quad (3.16)$$

This optical field can be recognized as consisting of a zero order beam propagating along the axes and two (conjugate) first order diffracted beams each of them containing a singularity of opposite charge $+\ell$ and $-\ell$ (see Fig. 3.7). The grating's shape, that

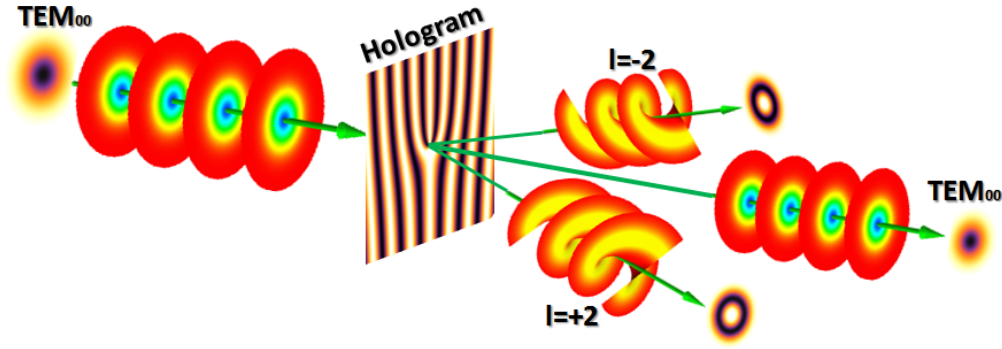


FIGURE 3.7: Beams generated by a sinusoidal pitch-fork holograms. A fraction of power diffracted on the first order and other part remains on the zeroth order. The topology of the hologram is objected to generate beams with $|\ell|=2$.

is fringe's shape patterns, of a hologram also plays an important role in determining the efficiency of a given hologram, in addition to the way of encoding, in amplitude or phase. Nevertheless, the diffracted beam wavefront is the same for all different shapes of grating. We mention four different types of grating here:

1. Sinusoidal grating

$$g(\alpha) := \frac{1}{2} (1 + \cos \alpha) \quad (3.17)$$

2. Blazed grating (saw-tooth shape)

$$g(\alpha) := \frac{1}{2\pi} \text{Mod}(\alpha, 2\pi) \quad (3.18)$$

3. Squared grating

$$g(\alpha) := \frac{1}{2} (1 + \text{Sign}(\cos \alpha)) \quad (3.19)$$

4. Triangle grating

$$g(\alpha) := \frac{1}{\pi} \text{Sign}(\alpha) (\pi - \text{Mod}(\alpha, 2\pi)) \quad (3.20)$$

where $\alpha = k_x x - \ell\phi$, $\text{Mod}(m, n)$ is the remainder on division of m by n , and $\text{Sign}(\alpha)$ is the sign function of α , i.e. $\frac{\alpha}{|\alpha|}$. Figure (3.8) shows four different type of gratings that generate a helical beam with $\ell = 2$. For amplitude holograms, the squared grating has

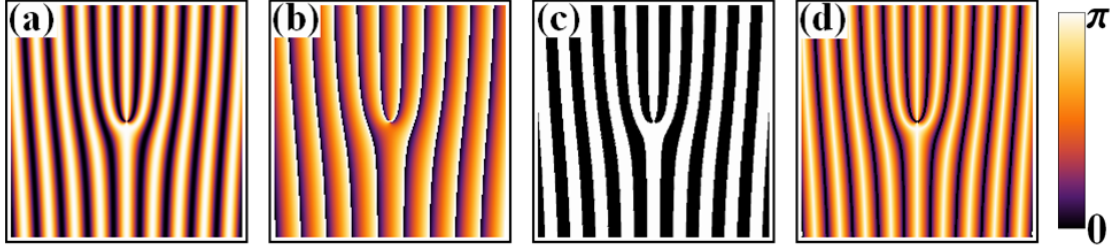


FIGURE 3.8: Different holograms pattern in order to generate a helical beam with $\ell = 2$. (a) is the sinusoidal, (b) is the blazed, (c) is the binary, and (d) is the Triangle holograms.

the maximum efficiency of around 10%, among all grating types (See Table 3.1).

The phase hologram pattern is exactly the same as the amplitude one. However, such hologram does not absorb light, so, its power transmittance is unity. For the phase hologram the Fresnel transmittance coefficient is given by

$$t(x, y) = e^{iag(\alpha)} \quad (3.21)$$

where $g(\alpha)$ is the grating type given by one of the four mentioned functions Equations (3.17, 3.18, 3.19, 3.20), and a is the phase depth of hologram.

For example, the Fresnel coefficient for a sinusoidal grating can be written, apart from a constant phase, in terms of Fourier series

$$t(x, y) = \sum_{n=-\infty}^{+\infty} i^n J_n(a) e^{i(k_x x - \ell\phi)} \quad (3.22)$$

where $J_n(a)$ is the Bessel function of order n . This expansion shows that, for a sinusoidal phase hologram, all orders of beam diffraction are present and their efficiency is equal to the square modules of $|J_n(a)|^2$. Table (3.1) shows the maximum theoretical efficiency and generated order of the amplitude and phase hologram for all possible types of gratings.

In our laboratory first we manufacture amplitude holograms, then, we change them into

TABLE 3.1: Ideal efficiency of different types of grating and different kind of holograms.

Type of grating	Amplitude Hologram		Phase Hologram	
	Generated order	Efficiency	Generated order	Efficiency
sinusoidal	zero + first orders	6.25%	all	33.85%
blazed	all	2.53%	Just first order	100%
squared	odd	10.13%	odd	40.52%
triangle	odd	4.10%	all	29.81%

phase ones by chemical bleaching procedure. In order to generate amplitude hologram, we numerically calculate a density plot of a pitch-fork hologram with a definite topological charge and diffraction angle by *Mathematica* from *Stephan Wolfram*. The dimension of simulated holograms were 1024×1024 *pixel*. Then, we simulated the computer generated holograms (CGHs) over a proper aligned 19" monitor. An ILFORD PAN F PLUS ASA 50 negative black and white film and a camera (Contax 167MT) with a standard 52 mm objective were then used to transfer the pattern on a photographic film. Photographes were taken from the a distance of 3.2 m away from aligned monitor. For our purpose, the combination of $f_{\#} = 8$ and exposure time of $\frac{1}{4}$ s gave the best result. Note that, the monitor refreshing time must be at least three times shorter than the exposure time of film. The film, then can be developed in a normal way. We used ILFORD developer (ILFOSOL3), ILFORD indicator stop bath (ILFOSTOP) and ILFORD rapid fixer (RAPID FIXER) with the recommended times and concentrations. The quality of the developed negative film can be checked via a microscope. The black and white line thicknesses must be equal for optimal efficiency. Moreover, a good amplitude hologram must have a wide range of gray levels. A very dark hologram absorbs light to much and very light hologram proved inefficient at diffracting light. So, for both cases the efficiency is low. We were able to produce amplitude holograms with 6% efficiency and 22 *lines/mm*. However, the best amplitude holograms to make a phase holograms were those with an efficiency around 1%.

A solution of 9 gr $\text{Fe}(\text{NO}_3)_3 \cdot 9\text{H}_2\text{O}$, 5 gr ammonium dichromat and 6 ml concentrated sulphuric acid into 1 liter distilled water was used for bleaching the developed negative film. Another possible bleaching solution is 10 gr mercuric chloride diluted into 1 liter of distilled water. After bleaching the developed negative film with the first solution, the bleached negatives were washed carefully with distilled water at least for 15 minutes. Then, the film was dried in a cleaned place, e.g under extractor fan. The bleaching solution is toxic, so, all process must be done in chemical hood.

A typical efficiency around 15% was achieved at green wavelength, 532nm, with this kind of film and bleaching solution.

3.5 q -plate

All methods presented in the previous sections to generate OAM were based on the direct manipulation of the beam's phase front only, without touching the polarization of the beam. We considered the beam OAM as an independent degree of freedom. Indeed, the sum of SAM+OAM, i.e. total angular momentum, is one of the possible constants of motion. Nevertheless, they cause different “*rotational*”-like motions. Before 2006, physicists considered them as an uncoupled degrees of freedom and no significant interaction between SAM and OAM was normally expected.

Marrucci et al. [19] showed that there is an interaction between SAM and OAM in an inhomogeneous anisotropic medium. The essential concept of this process is lying under the well-known Pancharatnam-Berry phase context. When a polarization state of a given beam adiabatically follows a closed path over the SAM Poincaré sphere, an additional phase given by half of the closed path's solid angle will appear with respect to initial optical field.

Let us consider an optical field passing through a transverse varying birefringent plate with a uniform thickness. If the input and output polarization states are homogenous, an inhomogeneous geometrical phase, then, is induced by the plate, thus corresponding to a modification of the output phase front. Clearly, based on the input polarization state the output phase front can be controlled. This is the heart of the SAM-OAM interaction optical elements.

We consider an uniaxial birefringent plate having an uniform thickness for a light propagating in the longitudinal z -direction, but, a transversely inhomogeneous optical axis laying in the transverse plane. For our purpose we assume that the optical axis of the uniaxial birefringent depends on the azimuthal angle only:

$$\alpha(r, \phi) = q\phi + \alpha_0 \quad (3.23)$$

where q is the topological charge of the plate, and α_0 is a real constant value. This pattern requires a singularity at the center of plate. For an integer or semi-integer value of q there will be no discontinuity in the transverse plane. q is an important parameter which defines the plate topology, i.e. the uniaxial varying geometry. Due to importance of topological charge q , this plate was named “ q -plate”. Some interesting topologies of the q -plate are shown in Figure (3.9). A complete analytical analysis of the light propagation inside a q -plate is postponed to the next chapter (4.3). However, based on the Jones formalism, in a good approximation, the q -plate action at least for a plane wave input beam can be readily calculated.

The Jones matrix to be applied on the field at each point over the q -plate transverse

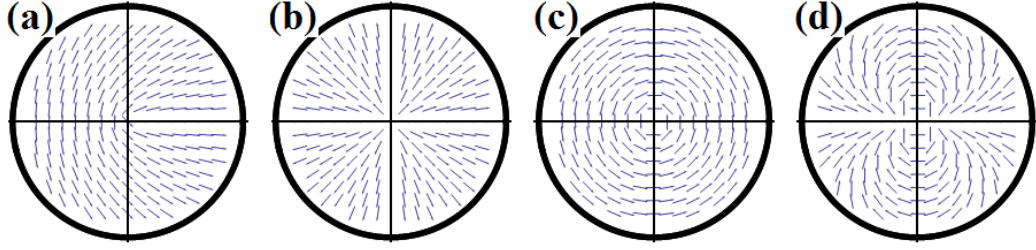


FIGURE 3.9: Four different topologies of q -plate. (a) $(q, \alpha) = (\frac{1}{2}, 0)$, (b) $(q, \alpha) = (1, 0)$, (c) $(q, \alpha) = (1, \frac{\pi}{2})$ and (d) $(q, \alpha) = (2, 0)$. The vectors are defining the liquid crystal orientation on the transverse plane.

plane is given by

$$\begin{aligned} \widehat{U}_q^\delta &= R(-\alpha) \cdot \begin{pmatrix} e^{i\frac{\delta}{2}} & 0 \\ 0 & e^{-i\frac{\delta}{2}} \end{pmatrix} \cdot R(\alpha) \\ &= \cos\left(\frac{\delta}{2}\right) \begin{pmatrix} 1 & 0 \\ 0 & 1 \end{pmatrix} + i \sin\left(\frac{\delta}{2}\right) \begin{pmatrix} 0 & e^{2i\alpha} \\ e^{-2i\alpha} & 0 \end{pmatrix} \end{aligned} \quad (3.24)$$

where $R(\alpha)$ is the 2×2 rotation matrix in the transverse plane about angle α , and δ is the q -plate optical retardation. This action is now rewritten in the circular polarization basis (2.39).

When a left-circular polarized light passes through the q -plate, we will have two components of light, based on the q -plate optical retardation at the plate exit face. A component of the beam remains unchanged, i.e., it is a non-converted part, and other part comes out with the right-circular polarization state and an additional phase transverse-modulation which corresponds to the presence of the OAM $m = 2q$.

$$\widehat{U}_q^\delta \cdot |L\rangle = \cos\left(\frac{\delta}{2}\right) |L\rangle + i e^{i(2q)\alpha_0} \sin\left(\frac{\delta}{2}\right) |R\rangle e^{i(2q)\phi} \quad (3.25)$$

It can be easily shown that by changing the input polarization state to the right circular polarization, the output phase front changes to $m = -2q$ with the left circular polarization. In other words, the OAM value generated by the plate depends on the input polarization state. So, the q -plate is an optical device to generate OAM based on the SAM-OAM interaction. As we will show, the optical retardation δ of the q -plate can also be controlled, e.g. by exciting a mechanical pressure, applying an electric field or changing the plate temperature.

A q -plate with a “ π ” optical retardation δ (half of wavelength) is hereafter called a “tuned” q -plate. The tuned q -plate’s acts just as a pure converter of SAM-to-OAM. So, the left (right) circular polarized beam converts to the right (left) circular polarization with a well-defined values of OAM which is two times of the plate’s topological charge

$+2q$ ($-2q$). This process may cause a torque, due to change of the total angular momentum, on the plate. In order to calculate this torque it will be convenient to trace out the total angular momentum of initial and final beams. For instance, for the above mentioned process, the total changes of angular momentum in the direction of propagation is equal to

$$\Delta j_z = \pm 2(q - 1)\hbar \quad (3.26)$$

per photon. The \pm sign are denoting these values for left and right circular polarization input beam, respectively. It is zero for the case of $q = 1$ topological charge, radial or azimuthal orientation of uniaxial birefringent. This result was expected from the physical cylindrical symmetry of the $q = 1$ -plate. In this case one can talk of a pure SAM-To-OAM conversion (STOC) taking place in the optical beam.

3.5.1 Manufacturing a q -plate

The uniaxial liquid crystal is a good candidate to generate transverse spatial varying patterns. Indeed, liquid crystal can be easily aligned by the electrostatic interaction with surfaces. In our laboratory, we are able to manufacture a plate with a unit topological charge, i.e. circular oriented pattern. Our plate is made of a $6 \mu\text{m}$ thick film of E7 liquid crystal from Merck, sandwiched between two fused silica glasses. These two glasses were coated with a proper mixture of PI2555 polyimide from DuPont for inducing the planar alignment. In order to introduce the unit topological charge to the liquid crystal molecules the glasses were rubbed circularly. The two plate singularities, after that, were precisely superimposed. This process was done with a help of a setup which gives control of all degrees of freedom to the plates. A microscope was inserted to check the position of two singularities during the positioning. In the meanwhile, on the same setup, the parallelism of the plates was precisely controlled by reflection of the HeNe laser light beam from the two inner surfaces of the glasses. We, then, inject liquid crystal between the plates. By time, liquid crystal molecules find the minimum energy interaction between these two circularly rubbed plates. The preferential direction for liquid crystal is circular at the glass surfaces. The used polyimide substrates align liquid crystal molecules parallel to the glasses surface for both plates. However, other kinds of surfactants, for example DMOAP, were also used in our laboratory to prepare the orthogonal alignment of liquid crystal at glass surface (called “homeotropic” alignment). In practice, these two kinds of q -plates, i.e. planar-planar and planar-orthogonal (also called “hybrid”), are different. Figure (3.10) shows the structure of two different type of q -plates under a microscope. In order to test the q -plate operation, we measured the beam phase front via Mach-Zender interferometer. A Verdi laser TEM₀₀ Gaussian

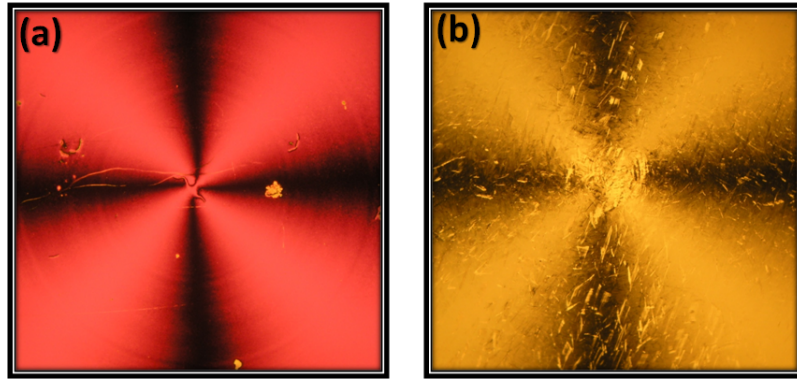


FIGURE 3.10: The fringes of q -plates sandwiched between two crossed polarizers. q -plate made by (a) ultra-violet (UV) technique (b) rubbing technique.

beam was split in two beams; signal and reference. The signal was switched to left circular polarization beam by means of a proper aligned QWP. Then, it passed through the q -plate. A converted part of output beam then was chosen with another QWP and polarizer. This QWP and polarizer selected the left circular polarization (orthogonal polarization). Finally, the signal beam was superimposed with reference beam. Figure (3.11) shows the interference pattern taken by CCD camera.

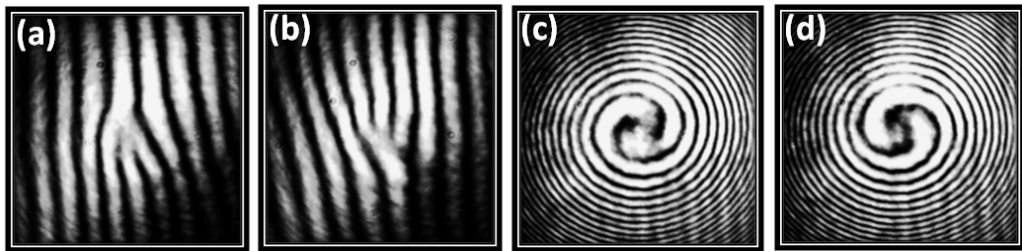


FIGURE 3.11: Interference patterns of outgoing beams from the q -plate with planar and spherical TEM_{00} beams for two different input polarization states. (a) and (b) Interference patterns of the Left and right circularly polarized input beams with a planar TEM_{00} , (c) and (d) interference patterns of the Left and right circularly polarized input beams with a spherical TEM_{00} light, respectively [44].

3.5.2 Thermal tuning of the q -plate and its characterizations (Karimi et al. [45])

High efficiencies in producing and detecting the light OAM are highly desirable in all circumstances where only few photons are at disposal. Examples are weak signals coming from far sources, such as astronomical ones [45] or after propagation in highly absorbing media, or in quantum information applications [31]. Achieving high efficiencies, however, requires accurate tuning of the q -plate retardation δ . In order to tune the optical

retardation δ and thus optimize the q -plate efficiency, in this subsection we adopted a method based on controlling the material temperature, which presents good features in terms of a realization simplicity and stability of the obtained retardation [46]. However, temperature tuning is not the only way to tune the optical retardation of the q -plate and there are some other methods like applying uniform electric field and uniform pressure over the plate.

We used the Spin-to-OAM conversion (STOC) process for transforming an input TEM_{00} laser beam into a beam having OAM $\ell = \pm 2$. The transmittance T of our q -plate was measured to be 88%, with the losses arising from scattering due to manufacturing imperfections and from the lack of antireflection coating on the cell bounding glasses. The

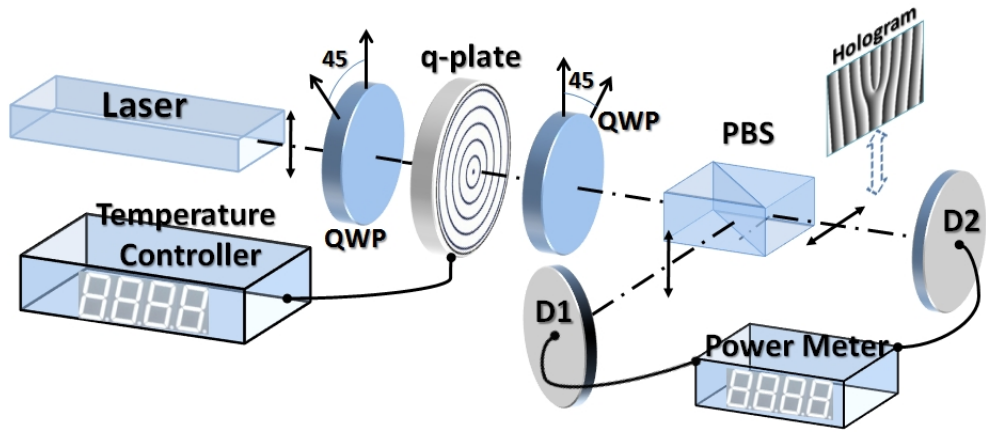


FIGURE 3.12: Setup to measure the STOC efficiency and the state purity. Legend: QWP - quarter-wave plate; PBS - polarizing beam-splitter. The fork hologram was inserted on the converted beam arm for verifying the degree of purity of the OAM $\ell = 2$ mode generated on the output [46].

optical setup used to measure the STOC efficiency of our q -plate as a function of its optical retardation is shown in Fig. (3.12). The input light was a linearly polarized TEM_{00} laser beam generated by a frequency-doubled continuous-wave Nd:YVO₄ ($\lambda = 532$ nm). After changing the polarization into left-circular (L) by a suitably oriented quarter wave plate (QWP), the beam was made to pass through our controlled-temperature q -plate. In the q -plate, a fraction of the photons will undergo the STOC process and will therefore emerge with right-circular (R) polarization and OAM $\ell = 2$, and the others will remain in the OAM $\ell = 0$ and with L polarization. For arbitrary q -plate tuning, the transverse intensity pattern of the beam emerging from the q -plate exhibits a central spot, corresponding to the light fraction that is left in the initial OAM state $\ell = 0$, surrounded by a single ring, corresponding to the light converted into the OAM $m = 2$ mode (doughnut beam) at the far field. By inserting in the output beam a second QWP

and a polarizing beam-splitter (PBS) oriented so as to select the R -polarization for, say, the transmission output, a pure doughnut beam is obtained. The reflected output of the PBS shows instead only the central spot (unconverted light). If P_{in} is the total input power, the respective powers of the coherently converted and unconverted components, $P_{R,2}$ and $P_{L,0}$, are expected to depend on the optical retardation δ according to the following Malus-like laws [47, 48]:

$$P_{R,2} = P_0 \sin^2 \frac{\delta}{2}, \quad P_{L,0} = P_0 \cos^2 \frac{\delta}{2} \quad (3.27)$$

where $P_0 = TP_{in}$ is the total power transmitted coherently by the q -plate. To adjust the retardation δ , the temperature of the q -plate was varied while measuring the power of the two output beams of the PBS. The results are shown in figure. (3.13), together with best-fit curves based on Eqs. (3.27), assuming a second-order polynomial dependence $\delta(T) = a + bT + cT^2$ and adding a constant offset of 0.5% that accounts for the finite PBS and wave-plates contrast ratios. When the PBS-transmitted power (full squares in Fig. (3.13)) reaches its maximum, we obtain the optimal STOC and almost all photons emerge in the $\ell = 2$ OAM state. More precisely, in this optimal situation, about 99.2% of the beam power is transmitted by the PBS, and after taking into account the finite contrast ratio of the waveplates and PBS (as measured without the q -plate), the actual q -plate efficiency in inverting the optical polarization is estimated to be 99.6%. Near the minima of the same curve, the STOC process is minimum and almost all photons emerge in the original $\ell = 0$ state. To test the purity of the OAM eigenmode generated by

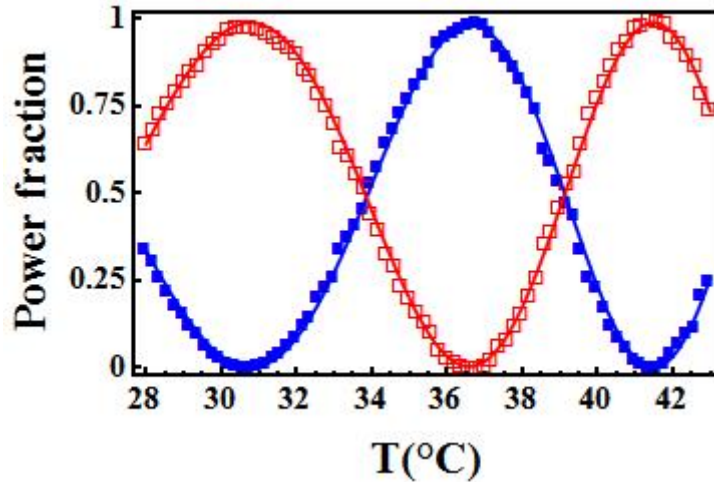


FIGURE 3.13: STOC power fraction $P_{R,2}/P_0$ (blue squares) and no STOC power fraction $P_{L,0}/P_0$ (red squares) as functions of the q -plate temperature. The curve is the best fit obtained as explained in the text [46].

our q -plate, at the optimal temperature we inserted along the beam a double pitchfork hologram as OAM-mode splitter [18, 20] and, on the first-order diffracted beam we

selected the central spot by a suitable iris placed before the detector. After suitable calibration of the detection efficiency, the measured OAM $\ell = 2$ mode content fraction was estimated to be $F = 97.2\%$ (in quantum optics, F is the squared “fidelity”, i.e. the overlap with the desired mode $\ell = 2$), so that the overall q -plate efficiency in generating a pure OAM $\ell = 2$ mode is $\eta = 97.2\% \times 99.6\% = 96.9\%$ (this value is net of reflection and scattering losses in the q -plate; including all losses, the efficiency of our q -plate is 85%, a figure which could be however easily improved to more than 90% by simply adding antireflection coatings). Moreover, we note that in order to invert the sign of the generated OAM value ℓ (e.g., from $+2$ to -2) with our setup it is enough to switch the input and output polarizations to the orthogonal ones. This can be achieved at gigaHertz rates by means of Pockel cells. No switching capability is instead possible with passive holograms, while computer-controlled spatial light modulators (SLM) can achieve at most switching rates of the order of few kiloHertz.

3.5.3 q -plate as a mode sorter (Karimi et al. [45])

In this subsection, we present a setup for sorting the four modes given by combining the two OAM modes $\ell = 2$ and $\ell = -2$ and the two orthogonal polarizations L and R . The setup is similar to the previous one, except that the input laser beam was made to pass through a SLM driven with a computer generated hologram (CGH) for determining its input OAM state. The temperature of the q -plate was held fixed at the optimal value for maximum STOC efficiency. We used double-pitchfork CGHs to produce alternatively $\ell = 2$ and $\ell = -2$ OAM eigenstates in the input. The first QWP was also rotated so as to produce, alternatively, right-circular and left-circular polarizations. In this way,

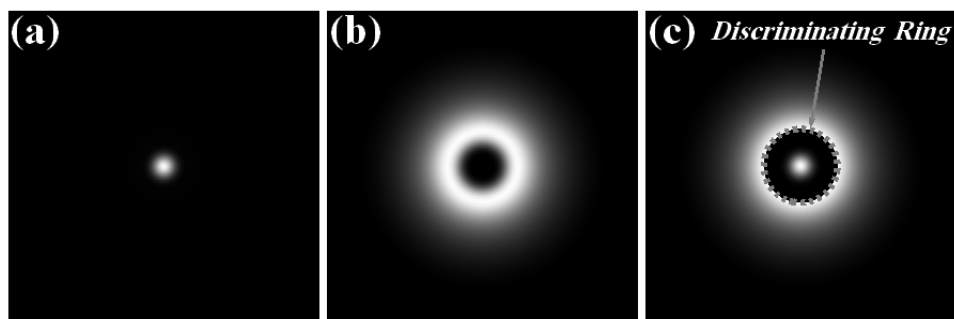


FIGURE 3.14: Calculated far-field patterns of OAM modes $\ell = 0$ and $\ell = 4$ generated by the q -plate for input OAM $\ell = \pm 2$ (The input beam was assumed to HyGG $_{-2,\pm 2}(r, \phi, 0.1)$ (2.5.2.2) mode). The dashed circle shows the discriminating area used in the balanced mode sorter [46].

we created in sequence the four photon states $|L, 2\rangle$, $|L, -2\rangle$, $|R, 2\rangle$, $|R, -2\rangle$, where the first symbol in the ket denotes the polarization and the second is the ℓ value of the

photon OAM. Because the STOC process is complete in a tuned q -plate, after passing through the q -plate these four states are expected to change respectively into $|R, 4\rangle$, $|R, 0\rangle$, $|L, 0\rangle$, $|L, -4\rangle$. The QWP after the q -plate, changes these states into $|H, 4\rangle$, $|H, 0\rangle$, $|V, 0\rangle$, $|V, -4\rangle$, respectively, so that the two states $|H, 4\rangle$, $|H, 0\rangle$ are transmitted by the PBS and the other two states $|V, 0\rangle$, $|V, -4\rangle$ are reflected. We see that owing to the q -plate, the two states in each of the reflected and transmitted beam have a different value of photon OAM ($\ell = 0$ and $\ell = 4$). After propagating in the far-field (or in the focal plane of a lens), these two modes can then be separated by exploiting their different radial distribution, i.e., a central spot for $\ell = 0$ and an outer ring for $\ell = 4$, as shown in Fig. (3.14), thus finally sorting all four initial spin-orbit modes into separate beams. The radial sorting can be obtained, for example, by means of a mirror with a hole at its center. We note that in our measurements we are using the PBS only for discriminating the two input polarizations. In many applications, the input polarization state is fixed and known and one is interested only in sorting the OAM $\ell = \pm 2$ modes. In this case, the PBS is unnecessary, the input light can be always made L -polarized, by suitable wave plates, and the output beam will then be only R -polarized. The OAM sorting is then still based on the radial-mode separation in the far field. The efficiency of this mode-sorter, here defined as the fraction of the optical power in a given eigenmode to be sorted that is directed in the *correct* output mode is however not 100%, because of the radial mode overlap, leading to some energy going in the “wrong” OAM output mode. This also leads also to a finite contrast ratio, i.e., to cross-talk between the input channels. In Table (3.2) we report the measured efficiencies and contrast ratios for the four input spin-orbit base states previously mentioned, with a discriminating hole radius chosen so as to balance the output efficiencies for opposite input OAM (see Fig. (3.14)). The measured efficiency of the q -plate as mode sorter is of about 81.5% (72% with q -plate losses), i.e., 2.7 times larger than for the best available holograms ($\approx 30\%$ efficiency, as blazing cannot be used for multiple outputs). The extinction ratio due to radial overlap between $\ell = 0$ and $\ell = 4$ OAM modes can be improved by introducing a suitable opaque belt mask that cuts away the overlapping region of the two modes, although at the expense of a reduced efficiency. In principle the contrast ratio can be made arbitrarily large. Theoretically, we estimate a contrast ratio $> 10^3$ for an efficiency of about 50% and $> 10^6$ for an efficiency of 10% [45]. Increasing the contrast ratio at the expense of efficiency can be useful in many quantum optics applications where good fidelity is required [32]. We note that the radial-overlap problem leading to cross-talk is not unique of the q -plate approach; a similar problem and an equivalent efficiency/contrast-ratio tradeoff is present also with hologram-based OAM sorting. We also tested our q -plate mode-sorter with coherent superpositions of $m = +2$ and $m = -2$ OAM modes (obtained with suitable CGHs), obtaining results

TABLE 3.2: The QP's efficiency as a mode sorter.

Input state	Output state	Efficiency	Extinction ratio
$ L, 2\rangle$	$ R, 4\rangle$	81.1%	$\approx 4.6:1$
$ L, -2\rangle$	$ R, 0\rangle$	81.8%	$\approx 4.5:1$
$ R, 2\rangle$	$ L, 0\rangle$	81.6%	$\approx 4.7:1$
$ R, -2\rangle$	$ L, -4\rangle$	81.5%	$\approx 4.6:1$

consistent with the efficiencies reported in Table (3.2).

3.5.4 Schemes for generating higher orders of OAM

The q -plate is highly transparent and can be cascaded along the beam to produce arbitrary values of the OAM [44]. The tuned q -plate in order to generate higher order of OAM is necessary and non-tuned q -plate cannot be used in the cascaded configuration. Indeed, a suitable configuration of waveplates and q -plates can be used to generate an arbitrary high value of OAM. In order to clarify this point we will start with a simple example. Let us consider a HWP sandwiches between two tuned q -plates with unite topological charge. When a left circularly polarized beam with no OAM, $|L, 0\rangle$ enters to this configuration, the first q -plate, then, generates a right circular polarized beam with $\ell = 2$, $|R, +2\rangle$. The HWP just inverts the polarization state. The second q -plate instead changes both SAM and OAM states to $|R, +4\rangle$. By removing the HWP the OAM output state will be $\ell = 0$. Marrucci et al. [44] presented a smart way to generate whole even number of OAM. They used a Pockel cell (PC) followed by a QWP to change the polarization state from Left to Right and vice versa. Then a q -plate were used to transfer the SAM state to OAM state and finally a QWP was used to return back the polarization state to the linear states. By cascading this element one will be able to generate whole even value of angular momentum. Furthermore, there is an issue regarding to the beam radial profile which must be addressed. The free-air propagation changes the radial profile of outgoing beam from the q -plate.

However, we also developed another way to generate the $-4, -2, +2, +4$ OAM states by inserting a q -plate in one arm of Sagnac interferometer as will be discussed in section (4.6.1).

Chapter 4

The OAM propagation and classical application

4.1 Introduction

In the previous chapter, we introduced some well-known techniques to generate, manipulate and detect light orbital angular momentum. We presented basic and simple views for explaining the working principle of these devices. In our elementary pictures we did not touch the other important degrees of freedom of light, i.e. the beam radial number. The beam radial index is as important as spin and OAM indices. In many practical applications of OAM in the quantum and classical regime of light, the SAM, OAM and radial index may be are strongly entangled. Therefore, the beam is not a pure OAM and SAM eigenstate. Indeed, the photon coherency or density matrix can be reconstructed in these three individual degrees of freedom's Hilbert spaces. By neglecting the radial part, the output beam is considered in the reduced Hilbert space of SAM and OAM, which is not the real physical state. The radial part plays an important role independent of the OAM's generator and detector. The transverse degree of freedom plays an essential role in the spatial filtering of light beams. Even, two given beams with the same values of OAM may have different transverse profiles. This difference can be reconduced to a different distinction of radial index number.

In order to handle such kind of issues we must study and calculate the beam radial profile generated by different type of OAM generator devices. In determining the light propagation kernel for different types of OAM generators will be the aim of this chapter. Of course, we expect to obtain different propagation kernels, and radial profiles for different OAM generators.

Finally, we present some new applications of the q -plate as an OAM generator and a special radial profile generator in the classical optics regime. The q -plate with half topological charge can be used with a system of high numerical aperture and optical phase mask to generate a very narrow beam with a waist radius below the diffraction limit, which is called “needle beam”. Furthermore, I will show how two classical bits of information can be encoded over OAM state of a photon, independent of the SAM state. Alice (sender) uses a q -plate to generate one of the four states on the OAM space, i.e. $-4, -2, +2, +4$, and Bob (receiver) can use a 2D pitch-hologram to project each state over 4 individual detectors.

4.2 Outgoing wave from the pitch fork hologram (Karimi et al. [13])

The pitch fork holograms are widely used for generating and detecting the OAM of a light beam. These kind of holograms provide a static (passive) generator or detector of OAM, and they cannot be used for switching dynamically among different OAM states. However, an optoelectronic device, named spatial light modulator (SLM), recently produced commercially can instead be used to obtain a reconfigurable holograms, allowing for dynamical control of the OAM state, although at a slow rate ($\lesssim 1$ KHz). The SLM is made as a nematic liquid crystal display. The normal dimension of each pixel of the SLM is of about $9 \mu m$. The optical phase retardation of each pixel can be controlled in the interval $[0, 2\pi)$ with 256 steps, corresponding to a GrayLevel color scale, by applying a voltage which is driven by a personal computer (PC) graphic card. In fact, when a hologram with a correct dimension is displayed on the PC screen, a well-defined voltage corresponding to the color of each pixel on the screen in the gray scale level is applied to the same pixel of the SLM. This voltage changes the liquid crystal alignment inside the cell. Due to this new orientation of the liquid crystal, the optical retardation of the cell also changes. So, pixel by pixel, the optical retardation is modulated according to the displayed hologram color. So, the SLM is working as a pure phase object. The hologram pattern can be changed by changing the displayed pattern. The SLM speed is limited by the graphic card and by the response time of the liquid crystal molecules. Moreover, the SLM’s efficiency is strictly dependent on the beam polarization state. The SLM has a wide range of applications in optical trapping and optical tweezers when a beam shape control is needed. Due to availability of such kind of optical elements the computer generated holograms are widely used to generate and detect light OAM. So, it will be worth of investigation to study the outgoing wave from a pitch-fork holograms.

A pitch fork hologram with any different encoded pattern cannot produce a pure LG mode [20]. Indeed, the output beam must have a well-defined azimuthal index number. But, there is not a rule to define a specific radial index number (only azimuthal index is well-defined for a pitch-fork hologram). In order to face this problem, we have considered a perfect blazed hologram with a well-defined value of OAM = ℓ , in which the whole impinging power is diffracted into the first order of diffraction. We choose the case of a blazed hologram just for simplifying our calculations, but our approach can be extended to any type of holograms. We suppose that this blazed hologram is illuminated with a $\text{LG}_{p,m}$ beam. The optical field in the first order of diffraction exactly after the hologram is, then, given by

$$\mathbf{E}_t(r', \phi'; 0) = \text{LG}_{p,m}(r', \phi', 0) e^{i\ell\phi'} \quad (4.1)$$

where we have supposed that the hologram is thin enough and that the beam waist of the LG mode is located on the hologram, $(r', \phi', 0)$ are the cylindrical coordinates at that frame. The LG beam is a solution to the PWE and carries finite power. The hologram output beam also carries finite power. So, we have chosen the free-air paraxial Fresnel propagator to calculate the optical field at any plane far from the holograms. The pupil function (4.1) of this propagator is given by a phase singularity due to the presence of hologram and input LG beam. The optical field, then, in any transverse plane is given by

$$\mathbf{E}_t(r, \phi; \zeta) = \left(-\frac{i}{\pi\zeta}\right) \int r' dr' \int d\phi' e^{\frac{i}{\zeta}(r^2+r'^2-2rr'\cos(\phi-\phi'))} \text{LG}_{p,m}(r', \phi', 0) e^{i\ell\phi'} \quad (4.2)$$

where we have used the dimensionless coordinates (See 2.5). There is no unique function to cover all integrals for different LG beams. However we consider an important type of impinging LG beam: $\text{LG}_{0,0}$ that is the normal gaussian $\text{TEM}_{0,0}$. The $\text{TEM}_{0,0}$ output is commonly used to generate OAM. As we will show, the outgoing wave from an OAM generator has a maximum power at the zero order of radial number.

In the case of $\text{TEM}_{0,0}$ input beam the outgoing wave at distance ζ from the hologram is

$$\mathbf{E}_t(r, \phi; \zeta) = C_\ell \zeta^{-|\ell|} (\zeta + i)^{-(|\ell|/2+1)} r^{|\ell|} e^{-\frac{ir^2}{(\zeta+i)} + i\ell\phi} {}_1F_1\left(\frac{|\ell|}{2}, |\ell| + 1; \frac{r^2}{\zeta(\zeta + i)}\right) \quad (4.3)$$

where C_ℓ is a normalization constant value dependent on ℓ . This field is a special category of HyGG modes family introduced in chapter (2), i.e. when p is replaced by $-|\ell|$. The main properties of the HyGG modes have been presented in chapter (2) or reference [13]. So, we could say that the pitch-fork hologram generates a new type of paraxial wave modes, i.e. HyGG $_{-|\ell|,\ell}$ modes. The hologram topology is defined only by the ℓ integer value. So, we could expect that the output beam must be also defined just

TABLE 4.1: The outgoing beam power spectrum from a pitch fork hologram in the LG modes basis. ℓ indicates the topological charge of hologram and q shows the LG radial index number.

	$q = 0$	$q = 1$	$q = 2$	$q = 3$
$\ell = 1$	0.785	0.098	0.036	0.019
$\ell = 2$	0.500	0.166	0.083	0.050
$\ell = 3$	0.294	0.165	0.103	0.070

by the value of this integer number. It may be interesting to find this beam spectrum in the LG mode basis. The expansion coefficients are given by equation (2.56) by replacing $p \rightarrow -|\ell|$.

$$A_q = \sqrt{\frac{1}{q!(q+|\ell|)!} \frac{\Gamma(|\ell|/2 + 1)\Gamma(|\ell|/2 + q)}{\Gamma(|\ell|/2)}} \quad (4.4)$$

where $\Gamma(x)$ is the gamma function. So the power which the zeroth mode, $\text{LG}_{0,\ell}$, carries is equal to

$$P_0^q = \frac{\Gamma^2(|\ell| + 1)\Gamma^2(|\ell|/2 + q)}{|\ell|!\Gamma^2(|\ell|/2)} \quad (4.5)$$

Table (4.1) shows this power spectrum for several pitch fork holograms. As you can see from the table (4.1), by increasing the hologram topological charge the higher radial orders of LG modes are excited more. So, we expect a bigger doughnut for large hologram topological charges. Moreover, the LG beams are propagation shape invariant. Of course, the output beam from a pitch-fork hologram is a superposition of infinite LG beams with a fixed azimuthal index number and different radial numbers. Since these beams have different *Gouy* phases, their superposition, i.e. the $\text{HyGG}_{-|\ell|,\ell}$ modes in this case, is not shape invariant anymore. Their intensity profile changes dramatically

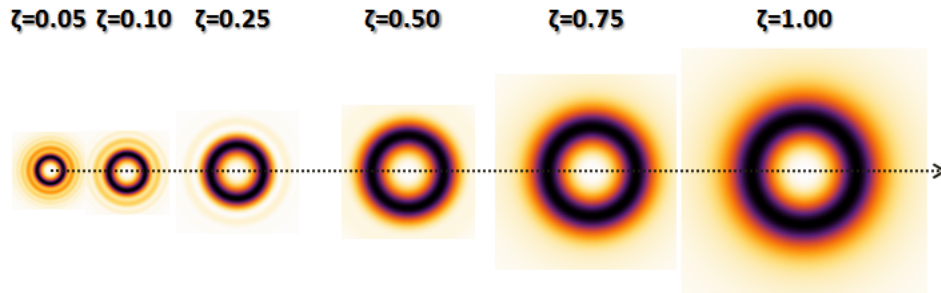


FIGURE 4.1: The free-air propagation of the outgoing beam from a pitch-fork hologram. The impinging beam and hologram topological charge are considered TEM_{00} and $m = 2$, respectively.

by free-space propagation and after the Rayleigh range they become brilliant doughnuts

(See figure (4.1)).

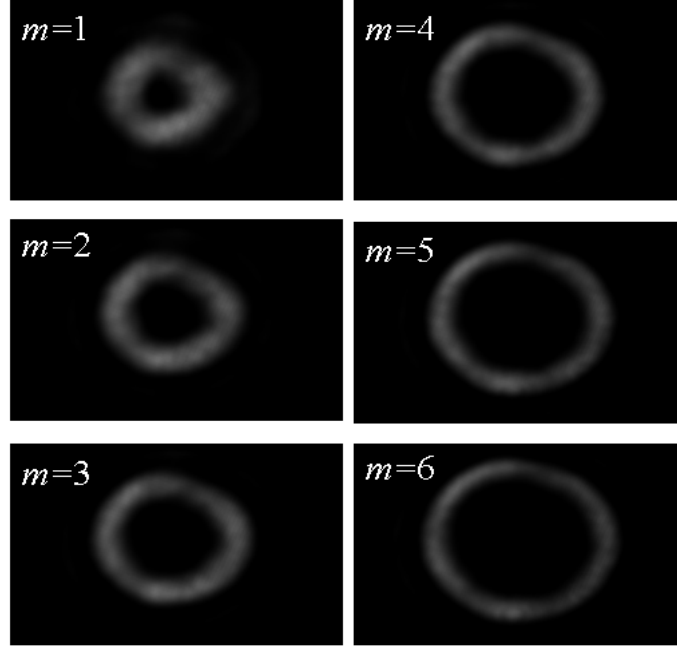


FIGURE 4.2: Experimentally observed intensity distributions of the $|\text{HyGG}\rangle_{-m,m}$ mode for $m = 1, \dots, 6$ in the transverse plane $z = 0.18z_0$. The Rayleigh range was $z_0 = 747.4$ cm.

In order to test our theory, we performed some measurements on the beam propagation profiles. In our experiment, a TEM_{00} linearly polarized laser beam from a frequency doubled $Nd:YVO_4$ ($\lambda = 532$ nm, Model Verdi V5, Coherent) was used to illuminate a grey scale computer generated hologram (CGH) sent onto the LCD microdisplay of an SLM (HoloEye Photonics LC-R 3000), with 1920×1200 pixels in a rectangle 18.24×11.40 mm wide. The SLM was located in the waist of the incident beam. We performed two series of measurements, according to the beam waist values w_0 at the SLM position. The two values were $w_0 = 1.1$ mm and $w_0 = 0.1$ mm, corresponding to Rayleigh ranges $z_0 = 747.4$ cm and $z_0 = 7.8$ cm, respectively. We focused our attention on the HyGG modes with $p = -|\ell|$. In accordance with the theoretical predictions, we observed an intensity profile in the transverse plane essentially made of a single bright annulus, whatever the value of ℓ we used or the observation z -plane. Some instances of the observed intensity profiles are shown in figure (4.2). The ring diameter of the beam as a function of ℓ is reported in figure (4.3). The diameter d of the ring was defined as the maximum distance between any two opposite maxima of the intensity profile. The scaling law of d versus ℓ turned out to be in good agreement with the theoretical predictions. We measured also the ratio between the diameter $d(z)$ of the luminous ring and the gaussian beam size $w(z)$ at different z -planes. The measurements were made by switching on and off the CGH to

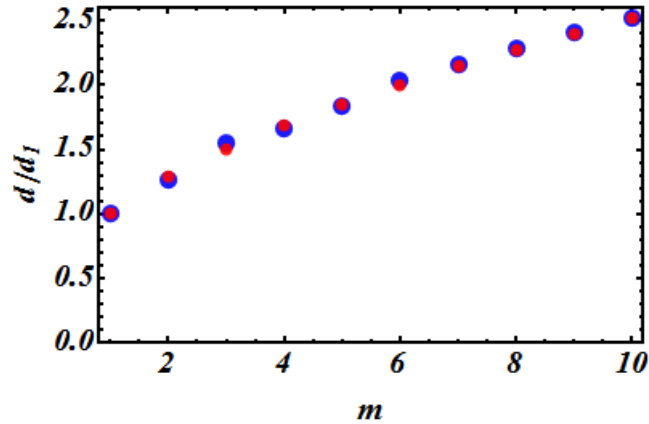


FIGURE 4.3: The ring diameter d of the $|\text{HyGG}\rangle_{-m,m}$ mode for $m = 1, \dots, 6$ measured at plane $z = 0.18z_0$. The Rayleigh range was $z_0 = 747.4$ cm. The reported values of the diameters were scaled with respect to the value d_1 for $m = 1$. blue \bullet – theory, red \bullet – experiment.

compare the intensity profile of the HyGG mode with the gaussian profile TEM_{00} beam profile at the same plane. Figure (4.4) shows that the ratio $d(z)/w(z)$ was the same in all z -planes, as predicted by theory when $z > z_0$. The constant value of the ratio d/w obtained from the experiment was 3.1 ± 0.3 , which is close to the theoretical prediction $d/w = 3.6$.

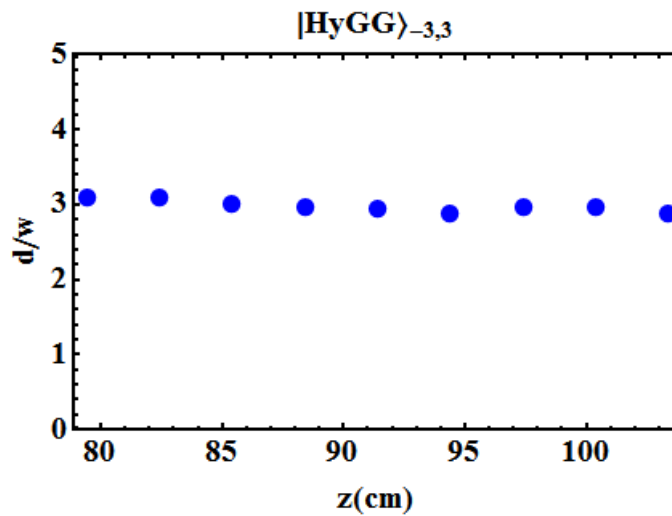


FIGURE 4.4: The ratio between the diameter $d(z)$ of the $|\text{HyGG}\rangle_{-3,3}$ mode and the $1/e^2$ intensity radius $w(z)$ of the generating TEM_{00} gaussian beam as a function of z . The Rayleigh range was $z_0 = 7.8$ cm.

4.3 Propagation of wave inside the q -plate (Karimi et al. [46])

We presented an elementary approach to the q -plate action in the previous chapter based on the Jones analysis. In this approach, we have considered the q -plate as an optical element in which the SAM of the impinging light converted into the OAM by the flipping the output beam polarization state. Based on the plate's optical retardation, the q -plate action on the circular polarized light beam is a superposition of two circular polarization states: a portion of light comes out unchanged from the q -plate and the other part comes out with flipped circular polarization and an OAM twice of the plate topological charge, its sign depending on the input polarization.

In such approach we considered a very thin q -plate in which when a light beam passes through the plate, its intensity profile at the exit face does not change at all. In this picture the q -plate acts as a pure phase object, introducing a phase factor $e^{\pm 2iq\phi}$, with the sign determined by the input polarization state. Actually, the intensity profile also changes in the q -plate due to the presence of the singularity at the center of the plate. A dark hole at the beam center, independent of input intensity profile of plate's optical retardation, due to strong diffraction (scattering) from the disordered birefringent molecules at the center is expected.

The first attempt to find the propagation kernel inside the plate with topological charge and radial index number for a Gaussian input beam was done by Calvó and Picon [49]. Their approach is analogues to what we have presented in the previous section (3.5.1). They consider a small element of the plate located far enough from the singularity center. In this small region the optical axes of the birefringent is uniform and constant. For this small element, one can solve the light propagation inside the uniform plate. Of course, two waves associated to the ordinary and extraordinary optical axis are expected inside the q -plate. The propagation kernel for a transverse monochromatic optical field with wave vector k , by using the Fourier integral in the paraxial approximation can then be easily found

$$K(\rho, \rho'; z) = \left(\frac{F_o + F_e}{2} \right) \hat{\mathbf{l}} + \left(\frac{F_o - F_e}{2} \right) R(\alpha) \cdot \hat{\sigma}_z \cdot R(\alpha) \quad (4.6)$$

with

$$\begin{aligned} F_o &: = e^{ikn_o z + \frac{ikn_o z}{2}(\rho^2 + \rho'^2 - 2\rho\rho' \cos(\phi - \phi'))} \\ F_e &: = e^{ikn_e z + \frac{ik(n_o^2 + n_e^2)z}{4n_e}(\rho^2 + \rho'^2 - 2\rho\rho' \cos(\phi - \phi'))} \\ &\times e^{\frac{ik(n_o^2 - n_e^2)z}{4n_e}(\rho^2 \cos 2(\alpha - \phi) + \rho'^2 \cos 2(\alpha - \phi') - 2\rho\rho' \cos(2\alpha - \phi - \phi'))} \end{aligned} \quad (4.7)$$

where n_o , n_e denote the ordinary and extraordinary refractive indices, F_o , F_e are the ordinary and extraordinary Fresnel kernels, α denotes the angle of the optical axis of the plate with respect to the x -axis, $\hat{1}$, $R(\alpha)$ and σ_z are the 2×2 identity, rotation and pauli matrices, respectively. They could show that when a light beam propagates inside the q -plate produces two distinct fields: a beam which preserves the input polarization state (the first term of Eq. (4.7)) and the second part that rotates the input polarization state (the last term of Eq. (4.7)). However, in both cases the radial profiles are modified by the ordinary and extraordinary Fresnel propagators. They applied this kernel to the case when α (the optical axes of small element) changes coordinate dependently. They claimed that the replacement of $\alpha \rightarrow q \arctan(y/x)$ is an excellent approximation as long as α varies slowly on the wavelength scale of the input beam. However, this approach is a rough approximation. From the beginning, the Fresnel kernel has been found for a case where α is constant and this expansion is only valid if α is not position-dependent. For the case where α is a function of (x, y) , that is our case, this Fourier expansion fails. In fact, the formal replacement $\alpha \rightarrow \phi(x, y)$ is justified only if the function $\alpha(x, y)$ varies smoothly over the optical wavelength scale (the so-called geometric optics approximation (GOA)) [49], which is not true in the present case, because no unique length scale is defined by the function $\arctan(y/x)$. Moreover, as we said, we expect a dark hole at the center of the output beam, independent of the plate's optical retardation, due to the presence of singularity. This approximation does not show this effect. Indeed, the first term shows that we have the same profile of the input beam. However, this simple picture is enough to account for some qualitative effects such as, for instance, the SAM-to-OAM conversion (STOC) [19], the associated optical Berry phase [44] and the changes of the SAM and OAM content of the beam at different depths in the q -plate [49], but it cannot be used to determine the detailed quantitative behavior of the beam during its propagation.

To overcome this broad discrepancy, in this section, we present a general solution based on the series expansion to the light propagation in the q -plate without recursing to the GOA. Moreover, in a special case where beams are in very good paraxial regime an analytical solution can be used to find the light profile inside the q -plate. For such good paraxial beams the SAM and OAM density fluxes also have been calculated for different input LG beams and different polarization states. It has been theoretically shown that for the 1-plate there will not be any torque on the plate due to this conversion, and the 1-plate, when is tuned, gives rise to a complete SAM-to-OAM transfer. Particularly, when the 1-plate is thin enough, the Spin-to-OAM conversion (STOC) efficiency is essentially 100%. By increasing the plate thickness, however, this conversion will decrease. We start from the Maxwell's wave equation inside the q -plate

$$\nabla^2 \mathbf{E} - \nabla(\nabla \cdot \mathbf{E}) + k_0^2 \tilde{\epsilon} \cdot \mathbf{E} = 0 \quad (4.8)$$

where $k_0 = 2\pi/\lambda = \omega/c$ is the wave vector, $\tilde{\epsilon}$ is the relative dielectric tensor at frequency ω , c is the speed of light and λ is the wavelength. In the local frame of the liquid crystal the relative dielectric tensor is given by

$$\tilde{\epsilon}_{local} = n_o^2 \hat{\mathbf{1}} + (n_e^2 - n_o^2) \hat{n} \hat{n} \quad (4.9)$$

where $\hat{\mathbf{1}}$ is the 3×3 identity matrix, \hat{n} is the unite vector in the direction of liquid crystal ordinary axes, and n_o and n_e are the liquid crystal ordinary and extraordinary refractive indices

$$\tilde{\epsilon}_{local} = \begin{pmatrix} n_o^2 & 0 & 0 \\ 0 & n_e^2 & 0 \\ 0 & 0 & n_o^2 \end{pmatrix} \quad (4.10)$$

The laboratory and local frame are related to each other by a rotation of $q\phi$ about the beam propagation axes, assumed z . The relative dielectric tensor in the laboratory, then, is given by

$$\begin{aligned} \tilde{\epsilon}_{lab} &= \hat{R}(q\phi) \cdot \tilde{\epsilon}_{local} \cdot \hat{R}(-q\phi) \\ &= \begin{pmatrix} n^2 - \delta^2 \cos(2q\phi) & \delta^2 \sin(2q\phi) & 0 \\ \delta^2 \sin(2q\phi) & n^2 + \delta^2 \cos(2q\phi) & 0 \\ 0 & 0 & n_o^2 \end{pmatrix} \end{aligned} \quad (4.11)$$

with

$$n^2 := \frac{n_e^2 + n_o^2}{2}, \quad \delta^2 := \frac{n_e^2 - n_o^2}{2} \quad (4.12)$$

where $\hat{R}(\alpha)$ is the rotation matrix about the z -axes. Our liquid crystal is a positive ($n_e > n_o$) and low birefringent material ($n_e - n_o \ll n_o$), the ordinary and extraordinary refractive indices are 1.5 and 1.7, respectively. In a good approximation we may neglect absorption by the liquid crystal molecule. In most materials, including liquid crystals, where the birefringence is small the longitudinal part of the optical field can be neglected with respect to the other terms, i.e. $\nabla \cdot \mathbf{E} \simeq 0$. This term can be neglected with respect to other terms which are present in the laplacian for a region enough far from the center of singularity. Indeed, it is proportional to the E_x and E_y and their first derivatives with a small coefficient equal to $(n_e^2 - n_o^2)/2$. In this approximation, the wave equation reduces to Helmholtz's vector equation $\nabla^2 \mathbf{E}_\perp + k_0^2 \hat{\epsilon} \cdot \mathbf{E}_\perp = 0$ for the transverse part \mathbf{E}_\perp of the field. Note that no frame work has been chosen for our calculation yet and the transformation from laboratory to the local frame does not require the derivative transformation and it has been just used to find the right dielectric tensor. However, in view of the cylindrical symmetry of the problem, it is

convenient to find the eigenmodes of the Helmholtz's vector equation in the circular polarization basis $E_{\pm} = (E_x \pm iE_y)/\sqrt{2}$ and in the cylindrical coordinates (r, ϕ, z) , by setting $\mathbf{E}_{\perp}(r, \phi, z) = (\mathcal{E}_+(r)e^{i(m+q)\phi}, \mathcal{E}_-(r)e^{i(m-q)\phi}, 0)e^{-ik_0\gamma z + i\omega t}$, where γ is the longitudinal spatial frequency and $z = 0$ is the input-face of the q -plate. Inserting this field into Helmholtz's equation, yields a pair of coupled radial equations

$$\begin{aligned} \left(\frac{1}{r} \frac{d}{dr} \left(r \frac{d}{dr} \right) - \frac{(m^2 + q^2)}{r^2} + k_0^2(n_o^2 - \gamma^2) \right) f(r) &= \frac{2mq}{r^2} g(r) \\ \left(\frac{1}{r} \frac{d}{dr} \left(r \frac{d}{dr} \right) - \frac{(m^2 + q^2)}{r^2} + k_0^2(n_e^2 - \gamma^2) \right) g(r) &= \frac{2mq}{r^2} f(r) \end{aligned} \quad (4.13)$$

where $f(r) = (\mathcal{E}_+ + \mathcal{E}_-)/\sqrt{2}$, $g(r) = (\mathcal{E}_+ - \mathcal{E}_-)/\sqrt{2}$. These pair of differential equations are strongly coupled. Equations (4.13) are exact and can be solved by the Frobenius series. Let us discuss some properties of these couple of ordinary differential equations. At the first sight, it is obvious that by changing $n_o \rightarrow n_e$ this equations reversed. So, $f_{n_e, n_o}(r) = g_{n_o, n_e}(r)$. Furthermore, we can cast these differential equations similar to the Schrödinger equation

$$\left\{ \left(\hat{\mathbf{P}}^2 - \frac{m^2 + q^2}{r^2} \right) \hat{\mathbf{1}} - k_0^2 \delta^2 \hat{\sigma}_z - \frac{2mq}{r^2} \hat{\sigma}_x \right\} \psi_{m, \beta}(r) = k^2 \beta^2 \psi_{m, \beta}(r) \quad (4.14)$$

where $\beta^2 = n^2 - \gamma^2$ is the transverse spatial frequency and $\hat{\mathbf{P}}^2 := \frac{1}{r} \frac{d}{dr} \left(r \frac{d}{dr} \right)$ is the radial part of laplacian operator in polar coordinate. The radial part of laplacian operator, $\hat{\mathbf{P}}^2$, is Hermitian with respect to the radial measure $r dr$. It is obvious that the pauli matrices also are Hermitian. Therefore, this hamiltonian is Hermitian with respect to radial measure. So, the eigenvalues, β^2 , are real and its eigenvectors, i.e. $\psi_{m, \beta}(r) := \begin{pmatrix} f^{m, \beta}(r) \\ g^{m, \beta}(r) \end{pmatrix}$, are orthogonal. In other word, we expect the following orthogonality relation

$$\int r dr \left\{ \begin{pmatrix} f^{m, \beta}(r) & g^{m, \beta}(r) \end{pmatrix} \cdot \begin{pmatrix} f^{m, \beta'}(r) \\ g^{m, \beta'}(r) \end{pmatrix} \right\} = \frac{1}{\beta} \delta(\beta - \beta') \quad (4.15)$$

It is impossible to diagonalize $\hat{\mathbf{1}}$, $\hat{\sigma}_x$ and $\hat{\sigma}_z$ at the same time. So, no analytical solution can be found by digitalization technique. However, we have applied the Frobenius series method to find the mode solutions. A possible solution of Eqs. (4.13) is

$$\begin{pmatrix} f^{m, \beta}(r) \\ g^{m, \beta}(r) \end{pmatrix} = r^s \sum_{j=0}^{+\infty} r^j \mathbf{C}_j \quad (4.16)$$

where s , $\mathbf{C}_j = \begin{pmatrix} F_j \\ G_j \end{pmatrix}$ are constant parameters. Substituting this ansatz into Eqs. (4.13) we will have the following recursion equations

$$\mathbf{M}_j \cdot \mathbf{C}_j + k_0^2 \mathbf{N} \cdot \mathbf{C}_{j-2} = 0 \quad (4.17)$$

with

$$\mathbf{M}_j = \begin{pmatrix} (j+s)^2 - (m^2 + q^2) & -2mq \\ -2mq & (j+s)^2 - (m^2 + q^2) \end{pmatrix}, \quad \mathbf{N} = \begin{pmatrix} \beta^2 - \delta^2 & 0 \\ 0 & \beta^2 + \delta^2 \end{pmatrix} \quad (4.18)$$

The proper value of s can be found from the recursion relation for $n = 0$. The right value of s is, then, equal to $|m| + |q|$. By replacing s into the first term of the recursion relation we will get two conditions based on the sign of $|mq|$ for the F and G constant. For positive and negative values of mq the F_0 and G_0 must be vanish, respectively. However, for simplicity of our calculation, without losing the generality, we consider a positive topological charge $q > 0$. It can be shown easily that all odd terms of C 's coefficient in the series must be vanished due to having non zero determinate for \mathbf{M}_j . So, the radial functions of modes can be expressed in terms of the these recursion relations

$$\begin{pmatrix} f^{m,\beta}(r) \\ g^{m,\beta}(r) \end{pmatrix} = (k_0 r)^s \sum_{j=0}^{\infty} (k_0 r)^{2j} \{\mathbf{P}_j \cdot \mathbf{P}_{j-1} \dots \mathbf{P}_1\} \cdot \begin{pmatrix} 1 \\ 0 \end{pmatrix} \quad \text{for } m \geq 0 \quad (4.19)$$

$$\begin{pmatrix} f^{m,\beta}(r) \\ g^{m,\beta}(r) \end{pmatrix} = (k_0 r)^s \sum_{j=0}^{\infty} (k_0 r)^{2j} \{\mathbf{P}_j \cdot \mathbf{P}_{j-1} \dots \mathbf{P}_1\} \cdot \begin{pmatrix} 0 \\ 1 \end{pmatrix} \quad \text{for } m \leq 0 \quad (4.20)$$

where $\mathbf{P}_j = -\mathbf{M}_{2j}^{-1} \cdot \mathbf{N}$ and $s = |m| + q$. The radial functions are real and they are vanishing at the origin, due to presence of r^s . The final form of the mode inside the q -plate, then, is given

$$\begin{pmatrix} E_+(r, \phi, z) \\ E_-(r, \phi, z) \end{pmatrix} = \frac{1}{\sqrt{2}} \int \beta d\beta \left\{ \sum_{j=0}^{\infty} F_0^{m,\beta} \begin{pmatrix} e^{i(m+q)\phi} (f^{m,\beta}(r) + g^{m,\beta}(r)) \\ e^{i(m-q)\phi} (f^{m,\beta}(r) - g^{m,\beta}(r)) \end{pmatrix} + \sum_{j=0}^{-\infty} G_0^{m,\beta} \begin{pmatrix} e^{i(m+q)\phi} (f^{m,\beta}(r) + g^{m,\beta}(r)) \\ e^{i(m-q)\phi} (f^{m,\beta}(r) - g^{m,\beta}(r)) \end{pmatrix} \right\} e^{-ik_0 \sqrt{n^2 - \beta^2} z} \quad (4.21)$$

By using the orthogonality relation between radial functions, then, the light propagation kernel inside the q -plate can be calculated

$$\begin{pmatrix} E_+(r, \phi, z) \\ E_-(r, \phi, z) \end{pmatrix} = \frac{1}{\sqrt{2\pi}} \int r' dr' \int d\phi' \mathbf{K}[r, \phi; r', \phi'; z] \cdot \begin{pmatrix} E_+(r', \phi', 0) \\ E_-(r', \phi', 0) \end{pmatrix} \quad (4.22)$$

with

$$\begin{aligned} \mathbf{K}[r, \phi; r', \phi'; z] &= \int \beta d\beta \sum_{m=-\infty}^{+\infty} \left\{ \begin{pmatrix} A^{m,\beta} e^{i(m+q)(\phi-\phi')} & e^{2iq\phi} B^{m,\beta} e^{i(m-q)(\phi-\phi')} \\ e^{-2iq\phi} B^{m,\beta} e^{i(m+q)(\phi-\phi')} & C^{m,\beta} e^{i(m-q)(\phi-\phi')} \end{pmatrix} \right. \\ &\times \left. e^{-ik_0\sqrt{n^2-\beta^2}z} \right\} \end{aligned} \quad (4.23)$$

where

$$\begin{aligned} A^{m,\beta} &= (f^{m,\beta}(r') + g^{m,\beta}(r'))(f^{m,\beta}(r) + g^{m,\beta}(r))/2, \\ B^{m,\beta} &= (f^{m,\beta}(r') - g^{m,\beta}(r'))(f^{m,\beta}(r) + g^{m,\beta}(r))/2, \\ C^{m,\beta} &= (f^{m,\beta}(r') - g^{m,\beta}(r'))(f^{m,\beta}(r) - g^{m,\beta}(r))/2. \end{aligned}$$

Of course, the final output beam can be calculated analytically, if the $f^{m,\beta}(r)$, $g^{m,\beta}(r)$ functions can be found in terms of the well-known special functions. However, the main characteristic of output beam can be understood only by taking part of the radial modes property. In many practical applications we are working out with a very good paraxial beams. There is a regime in which the Eq. (4.13) can be solved in terms of the well-known special function, i.e. the irrational Bessel functions. Here we consider only the approximate solutions for paraxial beams at normal incidence. Setting $\gamma = \gamma_o = \sqrt{n_o^2 - \beta^2} \simeq n_o - \beta^2/2n_o$, where β is a transverse spatial spectrum, Eqs.(4.13) reduce to the equations for the ordinary wave

$$\begin{aligned} f_o''(r) + \frac{f_o'(r)}{r} + \left(k_0^2 \beta^2 - \frac{\mu^2}{r^2} \right) f_o(r) &= \frac{\nu g_o(r)}{r^2} \\ g_o''(r) + \frac{g_o'(r)}{r} + \left(k_0^2 \beta^2 \Lambda^2 - \frac{\mu^2}{r^2} \right) g_o(r) &= \frac{\nu f_o(r)}{r^2} \end{aligned} \quad (4.24)$$

where $\Lambda^2 = 1 + 2(n_e^2 - n_o^2)/\beta^2$. We observe that in commercial liquid crystals we have $n_e^2 - n_o^2 \simeq 0.5$ while usual paraxial laser beams at normal incidence have the radial spatial frequency with β ranging from zero to $\beta \simeq 10^{-2}$. The parameter Λ^2 is therefore very large in all practical cases. We may then solve Eqs.(4.24) as asymptotic series of Λ^2 . The Λ^2 can be used as an expansion parameter. So, we may expand $f_o(r)$ and $g_o(r)$ in terms of Λ^2

$$\begin{aligned} f_o(r) &= u_o^0(r) + \sum_{j=1}^{+\infty} u_o^j(r) \\ g_o(r) &= v_o^0(r) + \sum_{j=1}^{+\infty} v_o^j(r) \end{aligned} \quad (4.25)$$

where $u_o^j(r)$ and $v_o^j(r)$ denote the perturbation order functions for ordinary wave. We will show that they are function of Λ^{-j} . Replacing Eqs. (4.25) into equations (4.13),

yields the following differential recursion equations for ordinary modes

$$\begin{aligned} u_o^{j''}(r) + \frac{1}{r^2} u_o^{j'}(r) + \left(k_0^2 \beta^2 - \frac{m^2 + q^2}{r^2} \right) u_o^j(r) &= \frac{2mq}{r^2} v_o^j \\ v_o^{j''}(r) + \frac{1}{r^2} v_o^{j'}(r) + (k_0 \beta \Lambda)^2 v_o^j(r) &= \left(\frac{m^2 + q^2}{r^2} v_o^{j-1}(r) + \frac{2mq}{r^2} v_o^{j-1}(r) \right) \end{aligned} \quad (4.26)$$

The zeros order for $v_o(r)$ is

$$v_o^{0''}(r) + \frac{1}{r^2} v_o^{0'}(r) + (k_0 \beta \Lambda)^2 v_o^0(r) = 0 \quad (4.27)$$

Its solution is then

$$v_o^0 = D_1 J_0(k_0 \beta \Lambda r) + D_2 Y_0(k_0 \beta \Lambda r) \quad (4.28)$$

where D_1, D_2 are arbitrary constants, $J_0(x)$ and $Y_0(x)$ are the Bessel functions of index zero [42]. The argument of bessel function is large, remember that $k_0 \beta \Lambda$ is a large parameter. So, they are highly oscillating when r changes. The asymptotic behavior of bessel function for large argument is look like *sine* and *cosine* functions. By choosing a good boundary condition we may take it zero. Replacing, it in the zeros order of the $u_o(r)$ in the recursion equations, yields

$$u_o^{0''}(r) + \frac{1}{r^2} u_o^{0'}(r) + \left(k_0^2 \beta^2 - \frac{m^2 + q^2}{r^2} \right) u_o^0(r) = 0 \quad (4.29)$$

Its solution, then, is

$$u_o^0 = E_o J_\mu(k_0 \beta r) \quad (4.30)$$

where E_o is an arbitrary constant and $J_\mu(x)$ is the bessel function of order $\mu = \sqrt{m^2 + q^2}$. We can show that other terms of expansion are two small with respect to $v_o^0(r)$ and $u_o^0(r)$ and they are bonded. In order to show this, it is much convenient to work out with integral form of the recursion relations of Eq. (4.26)

$$\begin{aligned} u_o^j(r) &= m\pi \int_{r_0}^r (J_\mu(k_0 \beta \zeta) Y_\mu(k_0 \beta \Lambda r) - Y_\mu(k_0 \beta \zeta) J_\mu(k_0 \beta \Lambda r)) \frac{v_o^j(\zeta)}{\zeta} d\zeta \\ v_o^j &= \frac{\pi}{2} \int_{r_0}^r (J_0(k_0 \beta \zeta) Y_0(k_0 \beta \Lambda r) - Y_0(k_0 \beta \zeta) J_0(k_0 \beta \Lambda r)) \frac{\mu^2 v_o^{j-1}(\zeta) + 2mq u_o^{j-1}(\zeta)}{\zeta} d\zeta \end{aligned} \quad (4.31)$$

where $\mu = \sqrt{m^2 + q^2}$. These two integral relations show that both $u_o^j(r), v_o^j(r)$ functions for $j > 0$ are bounded

$$|u_o^j(r)| \leq \left(\frac{1}{k_0 \beta \Lambda} \right)^n (\mathcal{O})_1(r, r_0, m, N)$$

$$|v_o^j(r)| \leq \left(\frac{1}{k_0 \beta \Lambda} \right)^n (\mathcal{O})_2(r, r_0, m, N) \quad (4.32)$$

where N is the upper bound of the Bessel function of second type. This approximation is not valid for the whole transverse plane of the plate. It is obvious, from the zeroth order of $v_o^0(r)$, that this high oscillation method is just valid for the whole transverse plane except a small region close to plate singularity where argument can be compared to unity, i.e. $\pi/2k_0\beta\Lambda r_0 \sim 1$. This small region has a radius about $r_0 \approx \lambda/(\Lambda\beta) = \lambda/\sqrt{n_e^2 - n_o^2}$. For commercial liquid crystal we have $r_0 \approx 1.25\lambda$. In this small region the singularity is located and the optical axis is not well defined there. The effect of this region can be accounted for only by the exact (not paraxial) wave approach, but we may anticipate on physical grounds that the main effect of this region is to scatter a small fraction of the light at large angles out of the paraxial beam. In conclusion, only the zero-order approximation, $f_o(r) = E_o J_\mu(k_0 \beta r)$ and $g_o(r) = 0$, of the asymptotic solution of Eq.(4.24) for the ordinary wave is important and other order of approximation asymptotically vanishes for large Λ . The differential equation for the extraordinary wave is obtained from Eqs.(4.13) by setting $\gamma = \gamma_e = \sqrt{n_e^2 - \beta^2} \simeq n_e - \beta^2/2n_e$ and it can be obtained from Eqs.(4.24) by the formal replacements $f \rightarrow g, g \rightarrow f, \Lambda^2 \rightarrow -\Lambda^2$. In the same way the zero-order asymptotic solution for the extraordinary wave is then given by $f_e(r) = 0$ and $g_e(r) = A_e J_\mu(k_0 \beta r)$ with constant A_e . All other terms of the asymptotic solution can be found recursively and are vanished for large Λ . From the asymptotic paraxial modes of Helmholtz' equation it is straightforward to calculate the Fresnel paraxial propagator for the optical field \mathbf{E}_\perp . The optical field at plane z in the q -plate is given by

$$\begin{aligned} \mathbf{E}_\perp(r, \phi, z) &= \frac{1}{2} \int_0^\infty \rho d\rho \int_0^{2\pi} d\psi \hat{R}(q\phi) \left\{ (K^o + K^e) \hat{1} \right. \\ &\quad \left. + (K^o - K^e) \hat{\sigma}_z \right\} \hat{R}(-q\psi) \mathbf{E}_\perp(\rho, \psi, 0). \end{aligned} \quad (4.33)$$

where $\hat{1}$, $\hat{R}(\phi)$ and $\hat{\sigma}_z$ are the 2×2 unit, rotation and Pauli's matrices, respectively. The Fresnel kernels in Eq.(4.33) are given by $K^{o,e} = \sum_m K_{\mu(m)}^{o,e}(r, \rho; z) e^{im(\phi-\psi)}$, where $\mu(m) = \sqrt{m^2 + q^2}$ and

$$\begin{aligned} K_{\mu(m)}^{o,e}(r, \rho; z) &= \left(\frac{in_{o,e}k_0}{2\pi z} \right) i^{\mu(m)} J_{\mu(m)} \left(\frac{k_0 n_{o,e} r \rho}{z} \right) \\ &\quad \times e^{-\frac{ik_0 n_{o,e} (r^2 + \rho^2)}{2z} - ik_0 n_{o,e} z} \end{aligned} \quad (4.34)$$

The Fresnel kernels K^o and K^e in Eq.(4.34) are characterized by the presence of Bessel function of irrational order. Although, K^o and K^e cannot be obtained in a closed form, they permit to evaluate analytically the field transmitted by the q -plate in important cases as, for instance, for Laguerre-Gaussian (2.5.2.1) incident beams. Here we

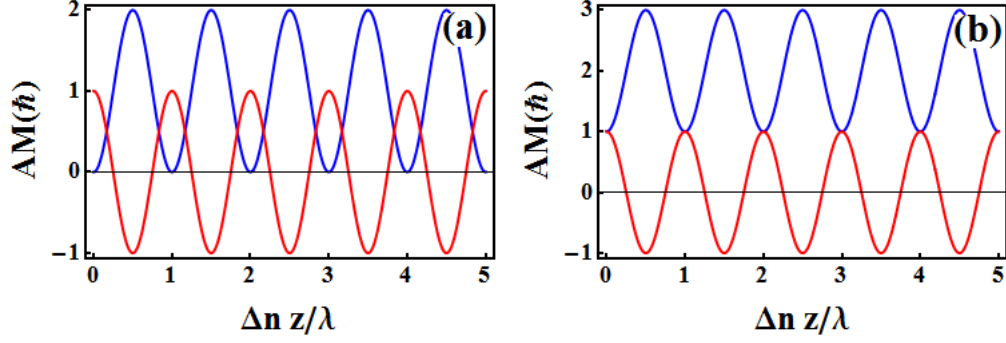


FIGURE 4.5: Beating of SAM (blue line) and OAM (red line) as a function of the optical retardation $\Delta n z/\lambda$ while a circularly polarized input beam propagates in the 1-plate. (a) For LG_{00} and (b) LG_{01} as a input beam. We used the following data: $n_o = 1.5$, $n_e = 1.7$, $w_0 = 50\lambda$.

consider only the case of a LG_{0l} beam impinging onto the QP. Setting $\mathbf{E}_\perp(\rho, \phi, 0) = e^{il\phi} \text{LG}_0^l(\rho) \begin{pmatrix} a \\ b \end{pmatrix}$ in the circular polarization basis, where $\text{LG}_0^l(\rho)$ is the radial amplitude of Laguerre-Gaussian modes, we obtain

$$\begin{pmatrix} E_+ \\ E_- \end{pmatrix} = e^{i(l\phi - k_0 n_o z)} \begin{pmatrix} K_{\mu^-}^+ & K_{\mu^+}^- e^{2iq\phi} \\ K_{\mu^-}^- e^{-2iq\phi} & K_{\mu^+}^+ \end{pmatrix} \begin{pmatrix} a \\ b \end{pmatrix} \quad (4.35)$$

where $K_\mu^\pm = (\text{HyGG}_{|l|-\mu, \mu}(r, z/n_o) \pm e^{-ik_0 \Delta n z} \text{HyGG}_{|l|-\mu, \mu}(r, z/n_e))/2$, $\Delta n = n_e - n_o$, $\mu^\pm = \mu(l \pm q)$ and $\text{HyGG}_{p,m}(r, z)$ is the Hypergeometric-Gaussian mode (2.5.2.2) [13], viz.

$$\text{HyGG}_{pm}(\rho, \zeta) = C_{pm} \zeta^{\frac{p}{2}} (\zeta + i)^{-(1+|m|+\frac{p}{2})} \rho^{|m|} \times e^{-\frac{i\rho^2}{\zeta+i}} {}_1F_1\left(-\frac{p}{2}, 1+|m|; \frac{\rho^2}{\zeta(\zeta+i)}\right)$$

where $C_{pm} = i^{|m|+1} \sqrt{\frac{2^{p+|m|+1}}{\pi} \frac{\Gamma(1+|m|+\frac{p}{2})}{\Gamma(p+|m|+1) \Gamma(|m|+1)}}$, $\rho = r/w_0$, $\zeta = z/z_R$ and $z_R = k_0 w_0^2/2$ is the beam Rayleigh range. Because $n_o \simeq n_e$, the arguments of the function HyGG_{pm} in Eq.(4.35) are very close, so that when $\Delta n z = j\lambda$ ($j = 1, 2, \dots$) the matrix in Eq. (4.35) is almost diagonal, the beam in the q -plate has the same value of OAM, i.e. $l\hbar$ per photon. When $\Delta n z = (2j-1)\lambda/2$, instead, only the off-diagonal elements survive, the right and left circular components of transmitted field assume a phase factor $e^{\pm 2iq\phi}$ and the beam OAM change by $\pm 2q\hbar$ per photon, depending on the input circular polarization helicity.

As the beam propagates in the q -plate, its transverse profile, spin and OAM change. From Eq. (4.35), we may calculate the average SAM and OAM carried by the beam at the plane z in the q -plate, obtaining

$$S_z(z) = \frac{1}{\omega} \Re[e^{-ik_0 \Delta n z} (|b|^2 I_{|l|-\mu^+, \mu^+}(z) - |a|^2 I_{|l|-\mu^-, \mu^-}(z))] \quad (4.36)$$

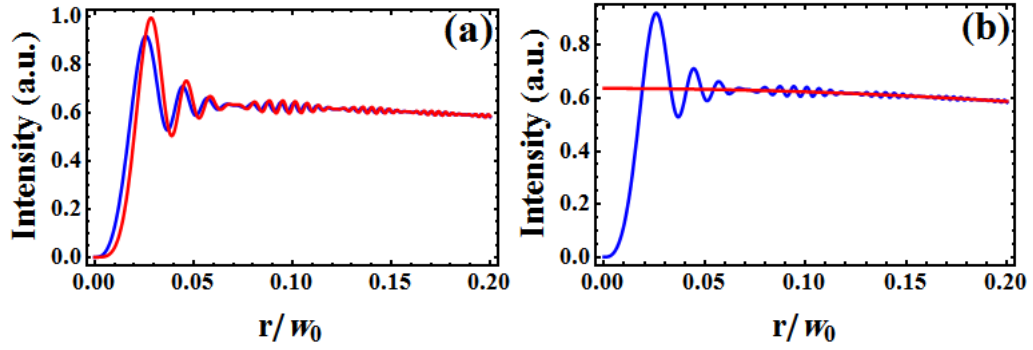


FIGURE 4.6: Intensity profile for (a) full STOC (b) no STOC in the 1-plate. Red and blue lines are simulated by [49] and our theory [48], respectively. The input beam assumed the TEM₀₀.

$$L_z(z) + \frac{q}{\omega} S_z(z) = \frac{1}{\omega} ((\ell - q) |a|^2 + (\ell + q) |b|^2) \quad (4.37)$$

where

$$I_{p,m}(\zeta) = \frac{2^{p+|m|+1} \Gamma^2\left(\frac{p}{2} + |m| + 1\right)}{\Gamma(|m| + 1) \Gamma(p + |m| + 1)} \chi^{-p/2}(\zeta) \\ \times \left(\frac{n_o n_e}{2n_o n_e - i(n_e - n_o)\zeta} \right)^{p+|m|+1} {}_2F_1\left(-\frac{p}{2}, -\frac{p}{2}; |m| + 1; \chi(\zeta)\right) \quad (4.38)$$

and $\chi(\zeta) = \left(\frac{n_e n_o}{n_e n_o - i(n_e - n_o)\zeta} \right)^2$. As expected, we have $I_{p,m}(0) = 1$ so that Eqs. (4.37) and (4.36) yield $S_z(0) = (|b|^2 - |a|^2)/\omega$ and $L_z(0) = (|a|^2 + |b|^2)\ell/\omega$. In Fig. (4.5) the photon STOC [19] is shown as a function of the propagation depth in the 1-plate for LG₀₀ and LG₀₁ input beams. The conversion efficiency is practically 100% and its maximum occurs at optical retardation $\Delta n z = (2j - 1)\lambda/2$ with integer j . When the optical retardation is $j\lambda$, no conversion occurs and the beam has no OAM. Changing the optical retardation of the 1-plate provides a good way to control the STOC process. However, when the thickness of the 1-plate becomes very large (much larger than the beam Rayleigh range) the conversion efficiency slowly decays. According to Eqs. (4.35) and (4.36), the field profile inside the 1-plate (and at its exit face) vanishes as $r^{\sqrt{2}}$ along the beam axis so that the intensity profile has the characteristic doughnut shape irrespective of the OAM carried by the beam. Figure (4.7) shows the intensity profiles for (a) full STOC (b) no STOC. For the sake of comparison, the results obtained in the GOA [49] are also shown. We can deduce that the GOA approximation is fairly good for the case of full STOC, but is very bad in the near field and in the case of no STOC. Dramatic changes of the intensity profile depending on the final OAM are seen, however, in the far-field after free-air propagation. When the STOC is maximum, in fact, we observe the doughnut profile, while when no conversion occurs, the far-field pattern has again a maximum at its center. This is shown in Fig. (4.7).

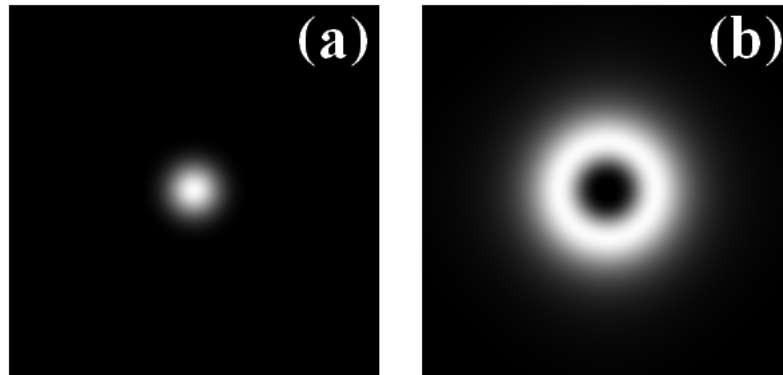


FIGURE 4.7: Intensity profile in the far-field beyond the 1-plate after free-air propagation. (a) No STOC; (b) Full STOC.

In order to verify our theory we have built up a setup to measure the converted and non-converted part of beam. The experimental setup was similar to the setup which we have used to measure the q -plate efficiency (see Fig. 3.12). Instead, a CCD camera replaced with a power meter in order to record the beam intensity profile of STOC and non-STOC parts. The intensity pattern for STOC and non-STOC parts has been recorded for different distances from the q -plate (4.8). The intensity profiles for both STOC and non-STOC part are quite similar at the near field, 4cm far from the q -plate, as our theory predicted. By free-air propagation, then, two beams have different behaviors: the STOC part changed to a doughnut-like beam and the non-STOC part, instead, changed in such away that it recovered the TEM₀₀-like profile.

4.4 OAM Poincarè sphere and geometrical phase (Karimi et al. [53])

In many practical cases, the OAM space is however restricted to the o_ℓ subspace spanned by a pair of opposite OAM eigenvalues $\pm\ell$. This bidimensional optical subspace is then isomorphic to the standard polarization space, that is the space of the spin angular momentum of light. A standard geometric representation of any polarization (or SAM) state of light is provided by the well known Poincaré sphere [50]. In particular, the spin $s = \pm 1$ eigenvalues are usually mapped onto the poles of Poincaré sphere and correspond to left- and right-handed circular polarizations, while their equal-weight linear combinations are mapped along the equator circle and correspond to differently oriented linear polarizations. The other points on the sphere describe arbitrary elliptical polarizations. Analogously, any state in a given o_ℓ subspace can be represented as a point on a OAM Poincaré sphere [51]. The OAM eigenvalues $\pm\ell$ may again be mapped onto the

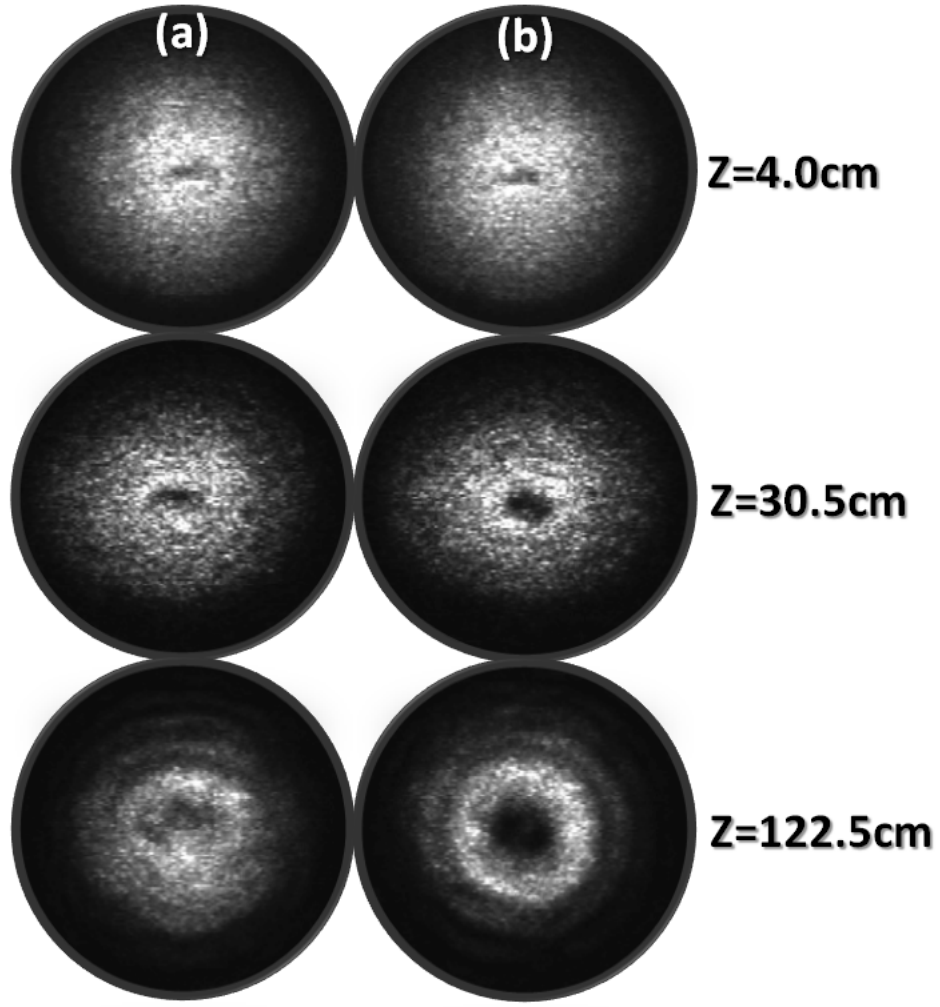


FIGURE 4.8: The intensity profile of outgoing beams from the q -plate in a different plane. (a) non-STOC (b) STOC part. The beam waist and beam wavelength were 1.5 mm and 532 nm, respectively.

poles of this sphere and correspond to generalized Laguerre-Gaussian(LG_ℓ) transverse modes, while equal-weight linear combinations are mapped along the equator circle and correspond to differently oriented generalized Hermite-Gaussian (HG_ℓ) modes (By generalized LG_ℓ or HG_ℓ modes we mean ℓ -eigenstates of light OAM resulting from linear combination of $LG_{p,m}$ modes with different radial number p and fixed azimuthal number ℓ). By this geometrical representation, a one-to-one correspondence is established between the states of SAM and those of o_ℓ , for any ℓ . In the following, we label the axis joining the right (R) and left (L) circular polarizations states on the Poincaré sphere as the z -axis, and the axis joining the vertical (V) and horizontal (H) polarization states as the x -axis. The photon SAM can be manipulated easily by polarizers and birefringent plates. It is well known that sequences of quarter-wave plates (QW) and half-wave plates (HW) oriented at suitable angles can change any given polarization state into another

state at will [52, 53]. Moreover, electro-optical devices can be used to make such light

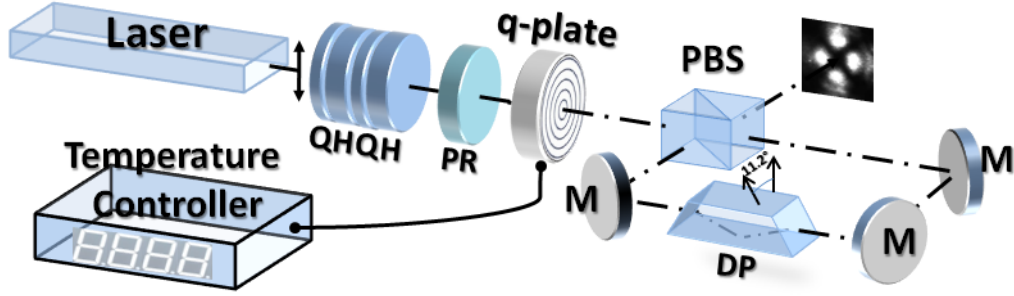


FIGURE 4.9: Experimental setup for generating polarization-controlled linear combinations of LG_2 beams. Legend: HQHQ - set of waveplates to control the beam polarization; PR - polarization rotator; PBS - polarizing beam-splitter; DP - Dove prism; M - mirror.

polarization manipulation very fast. No so simple and fast devices are available for manipulating the light OAM. Cylindrical lens converters and Dove prisms can simulate the behavior of HW and QW wave plates in the o_ℓ space [24], but these devices are difficult to be aligned and cannot change the light OAM very quickly. Following continuous paths on the OAM Poincaré sphere by means of these devices would require very careful control and precise mechanics. Recently, a new device, the q -plate was introduced which is able to transfer the SAM state of the beam to the o_2 subspace [19, 44]. In a previous chapter, we showed that it is possible to achieve efficiencies exceeding 90% by controlling the QP temperature [48]. A very appealing use of the STOC process is that of exploiting the easy and fast control that we have on the light polarization degree of freedom for controlling the OAM degree of freedom. By using STOC, cylindrical lens mode converters and Dove prisms can be conveniently replaced with birefringent plates and electro-optical cells. The aim of this work is to demonstrate the easy and efficient control on the OAM of a light beam that is attainable via the STOC process. Arbitrary and continuously controllable linear combinations of LG_2 modes have been generated in a very simple way and with efficiency exceeding 90% by manipulating the input beam polarization. Our experimental setup is shown in Fig. (4.9) [54]. The polarization of the light beam entering the QP is controlled by the QHQH waveplate sequence $QW(90^\circ)HW(-\alpha/4)QW(0^\circ)HW(90^\circ+\beta/4)$, where in parentheses are the orientation angles of each plate counted from the horizontal plane. As it can be easily shown, this sequence of waveplates applies to the input polarization state first a rotation of angle α around the y -axis of the SAM Poincaré sphere and then a rotation of an angle β around the z -axis. After this QHQH set, we inserted the QP, a polarization rotator (PR) of 45° and a Sagnac Polarizing Interferometer (SPI). In the SPI, a Dove prism rotated by 11.25° from the horizontal plane was inserted. The QP, PR, and SPI

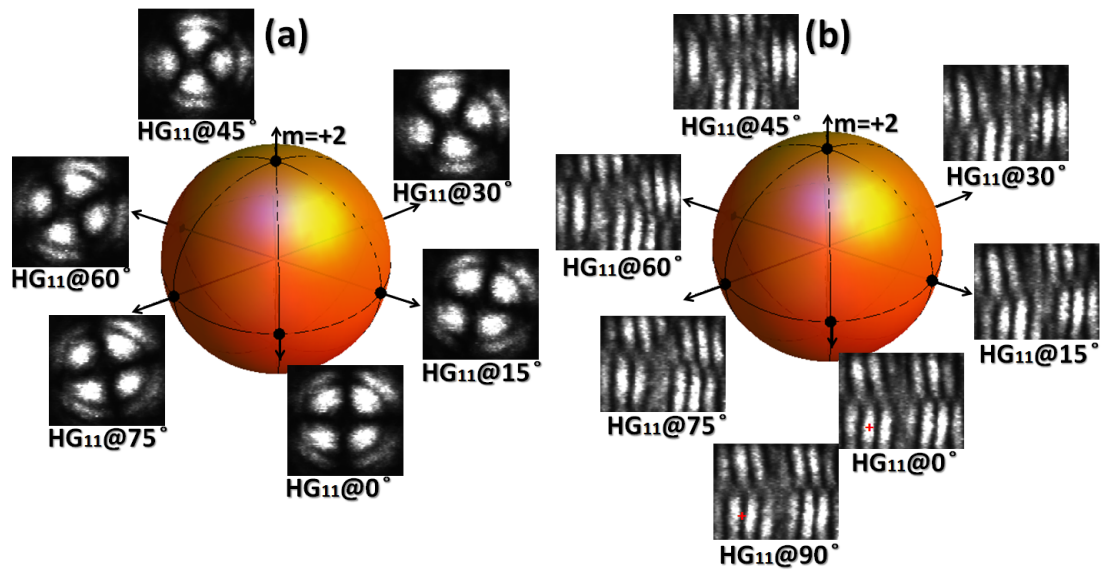


FIGURE 4.10: Trajectory along the equator of the Poincaré's sphere. (a) Intensity profiles of generated beams corresponding to differently rotated HG_2 modes. (b) Corresponding interference patterns with a TEM_{00} A-polarized reference beam.

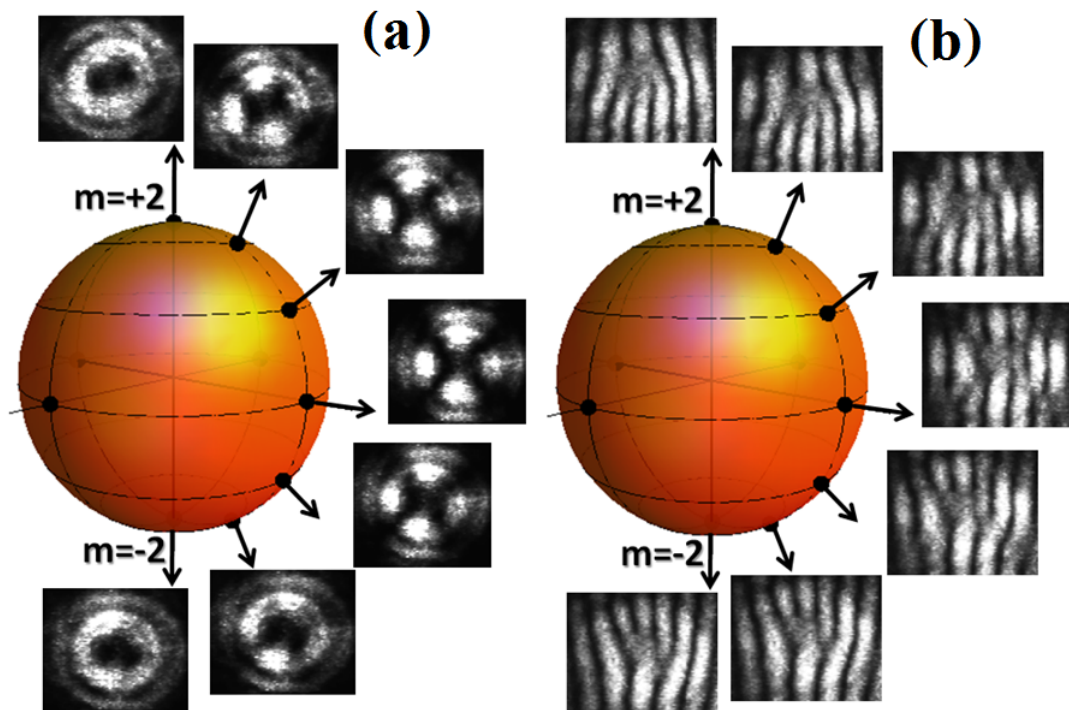


FIGURE 4.11: Trajectory along a meridian of the Poincaré's sphere. (a) Intensity profiles of generated beams corresponding to different linear combinations of $\text{LG}_{\pm 2}$ modes. (b) Corresponding interference patterns with a TEM_{00} A-polarized reference beam.

are the heart of our apparatus, because they realize the required mapping ¹.

$$(\alpha|L\rangle + \beta|R\rangle)|0\rangle \rightarrow (\alpha|2\rangle + \beta|-2\rangle)|A\rangle. \quad (4.39)$$

where $|L\rangle, |R\rangle, |H\rangle, |V\rangle, |D\rangle, |A\rangle$ denote the right-circular, left-circular, horizontal, vertical, diagonal, and anti-diagonal polarization states, respectively, and $|\ell\rangle$, with integer ℓ , denote the OAM eigenstate with eigenvalue ℓ . It is worth noting that our apparatus works in any basis. For example, it also realizes the mapping $(\alpha|H\rangle + \beta|V\rangle)|0\rangle \rightarrow (\alpha|h\rangle + \beta|v\rangle)|A\rangle$, where $|h\rangle$ and $|v\rangle$ denote the HG₂ modes corresponding to the linear polarization states H and V . The detailed functioning of our apparatus is as follows. Up to a global phase factor, the action of a tuned QP on the elliptically polarized TEM₀₀ ($\ell = 0$) input beam is given by

$$\begin{aligned} (\alpha|L\rangle + \beta|R\rangle)|0\rangle &\xrightarrow{\widehat{\text{QP}}} \alpha|R, 2\rangle + \beta|L, -2\rangle = \\ &= \frac{1}{\sqrt{2}}[|H\rangle(\alpha|2\rangle + \beta|-2\rangle) - i|V\rangle(\alpha|2\rangle - \beta|-2\rangle)] \end{aligned} \quad (4.40)$$

The radial modes are factorized out and can be omitted. From Eq. (4.40) we see that insertion of a linear polarizer after the QP would already select the desired linear combination of LG₂ and LG₋₂ modes (or $|2\rangle$ and $|-2\rangle$ states), but this would also reduce the maximum conversion efficiency to 50% [33]. The polarizing Sagnac interferometer scheme shown in Fig. (4.9) allows one to increase the theoretical efficiency to 100%. The Sagnac interferometer is made of the Polarizing Beam Splitter (PBS) and the three mirrors (M). The H- and V-polarized components of the beam emerging from the q -plate are initially separated by the PBS and travel through the interferometer in opposite directions until they are recombined on exit by the same PBS. Equal optical paths of the counter-propagating beams render this interferometer particularly noise-insensitive, thus removing the need for active control of the interferometer length [55]. The reflection in the Dove prism tilted at angle θ adds a phase factor $e^{2i\ell\theta}$ to the OAM eigenstate $|\ell\rangle$ and changes $|\ell\rangle$ into $|-\ell\rangle$. Moreover, the polarization state $|H\rangle$ is left unchanged, while $|V\rangle$ is changed into $-|V\rangle$. In our case, however, because of the counter-propagation, the H-polarized beam sees the Dove prism tilted at angle θ and the V-polarized beam sees the Dove prism tilted at angle $-\theta$. With the substitutions $|H, \ell\rangle \rightarrow e^{2i\theta}|H, -\ell\rangle$, $|V, \ell\rangle \rightarrow -e^{-2i\theta}|V, -\ell\rangle$, and then setting $\theta = \pi/16$, we see that, up to a phase factor, the state in Eq. (4.40) is changed into

$$(2) \rightarrow \psi_{out} = |D\rangle(\alpha|-2\rangle - i\beta|2\rangle), \quad (4.41)$$

¹Our apparatus produces constant A -linear polarization in the exit beam.

We see that the resulting beam is fully polarized, and that its OAM content is a linear combination of $LG_{\pm 2}$ modes with coefficients uniquely related to α and β . Thus, we succeeded to realize one-to-one mapping of the input SAM state onto the output OAM state², but not yet the wanted one, given by Eq. (4.39). First, the $\ell = \pm 2$ states in Eq. (4.41) are in the wrong place. This problem can be fixed by adding one more mirror reflection, in order to make the total number of reflections odd (not counting the reflections taking place in the Dove prism). This exchanges the $\ell = \pm 2$ states and also the D-polarization of the output state into the A-polarization. Second, the phase difference of $\pi/2$ between the two terms on the right of Eq. (4.41) must be eliminated. This is accomplished by the PR located before the PSI, which introduces a retardation of $\pi/2$ between the circular polarization components of the input beam.

To show the flexibility of our apparatus in manipulating the light OAM, we performed a set of measurements in which we slowly modulated the polarization of the input TEM_{00} beam so to make the output beam follow a controlled trajectory on the OAM Poincaré sphere. In this way, arbitrary states in the o_2 subspace were easily and continuously generated starting from a TEM_{00} laser beam. The power conversion efficiency from TEM_{00} H-polarization to o_2 modes was found to exceed 90% for all o_2 modes. This efficiency is larger than the maximum typically obtainable ($\simeq 80\%$) with blazed holograms. In our experiments, we measured the OAM content of the output beam in several points on the Poincaré sphere by recording the intensity profile and the pattern obtained by interference with an A-polarized reference beam assimilable to a plane wave (not shown in Fig. 4.9). The results are shown in Figs. (4.10-4.13).

In the measurements we used a 532 nm TEM_{00} H-polarized laser beam and a home made LC q -plate tuned to optimum STOC by temperature. The details of the q -plate and of the tuning system are described elsewhere [48]. In Fig. (4.10) the observed intensity profiles and interferograms are shown when the OAM state is moved along the equator of the Poincaré sphere. The data for the equatorial trajectory shown in Fig. (4.10) were obtained by fixing $\alpha = 0$ and moving β from zero to π by rotating from 90° to 135° the second HW-plate in the HQHQ device. In this way, the continuous sequence of HG_2 modes with different orientations were generated. Similarly, the meridian trajectory on the OAM Poincaré sphere was obtained by fixing $\beta = 0$ and changing α from $-\pi/2$ to $+\pi/2$ in the QHQH device. This was achieved by rotating the first HW-plate from $+22.5^\circ$ to -22.5° . The continuous passage from the doughnut beam and down-fork interferogram corresponding to LG_2 mode to HG mode in crossing the equator to reach finally the doughnut beam and up-fork interferogram corresponding to LG_{-2} mode is shown in Fig. (4.11). In our last experiment, we drove the OAM state along

²The mapping (4.41) may be enough in many applications

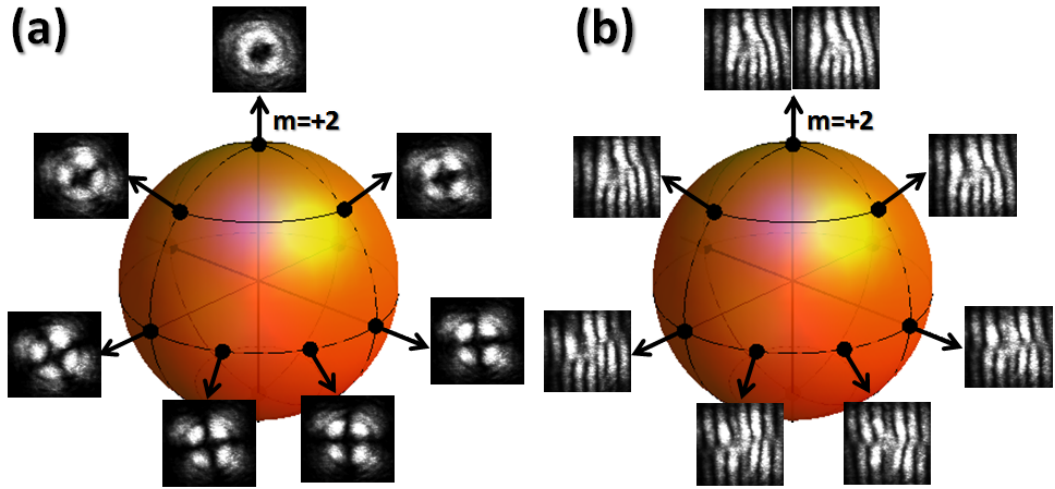


FIGURE 4.12: A possible closed path over the OAM-Poincaré sphere. The path starts and ends at the pole. (a) Intensity profiles of the generated beam at different points of the path. (b) Corresponding interference patterns with a TEM_{00} A-polarized reference beam.

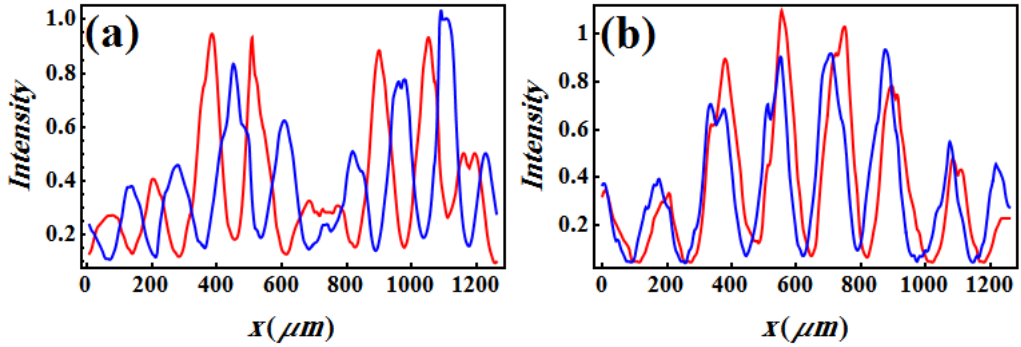


FIGURE 4.13: Interference patterns for two different closed trajectories on the Poincaré sphere. (a) Circular path along the equator, as shown in Fig. (4.10). In this case, there is a π change in the phase when the path is closed. (b) Path shown in Fig. (4.12). In this case there is a $\pi/4$ change in the phase when the path is closed. Blue and red lines show the fringes of the initial and final states, respectively.

a closed path on the Poincaré sphere and measured the resulting Pancharatnam geometric phase [56] by interference with almost plane-wave A-polarized reference beam. The closed path we chose and the corresponding intensity profiles and interferograms are shown in Fig. (4.12). The observed fringe shift due to Pancharatnam geometric phase after a cycle is shown in Fig. (4.13). As expected, in both cases we found a phase shift equal to the solid angle subtended by the path on the OAM Poincaré sphere. The geometrical phase acquired by a light beam when the OAM state was moved along a closed path on its Poincaré sphere was observed some time ago [57]. However, in this experiment the light OAM content was changed discontinuously by making the beam pass through a sequence of fixed Dove prisms and cylindrical lens converters. In the

present work, the beam OAM was changed adiabatically and the phase was monitored continuously along the path. We notice that the Pancharatnam geometric phase is already present when we close the path on the SAM Poincaré sphere of the input beam. What we have done with our experiment is therefore to prove that the STOC process is able to transfer coherently global phase shifts, as geometric phase shifts, from the SAM to the OAM degree of freedom. After the transfer, the polarization is fixed, in our case, to linear anti-diagonal, so that the SAM degree of freedom is still available for further encoding of information. Moreover, having a fixed polarization and geometrical phase transferred to OAM allows to obtain a constant fringe visibility along the whole close path, which is impossible in experiments on Pancharatnam's phase based on polarization only [58].

4.5 Generation of needle beams (Karimi et al. [14])

Richard and Wolf [59] have shown, by using a vector Debye integral, that a non-propagating component of the electric field can be created near the focal point of high numerical aperture lens. It has been found, both theoretically [60] and experimentally [61], that a radially polarized light beam can be focused into a much tighter and deeper spot than a linearly polarized beam. One of the most interesting features of the radial polarization is the formation of a large non-propagating longitudinal component of optical electric field near the beam axis. Conversely, the azimuthal polarization generates a strong magnetic field near the optical axis. Recently, Zhan [62] has studied the properties of circularly polarized vortex beams and has found the proper combination of polarization and topological charge of phase singularity to achieve focusing properties similar to radial polarization. Besides polarization, other parameters such as the pupil amplitude and phase structure of the field play an important role to achieve a very narrow beam with a long depth at focus, high beam quality and high optical efficiency. To this purpose, many different optical beam profiles have been studied both theoretically and experimentally, such as Bessel-Gaussian (BG), Hypergeometric (HyG), Hypergeometric-Gaussian (HyGG), fractional elegant Laguerre-Gauss (fr-eLG), Ince-Gaussian, Laplace-Gauss and Mathieu beams [11–13]. Among them, the radially polarized BG beams have been to date proved to provide the best results. Moreover, Wang et al. [63] have recently calculated that an even tighter and deeper focus spot - a “light needle” - even smaller than the standard diffraction limit, can be obtained from BG beams by adding a suitable binary phase mask to the high numerical aperture focusing system.

In this section, we studied the properties of the HyGG-II modes (2.5.2.3) at the focus of a large aperture lens [14]. We prove that HyGG-II beams may provide better spot size, beam quality and depth of focus than BG beams. Let us consider an aplanatic high-numerical-aperture focusing lens system. The origin $z = 0$ is located at the lens focal point, f , NA, $\alpha = \arcsin(\frac{\text{NA}}{n})$, and $n = 1$ are the focal length, the numerical aperture, the semi-aperture angle, and the vacuum refractive index, respectively. Using the vectorial Debye diffraction integral, Richard and Wolf [59] have shown that the electric field at the point $\tilde{\mathbf{r}} = (\rho, \phi, z)$, in a region close to the focal point in the cylindrical coordinates is given by

$$\tilde{\mathbf{E}}(\tilde{\mathbf{r}}) = -\frac{i}{\lambda} \iint_{\Omega} \tilde{\mathbf{a}}(\theta, \varphi) e^{2\pi i(z \cos \theta + \rho \sin \theta \cos(\varphi - \phi))} d\Omega, \quad (4.42)$$

where $\tilde{\mathbf{a}}(\theta, \varphi)$ is determined by the field distribution in the object space at the pupil and Ω is the solid angle. In Eq. (4.42), ρ and z are dimensionless, their scale length being the λ . Youngworth and Brown [60] have calculated this integral for radially and azimuthally polarized beams. Their calculation showed that the radial polarization is much more effective than the azimuthal and linear ones for obtaining a tight focusing. Therefore, we restrict our attention only to radially polarized beams. The electric field of a radially polarized beam in the focal region is given by

$$\begin{aligned} E_{\rho}(\tilde{\mathbf{r}}) &= \frac{f}{\lambda} \int_0^{\alpha} \sqrt{\cos \theta} \sin(2\theta) l(\theta) J_1(2\pi \rho \sin \theta) e^{i(2\pi z \cos \theta)} d\theta \\ E_z(\tilde{\mathbf{r}}) &= \frac{2if}{\lambda} \int_0^{\alpha} \sqrt{\cos \theta} \sin^2 \theta l(\theta) J_0(2\pi \rho \sin \theta) e^{i(2\pi z \cos \theta)} d\theta, \end{aligned} \quad (4.43)$$

where $J_0(x)$ and $J_1(x)$ are Bessel's functions, and $l(\theta)$ is the amplitude distribution of the pupil apodization function. We consider an amplitude-only apodization function given

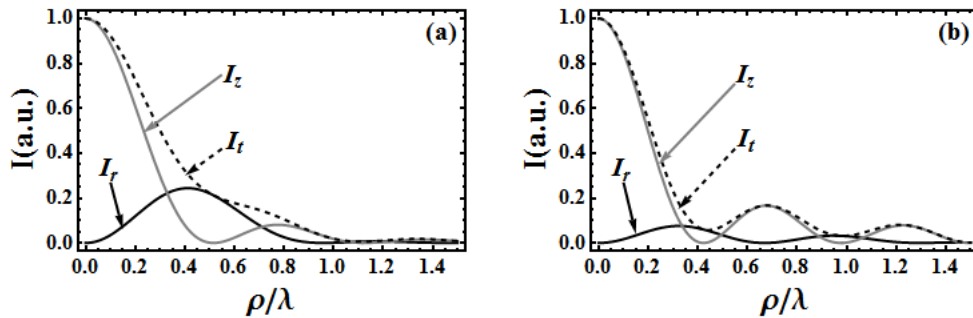


FIGURE 4.14: Intensity profile of the longitudinal and radial field components at the focal point of a high numerical aperture lens (a) and a system of high numerical aperture lens and binary phase mask (b). The black, gray and dashed lines are radial, longitudinal and total intensity, respectively.

by the HyGG-II_{-1,1} profile calculated from Eq. (2.58) with the singular phase factor

omitted. We choose this profile because it exhibits minimum diffraction. Explicitly, $l(\theta)$ is given by

$$l(\theta) = e^{-\beta^2 \left(\frac{\sin \theta}{\sin \alpha}\right)^2} \left(\beta \frac{\sin \theta}{\sin \alpha} \right) {}_1F_1 \left(\frac{1}{2}, 2; \beta^2 \left(\frac{\sin \theta}{\sin \alpha}\right)^2 \right), \quad (4.44)$$

where β is the ratio between the pupil radius and the beam waist. One can solve the integral in Eq. (4.44) numerically and plot the intensities near the focus for any values of the numerical aperture. We have chosen the global adaptive strategy to solve these integrals. In our calculations we considered $\beta = 1$ and $\text{NA} = 0.95$ corresponding to $\alpha = 71.8^\circ$. We compared our results with the well-known apodization function of the BG_1 beam. Fig. 4.14(a) shows the intensity profile of the radial and longitudinal components of the optical field at focus. It is evident that the intensity of the longitudinal component is higher than the radial component. The beam quality is characterized by [63]

$$\eta = \frac{\int_0^{r_0} |E_z(r, 0)|^2 r dr}{\int_0^{r_0} |E_\rho(r, 0)|^2 r dr + \int_0^{r_0} |E_z(r, 0)|^2 r dr} \quad (4.45)$$

where r_0 is the first zero of the radial field component. For the $\text{HyGG-II}_{-1,1}$ profile we found $\eta = 52.5\%$ instead of 44.7% for the BG_1 profile in the same conditions. The hypergeometric apodization function increases the beam quality by 17% . Furthermore, the $\text{HyGG-II}_{-1,1}$ beam size (full width at half maximum, FWHM) is as small as 0.60λ which is 13% less than the beam size of the BG_1 mode (although it is still larger than diffraction limit). Also, its depth focus is about $\sim 1.5\lambda$ which is 1.4% larger than the depth focus of the BG_1 mode. Finally, we calculated the optical electric field near the focal

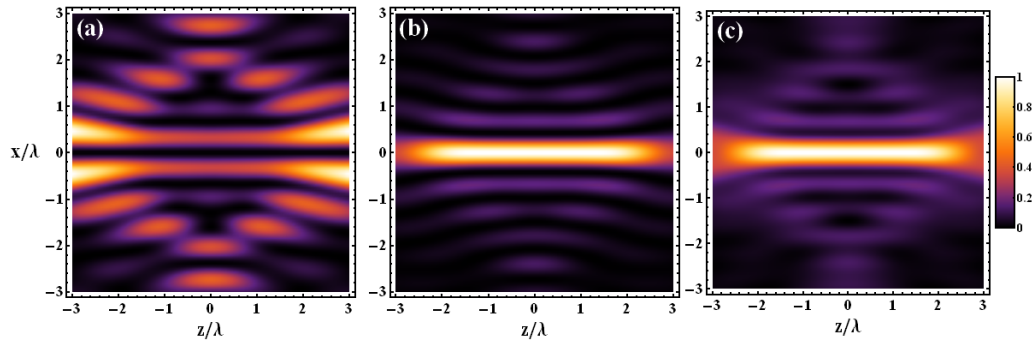


FIGURE 4.15: Density plots of intensity distribution for (a) radial, (b) longitudinal components. (c) the total intensity distribution for the $\text{HyGG-II}_{-1,1}$ beams, respectively.

point when a binary phase mask is inserted just in front of the high numerical aperture system, as in [63]. Our binary phase mask is made of five concentric belts in which the phase of each belt changes by π with respect to neighbor belts [63, 64]. Compared with the mask used in [63] for the BG_1 modes, we introduced some small modifications, i.e., $\theta_1 = 4.46^\circ$, $\theta_2 = 23.64^\circ$, $\theta_3 = 36.53^\circ$, $\theta_4 = 49.03^\circ$, where θ_i are related to the inner

radius of each belts, $r_i = \sin \theta_i / \text{NA}$. The intensity profiles of the radial and longitudinal components of the field in the presence of this phase mask are shown in Fig. 4.14(b). The total field FWHM is 0.426λ , leading to a spot size of $0.142\lambda^2$. These values are 1.6% and 3.2% smaller than the in BG_1 case [63]. Furthermore, the phase mask increases the beam quality to 81.76%, which is improved by 1.7% with respect to the BG_1 profile. Fig. 4.15 shows the intensity distribution for the radial Fig. 4.15(a), longitudinal Fig. 4.15(b) and total field Fig. 4.15(c) of the HyGG-II $_{-1,1}$ profile. It is clear that the depth of focus of the hypergeometric profile is longer than the Bessel-Gauss case and it is about 4.5λ [63].

It is also worth investigating the field distribution obtained at the focus when using vector vortex beams [62] having the HyGG-II profile of Eq. (2.58) with the singular phase retained, but we postponed this problem to the near future.

4.6 Classical communication (Slussarenko et al. [64])

The electromagnetic waves have been recognized as the fastest and most convenient way of long range communication. It is almost two centuries that the telegraph was invented by Claude Chappe. In the last century there has been much effort to find a secure and high-channel-capacity communication method. Besides those mentioned practical features, scientists were interested in having novel communication encoding procedures [41]. Especially, spin angular momentum (SAM) of an electromagnetic wave which is associated to the vectorial property of optical field has been recognized as a good candidate for telecommunication and quantum communication process [30]. SAM is inherently binary, so that only one bit (in the quantum regime - one qubit) can be encoded over a single photon. Of course, this fact bounds quantum communication protocols. Recently, an additional photon degree of freedom associated with the beam phase-front, known as the light orbital angular momentum (OAM), received much attentions for free-space communication [26]. In contrast to the SAM, the OAM is inherently multidimensional, so many novel protocols that were not usable for the binary space now can be used in the OAM space [31]. In this section, I report a novel method to encode information over one photon in the four dimensions OAM Hilbert space where two bits (or qubits in quantum regime) are encoded over a single photon independently of photon polarization state. Indeed, one may encode three bits of information over one photon by considering also SAM in this communication configuration.

4.6.1 Experimental setup

In our experiment we used a q -plate with unit topological charge that corresponds to azimuthally oriented liquid crystal in the transverse plane. The optical retardation of the q -plate was tuned by temperature controller (3.5.2) in such a way that it acted as a half wave plate and induced a value of OAM based on the input polarization [44, 46], according to

$$\begin{aligned}\widehat{QP}_\pi \cdot |L, \ell\rangle &= |R, \ell + 2\rangle \\ \widehat{QP}_\pi \cdot |R, \ell\rangle &= |L, \ell - 2\rangle\end{aligned}\quad (4.46)$$

where $|L\rangle, |R\rangle$ and $|\ell\rangle$ denote the polarization and orbital angular momentum states, respectively and \widehat{QP}_π is the operator representing the action of the q -plate. It is worth noting that we can change the OAM value just by switching the input polarization state with frequencies restricted only by electro-optical speed limitations (order of MHz). The sender (Alice) apparatus was made of a triangular cavity where just one arm was used in the experiment. Due to the presence of the PBS only horizontally polarized light can enter and exit the interferometer. Moreover, the beam OAM, changes in sign under reflection from mirrors and PBS. The tuned q -plate is sandwiched between two quarter wave plates (QWPs) and is inserted in the cavity, as shown in Fig. (4.16-a). In our experiment, a 532 nm TEM₀₀ horizontally polarized laser beam was used. The first QWP was set to change the polarization of the input beam from horizontal to circular $|L\rangle$ and $|R\rangle$. The q -plate coherently transfers this spin state to OAM space, switching the polarization to opposite one and generating beam with OAM value of -2 or +2, respectively. By switching the polarization back to horizontal with the second QWP, the light was led out from the interferometer. If the polarization was changed to vertical, instead, the beam was reflected back by the PBS and remained in the interferometer. Given the same parameters of QWPs, and taking in account odd number of reflections (i.e. the change of the OAM value to opposite one), after the second trip the beam was horizontally polarized and exited the interferometer with OAM value equal to -4 or +4 depending on the angle of the first QWP. This way, Alice was able to generate -4, -2, +2, +4 values of OAM by choosing the proper angles for the QWPs. Table (4.2) shows four possible combinations of QWP angles and their corresponding beam's OAM values. Optionally, one may add Pockels cells before each QWP, so to encode the information in the light beam with rate of the order of MHz. Of course, the length of interferometer must be properly matched with Pockels cells speed. In our experiment, we measured the output beam phase front by making an interference with TEM₀₀ beam. Figure (4.16-(b)) shows the recorded interference pattern for different angles of the

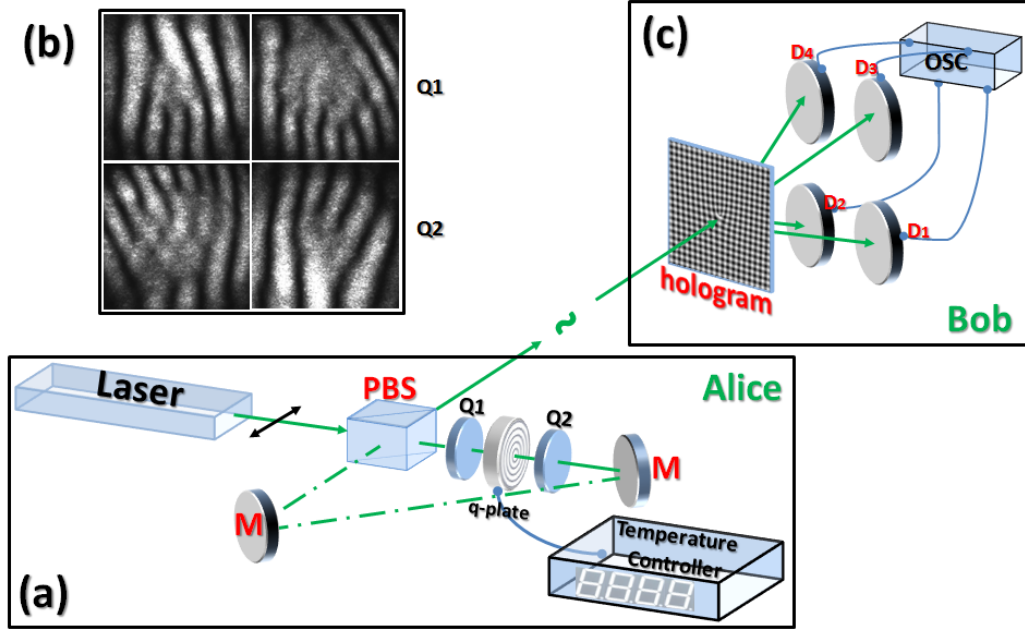


FIGURE 4.16: (a) Alice apparatus: q -plate sandwiches between two QWPs inserted on the Sagnac interferometer, (b) The interference of output beam from the Sagnac interferometer and TEM beam for different QWPs angles corresponding to table (4.2) (c) Bob detector apparatus: a 2D hologram and 4 detectors connected to the oscilloscopes in order to read the $-4, -2, +2, +4$ signals [65].

TABLE 4.2: Four possible combinations of QWP angles and their corresponding beam's OAM values.

Logical bit	QWP1	QWP2	OAM value
00	$+45^\circ$	$+45^\circ$	+2
01	-45°	-45°	-2
10	$+45^\circ$	-45°	-4
11	-45°	$+45^\circ$	+4

QWPs. Bob detector was made of a 2D hologram and 4 detectors, figure (4.16-(c)). The 2D hologram was made by superimposing two computer generated holograms with different topological charges (1 and 3) and orthogonal diffraction angles. This hologram diffracted the beam onto the 4 detectors, according to the beam's OAM values and allowing Bob to decode the information carried by the beam OAM. Our apparatus has been intended for classical telecommunication, but it can be easily applied for single photon quantum communication. Furthermore, another bit can be encoded into the outgoing photon polarization by putting a Pockels cell at the output face of the triangular cavity increasing the total amount of information up to three bits.

Chapter 5

Quantum information application of OAM

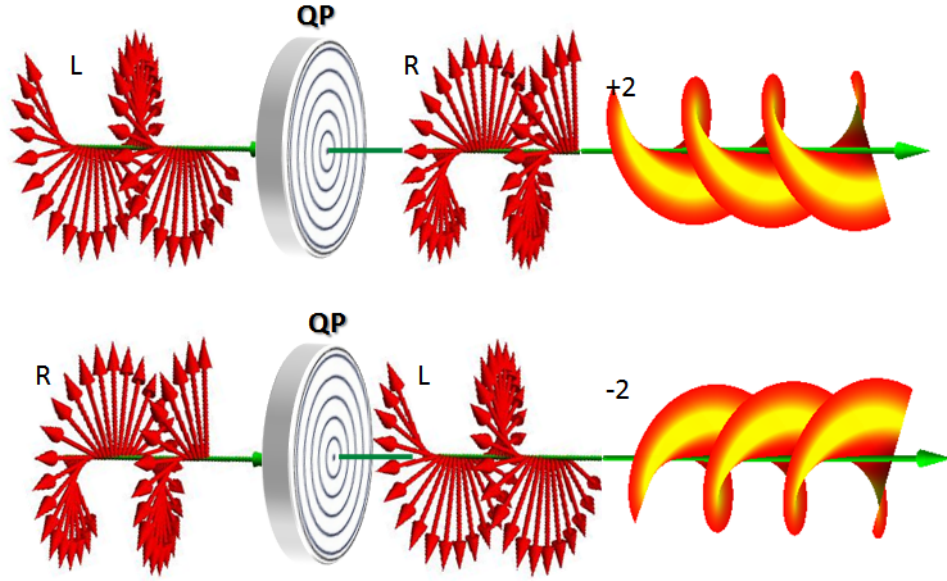
5.1 Introduction

In the previous chapter some new applications of OAM on the classical regime of light has been presented such as: beam shape controlling, generating the needle beam and telecommunication (4).

The main different between SAM and OAM of light is their Hilbert space's dimensions. The SAM is inherently binary and only a qubit can be encoded on its Hilbert space. This limitation of SAM dimensions bounds the quantum protocols which may be implemented. Instead, OAM is infinite dimensional and higher dimension of Hilbert space, "qudit", for quantum applications are available [66].

Aspect et al. demonstrated that the SAM is a quantum number and can be used for quantum protocols. However, after 20 years, the first quantum properties of OAM has been observed by Zeilinger and his coworkers [31]. This experiment confirmed that OAM is a good quantum number as well as SAM. Recently, our group made some new investigations on the quantum properties of OAM of a photon pair. The result shows that, a coherent transferrer of SAM-to-OAM, q -plate, can be used in the quantum regime of light as well as holograms and other OAM generators.

In this chapter, I present some new researches by our group on the OAM quantum regime which have been done with collaboration of De Martini's group at university of La Sapienza in Rome [33, 34, 67]. The first section deals with quantum properties of the q -plate. The observation of Houg-Ou-Mandel (HOM) effect, photon bunching, on the OAM space is presented in the second section. In the third section the bunching of

FIGURE 5.1: Schematic of q -plate action. [19, 48]

two photons with OAM in a beam splitter is presented. Optimal quantum cloning in the OAM space is presented in the fourth section. Finally, I present new devices, made of two q -plates and birefringent wave plates, to built up a universal unitary gate (UUG) on the SAM-OAM four dimension space [68].

5.2 q -plate: single photon quantum formalism

In a single photon quantum formalism, the q -plate acts as the quantum transferrer on the single photon state (up to a global phase factor):

$$|\pm\rangle_{\pi}|\ell\rangle_o \xrightarrow{\widehat{QP}} |\mp\rangle_{\pi}|\ell \pm 2\rangle_o \quad (5.1)$$

where $|\cdot\rangle_{\pi}$ and $|\cdot\rangle_o$ denote the photon quantum state in the in the SAM and OAM spaces, $|+\rangle_{\pi}$ and $|-\rangle_{\pi}$ define the left and right-circular polarization states, respectively [19, 48] (see Fig. (5.1)). It will be convenient to use the field operators instead of ket notation for the following calculations. The creations operator for a tuned (π retardation) q -plate for with unite topological charge are given by

$$\begin{aligned} \hat{a}_{H,\ell}^{\dagger} &\xrightarrow{\widehat{QP}} -\frac{i}{2} \left(\hat{a}_{H,\ell-2}^{\dagger} + \hat{a}_{H,\ell+2}^{\dagger} + i \left(\hat{a}_{V,\ell-2}^{\dagger} - \hat{a}_{V,\ell+2}^{\dagger} \right) \right) \\ \hat{a}_{H,\ell}^{\dagger} &\xrightarrow{\widehat{QP}} +\frac{1}{2} \left(\hat{a}_{H,\ell-2}^{\dagger} - \hat{a}_{H,\ell+2}^{\dagger} + i \left(\hat{a}_{V,\ell-2}^{\dagger} + \hat{a}_{V,\ell+2}^{\dagger} \right) \right) \end{aligned} \quad (5.2)$$

where $\hat{a}_{\pi,\ell}^\dagger$ is a creation operator of a photon with SAM and OAM states of π and ℓ , respectively. In our calculation the radial profile does not play a significant role, so, without losing the generality we have neglected it.

5.3 Holograms and quantum state tomography (Nagali et al. [66])

A full analogy can be drawn between the polarization SU(2) Hilbert space and each subspace of OAM with a given $|m|$, except of course $m = 0$. This analogy is for example useful for retracing the quantum tomography procedure in the OAM space to the standard one for polarization [51, 69]. In particular, it is convenient to consider the eigenstates of OAM $|\pm|m|\rangle$ as the analog of the circular polarizations $|L\rangle$ and $|R\rangle$, as the latter ones are obviously the eigenstates of the SAM. To make the analogy more apparent, small-letter symbols $|l\rangle = | +|m|\rangle$ and $|r\rangle = | -|m|\rangle$ are introduced to refer to the OAM case, while the capital letters are used for the polarization. Following the same convention, the OAM equivalent of the two basis linear polarizations $|H\rangle$ and $|V\rangle$ are defined as

$$\begin{aligned} |h\rangle &= \frac{1}{\sqrt{2}}(|l\rangle + |r\rangle) \\ |v\rangle &= \frac{1}{i\sqrt{2}}(|l\rangle - |r\rangle) \end{aligned} \quad (5.3)$$

Finally, the $\pm 45^\circ$ angle “anti-diagonal” and “diagonal” linear polarizations will be hereafter denoted with the kets $|A\rangle = (|H\rangle + |V\rangle)/\sqrt{2}$ and $|D\rangle = (|H\rangle - |V\rangle)/\sqrt{2}$, and the corresponding OAM states are defined analogously:

$$\begin{aligned} |a\rangle &= \frac{1}{\sqrt{2}}(|h\rangle + |v\rangle) = \frac{e^{-i\pi/4}}{\sqrt{2}}(|l\rangle + i|r\rangle) \\ |d\rangle &= \frac{1}{\sqrt{2}}(|h\rangle - |v\rangle) = \frac{e^{i\pi/4}}{\sqrt{2}}(|l\rangle - i|r\rangle). \end{aligned} \quad (5.4)$$

The holograms used for generating or analyzing the above OAM states were manufactured from a computer-generated image by a photographic technique followed by chemical bleaching, producing pure phase binary holographic optical elements (see section 3.4). The typical first-order diffraction efficiencies of these holograms are in the range 10-15%. The patterns we used are shown in Fig. (5.2). Analogously to polarizers, these holograms are used in two ways: (i) to generate a given input quantum state of OAM; (ii) to analyze a given OAM component of an arbitrary input quantum state.

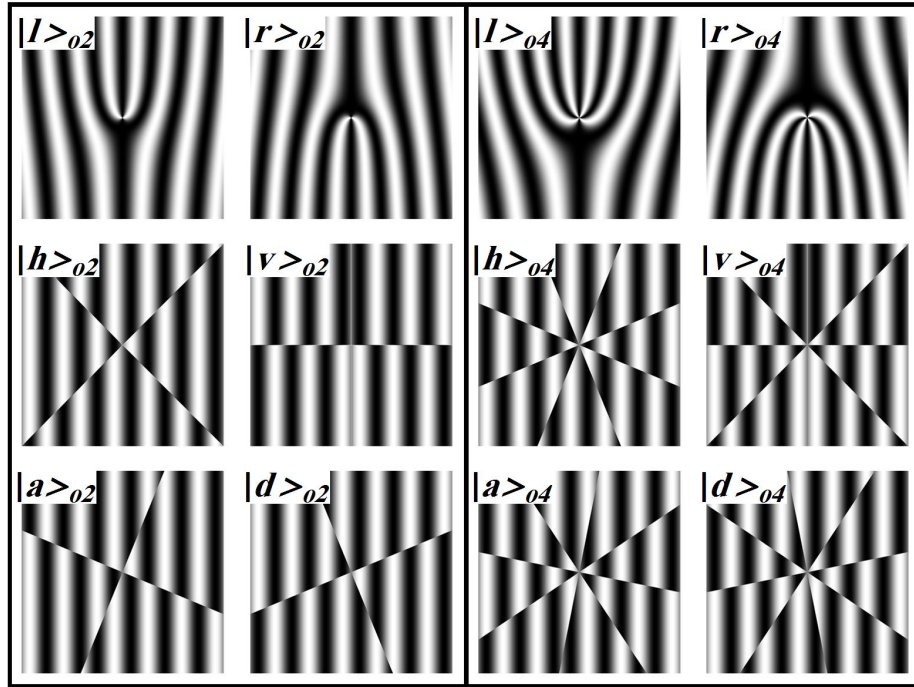


FIGURE 5.2: Patterns of the 12 binary holograms used in this work. The left box refers to the OAM subspace o_2 ($|m| = 2$). The right box to the OAM subspace o_4 ($|m| = 4$). In the upper-left corner of each hologram is shown the quantum state that is generated by the hologram, when using a TEM_{00} input, in the first-order diffraction beam [67].

When using the holograms for generating one of the above OAM states, a TEM_{00} input mode is sent into the hologram and the first-order diffracted mode is used for output. The input beam must be precisely centered on the hologram pattern center. The output OAM quantum state obtained is shown in the upper corner of each hologram pattern in Fig. (5.2). When using the holograms for analysis, the input mode, having unknown OAM quantum state, is sent through the hologram (with proper centering). The first-order diffracted output is coupled to a single-mode optical fiber, which filters only the $m = 0$ state, before detection. It can be shown that the amplitude of this output is then just proportional to the projection of the input state onto the OAM state shown in the upper corner of each hologram pattern, in Fig. (5.2) (except, possibly, for a sign inversion of m in the case of the upper row holograms).

5.4 q -plate as OAM quantum information transfer (Nagali et al. [66])

In order to examine the quantum properties of the q -plate, we have built up four possible setup configurations, shown in Fig. (5.3), corresponding to the implementations of the following devices:

- a) Quantum transferrer from polarization to OAM subspace $|m| = 2$, i.e. $\pi \rightarrow o_2$
- b) Quantum transferrer from OAM subspace $|m| = 2$ to polarization, i.e. $o_2 \rightarrow \pi$
- c) Quantum bidirectional transfer polarization-OAM-polarization, i.e. $\pi \rightarrow o_2 \rightarrow \pi$
- d) Quantum transferrer from polarization to OAM subspace $|m| = 4$, i.e. $\pi \rightarrow o_4$

Each process of quantum information transfer is based on a q -plate (two in the cases c and d) combined with other standard polarizers and waveplates. The OAM state is prepared or analyzed by means of suitably-developed holograms, as discussed in the next Section, preceded or followed by coupling to single-mode fibers, which selects the $m = 0$ state $|0\rangle_o$ before detection. After the analysis, the signals were detected by single photon counters SPCM and then sent to a coincidence box interfaced with a computer, for detecting and counting the coincidences with the trigger D_T (see Fig. (5.3)).

In our experiment [67], the main optical source was a Ti:Sa mode-locked laser, with wavelength $\lambda = 795$ nm, pulse duration of 180 fs, and repetition rate 76 MHz. By second harmonic generation, the output of the laser was converted into a ultraviolet (UV) beam with wavelength $\lambda_p = 397.5$ nm, which was used as pump beam for the photon pairs generation. The residual field at λ was eliminated by means of a set of dichroic mirrors and filters. The UV beam, with an average power of 600 mW, pumped a 1.5 mm thick nonlinear crystal of β -barium borate (BBO) cut for type II phase-matching, working in a collinear regime and generating polarization pairs of photons with the same wavelength λ and orthogonal linear polarizations, hereafter denoted as horizontal (H) and vertical (V). These down-converted photons were then spatially separated from the fundamental UV beam by a dichroic mirror. The spatial and temporal walk-offs were compensated by a half-wave plate and a 0.75 mm thick BBO (C) [70]. Finally, the photons were spectrally filtered by an interference filter with bandwidth $\Delta\lambda = 6$ nm.

In order to work in the one-photon regime, a polarizing beam-splitter (PBS) transmitted the horizontally-polarized photon of the pair and reflected the vertically-polarized one. The latter was then coupled to a single-mode fiber and revealed with a single-photon counter (SPCM), which therefore acted as a trigger of the one-photon state generation. The transmitted photon in the $|H\rangle$ polarization state was coupled to another single-mode fiber, which selected only a pure TEM_{00} transverse mode, corresponding to OAM $m = 0$. The coincidence count rate of the two outputs of the PBS, after coupling into the fibers, was of typically 16-18 kHz.

After the fiber output, two waveplates compensated (C) the polarization rotation introduced by the fiber. Finally, a polarizing beam-splitter and a set of wave plates were used for setting the photon polarization to an arbitrary qubit state $|\varphi\rangle_\pi$. In this way, we prepared the one-photon quantum state $|\varphi\rangle_\pi|0\rangle_o$ for further processing.

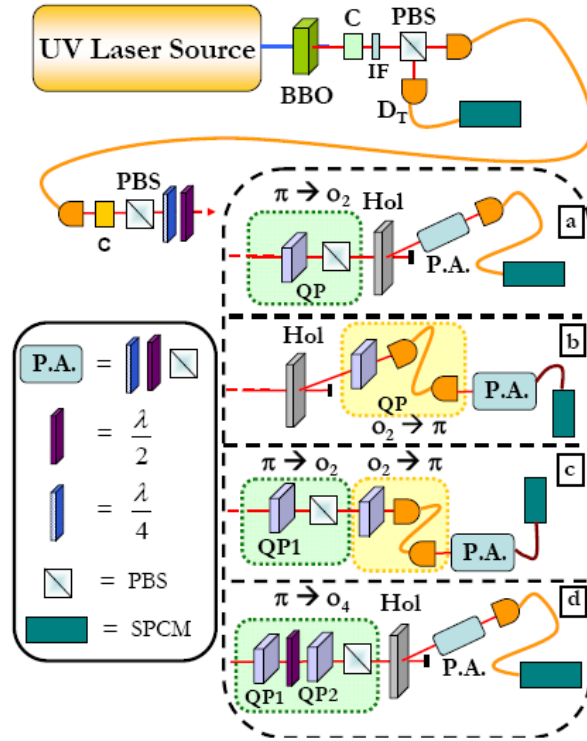


FIGURE 5.3: Schematic representation of the experimental setup. Outside the dashed box is the first section of the apparatus, common to all our experiments. In the dashed box, the four configurations **a**, **b**, **c**, **d** of the second section of the apparatus are shown, used in the four experiments discussed in this paper. Legend: BBO - β -barium borate crystal used for photon-pair generation; C - walk-off compensation stage; PBS - polarizing beam-splitter; D_T - trigger detection unit; QP - q-plate; Hol - hologram; S.P.C.M. - Single photon counter module; P.A. - polarization analysis set, as shown in solid-line box. [67]

5.4.1 Quantum transferrer from SAM to OAM

In the first experiment, we demonstrated that an initial information encoded in an input polarization state can be coherently transferred to the OAM degree of freedom. Let us consider an initial qubit which the information has been encoded over polarization state;

$$|\Psi\rangle_{\text{in}} = |\varphi\rangle_{\pi}|0\rangle_o = (\alpha|H\rangle_{\pi} + \beta|V\rangle_{\pi})|0\rangle_o \quad (5.5)$$

where $|0\rangle_o$ indicates the TEM_{00} mode. A pair of suitably oriented QWPs can be used to convert the basis into the L, R basis. Then, the q -plate can transfer the SAM state into OAM space. The output state, however, is an entangled state on the SAM-OAM spaces. A polarizing beams splitter can be used to trace out the polarization state. The final state after the PBS is, then, given by

$$|\Psi\rangle_{\text{out}} = |H\rangle_{\pi}(\alpha|+2\rangle_o + \beta|-2\rangle_o) = |H\rangle_{\pi}|\varphi\rangle_{o_2}, \quad (5.6)$$

TABLE 5.1: Fidelity values between the experimental states generated by the $\pi \rightarrow o_2$ transferrer and the theoretical ones expected after the conversion in the OAM degree of freedom of the qubit initially encoded in the polarization.

Initial state	Final state	Fidelity
$ H\rangle_\pi$	$ +2\rangle = l\rangle_{o_2}$	(0.990 ± 0.002)
$ V\rangle_\pi$	$ -2\rangle = r\rangle_{o_2}$	(0.972 ± 0.002)
$ A\rangle_\pi$	$ h\rangle_{o_2}$	(0.981 ± 0.002)
$ D\rangle_\pi$	$ v\rangle_{o_2}$	(0.968 ± 0.002)
$ L\rangle_\pi$	$ a\rangle_{o_2}$	(0.998 ± 0.002)
$ R\rangle_\pi$	$ d\rangle_{o_2}$	(0.982 ± 0.002)

where we have assumed a PBS along the horizontal direction. We note that such conversion process is probabilistic, since the state $|\Psi\rangle_{out}$ is obtained with a probability $p = 50\%$, owing to the final polarizing step. Moreover, since we are using the $\{|H\rangle, |V\rangle\}$ basis for the polarization encoding and the $\{|+2\rangle, |-2\rangle\} = \{|l\rangle, |r\rangle\}$ for the OAM one, the transfer is associated also with a rotation of the Poincaré sphere. The correspondence of the six orthogonal states on the polarization Poincaré sphere with the six final ones in the OAM sphere is given in table (5.1) The experimental layout of this scheme is shown in

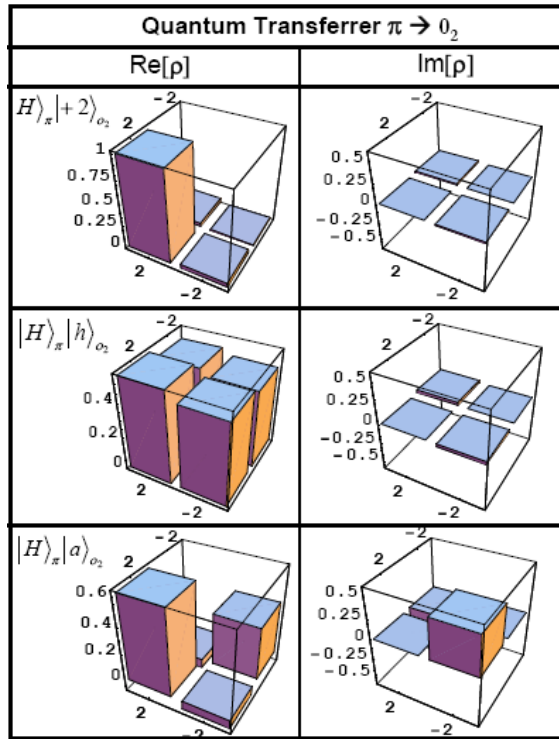


FIGURE 5.4: Experimental density matrices ρ (the left column shows the real part and right column the imaginary part) measured for the output of the $\pi \rightarrow o_2$ qubit transfer, for each of the three different predicted output states shown in the upper left corner of each row [67].

Fig. (5.3), dashed box **a**. The final state tomography has been realized by means of the

TABLE 5.2: Fidelity values between the experimental states generated by the $o_2 \rightarrow \pi$ transferrer and the theoretical ones expected after the conversion in polarization degree of freedom of the qubit initially encoded in the OAM.

Initial state	Final state	Fidelity
$ +2\rangle = l\rangle_{o_2}$	$ H\rangle_\pi$	(0.981 ± 0.002)
$ -2\rangle = r\rangle_{o_2}$	$ V\rangle_\pi$	(0.995 ± 0.002)
$ a\rangle_{o_2}$	$ L\rangle_\pi$	(0.964 ± 0.002)
$ d\rangle_{o_2}$	$ R\rangle_\pi$	(0.972 ± 0.002)
$ h\rangle_{o_2}$	$ A\rangle_\pi$	(0.967 ± 0.002)
$ v\rangle_{o_2}$	$ D\rangle_\pi$	(0.970 ± 0.002)

six holograms shown in Fig. (5.2) (left box). The experimental results for three specific choices of the input state are shown in Fig. (5.4). We found a good agreement with theory as demonstrated by the fidelity parameter, defined as $F = \langle \psi | \rho_{exp} | \psi \rangle$, where $|\psi\rangle$ is the theoretical state to be compared to the experimental one described by density operator ρ_{exp} . The average fidelity in this experiment value between the experimental states and the theoretical predictions is $F = (97.7 \pm 0.2)\%$. The fidelities obtained for six different input states are shown in table (5.1).

5.4.2 Quantum transferrer from OAM to SAM

In the second experiment we showed that the reverse process can be realized as well, by transferring a qubit initially encoded in the OAM subspace o_2 into the polarization space. We consider as initial quantum state of the photon the following one:

$$|\Psi\rangle_{in} = |H\rangle_\pi |\varphi\rangle_{o_2} = |H\rangle(\alpha|+2\rangle + \beta|-2\rangle) \quad (5.7)$$

By injecting the state $|\Psi\rangle_{in}$ in the q -plate device, and then rotating the output state by means of a pair of waveplates, we obtain the following state:

$$\frac{1}{2}\{\alpha|V\rangle|+4\rangle + \alpha|H\rangle|0\rangle + \beta|V\rangle|0\rangle + \beta|H\rangle|-4\rangle\} \quad (5.8)$$

Now, by coupling the beam to a single mode fiber, only the states with $m = 0$ that is, the TEM₀₀ modes, will be efficiently transmitted. Of course, this implies that a probabilistic process is obtained again, since we discard all the contributions with $m \neq 0$ (ideally, again $p = 50\%$). After the fiber, the output state reads:

$$|\Psi\rangle_{out} = (\alpha|H\rangle + \beta|V\rangle)|0\rangle = |\varphi\rangle_\pi |0\rangle_o \quad (5.9)$$

which demonstrates the successful conversion from the OAM degree of freedom to the polarization one. The experimental layout of this “reverse” scheme is shown in Fig. (5.3),

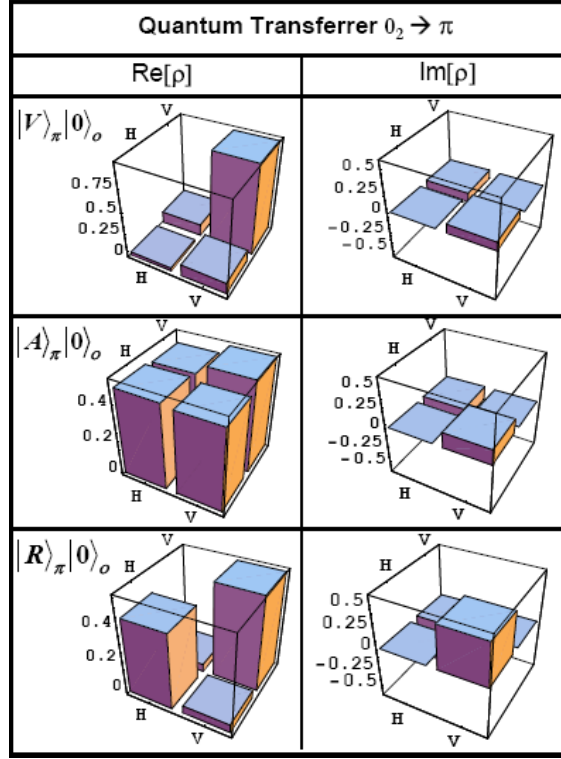


FIGURE 5.5: Experimental density matrices ρ (the left column shows the real part and right column the imaginary part) measured for the output of the $o_2 \rightarrow \pi$ qubit transfer, for each of the three different predicted output states shown in the upper left corner of each row [67].

dashed box **b**. The input qubit in OAM is prepared using one of the six holograms shown in Fig. (5.2) (left box), as explained in the previous Section. The output state is analyzed by standard polarization-state quantum tomography. The experimental results for three cases are shown in Fig. (5.5). We find again a good agreement with theory, with an average fidelity $F = (97.3 \pm 0.2)\%$, and the specific cases shown in table (5.2). We note that this OAM-to-polarization transferrer allows a simple detection of the sign of the OAM, with a theoretical efficiency of 50%, much larger than what is typically obtained by the fork holograms (10% ÷ 30%). Therefore, this scheme can be used as a very efficient OAM detector.

5.4.3 Bidirectional transfer SAM-OAM-SAM

Having demonstrated polarization-to-OAM transfer and OAM-to-polarization transfer, it is natural to try both schemes together, in a bidirectional transfer which starts and ends with polarization encoding, with OAM as an intermediate state which can be used for example for communication. This is also the first quantum experiment based on the combined use of two q -plates. Although this test in principle is not involving any

TABLE 5.3: Fidelity values between the input and output states for the bidirectional $\pi \rightarrow o_2 \rightarrow \pi$ transferrer.

Initial state and final state	Fidelity
$ H\rangle_\pi$	(0.970 ± 0.002)
$ V\rangle_\pi$	(0.972 ± 0.002)
$ A\rangle_\pi$	(0.958 ± 0.002)
$ D\rangle_\pi$	(0.955 ± 0.002)
$ R\rangle_\pi$	(0.934 ± 0.002)
$ L\rangle_\pi$	(0.962 ± 0.002)

new idea with respect to the previous two experiments, it is important to verify that in practice the efficiency of the optical manipulation is not strongly affected by the number of q -plate employed, for example due to alignment criticality.

The layout is shown in Fig. (5.3), dashed box **c**, and corresponds to the sequence of the two schemes discussed above. In Fig. (5.6) we show some density matrices obtained by the quantum tomography technique in the polarization degree of freedom of the output state. As can be observed in table (5.3), the experimental results are in good agreement

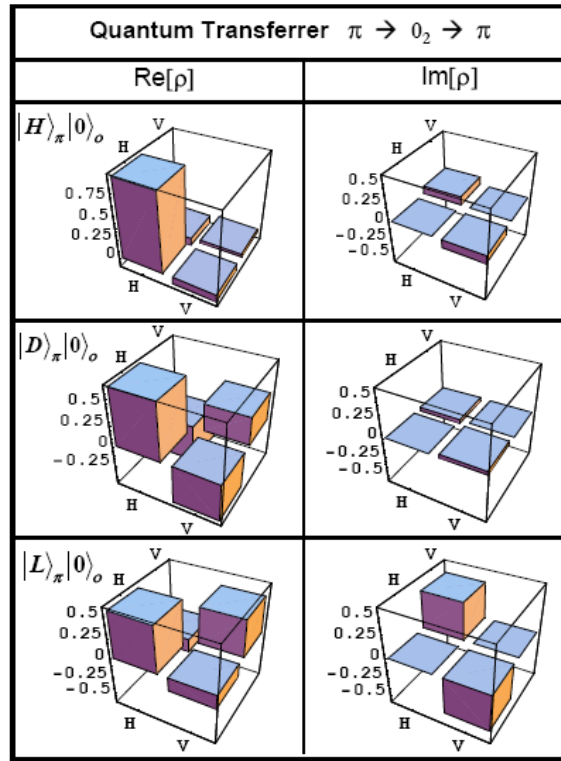


FIGURE 5.6: Experimental density matrices measured in the polarization degree of freedom after the bidirectional $\pi \rightarrow o_2 \rightarrow \pi$ transferrer. In each box is reported the expression of the initial and final state, to be compared with the experimental one described by the density matrix. [67].

with the theoretical predictions, with a mean fidelity value equal to $F = (95.9 \pm 0.2)\%$.

We see that the overall fidelity is still quite good, so that there seem to be no significant problem into the combined use of many q -plates in a cascaded configuration. After the two q -plates the quantum efficiency of the conversion process, defined as the capability to convert a TEM₀₀ mode in a pure Laguerre-Gaussian, is still around 80% (to optimize the efficiency, the q -plate birefringent retardation δ were tuned by mechanical pressure).

5.4.4 Manipulation of OAM in the subspace $|m| = 4$

In the bidirectional transfer, we have experimentally demonstrated that it is possible to work with two sequential q -plates without a significant lowering of the overall efficiency. This approach can be also adopted to access higher-order subspaces of the orbital angular momentum, by moving from one subspace to the next using a sequence of QPs alternated with half-wave plates [44].

Experimentally we have studied the case of two sequential q -plates QP₁ and QP₂ (both with $q = 1$). We demonstrate that it is possible to efficiently encode the quantum information in the OAM basis $\{|+4\rangle, |-4\rangle\}$, by exploiting the spin-orbit coupling in the q -plates. In order to analyze the orbital angular momentum with $|m| = 4$ we have adopted newly designed holograms, shown in Fig. (5.2) (box on the right).

An initial state in the TEM₀₀ mode and arbitrary polarization $|\varphi\rangle_\pi = (\alpha|H\rangle + \beta|V\rangle)$ is transformed by a pair of quarter-wave plates and QP₁ into the following one:

$$|\varphi\rangle_\pi|0\rangle_l \rightarrow (\alpha|R\rangle|-2\rangle + \beta|L\rangle|+2\rangle) \quad (5.10)$$

A HWP then inverts the polarization of the output state after QP₁, so that we get:

$$\alpha|L\rangle|+2\rangle + \beta|R\rangle|-2\rangle \quad (5.11)$$

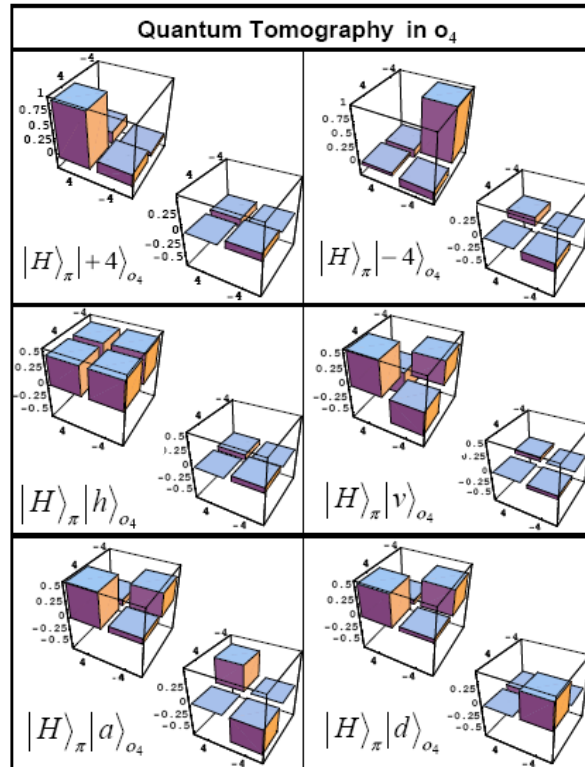
Next, the action of QP₂ and a polarizer leads to the final state:

$$(\alpha|+4\rangle + \beta|-4\rangle)|H\rangle = |\varphi\rangle_{o_4}|H\rangle_\pi \quad (5.12)$$

By changing the different hologram masks, we have carried out the quantum state tomography reported in Fig. (5.7). The fidelity related to each state is reported in table (5.4), and the high accordance between theory and experimental data leads to an average value $F = (96.1 \pm 0.2)\%$.

TABLE 5.4: Fidelity values between the expected and the experimental states generated by the $\pi \rightarrow o_4$ transferrer.

Initial state	Final state	Fidelity
$ H\rangle_\pi$	$ +4\rangle = l\rangle_{o_4}$	(0.947 ± 0.002)
$ V\rangle_\pi$	$ -4\rangle = r\rangle_{o_4}$	(0.958 ± 0.002)
$ L\rangle_\pi$	$ a\rangle_{o_4}$	(0.992 ± 0.002)
$ R\rangle_\pi$	$ d\rangle_{o_4}$	(0.923 ± 0.002)
$ A\rangle_\pi$	$ h\rangle_{o_4}$	(0.994 ± 0.002)
$ D\rangle_\pi$	$ v\rangle_{o_4}$	(0.955 ± 0.002)

FIGURE 5.7: Experimental density matrices measured in the OAM basis $\{|+4\rangle, |-4\rangle\}$ for different predicted final states, shown in the lower-left corner of each panel. [67].

5.5 Hong-Ou-Mandel effect via OAM (Nagali et al. [32])

As we know, photon is a boson. Therefore, two identical photons can interfere together. This effect called photon bunching (or Hong-Ou-Mandel effect) on the quantum optics. Hong, Ou and Mandel (HOM) on 1987 demonstrated experimentally that two identical single photons can interfere together on a 50 : 50 beam splitter [71]. They generated two photons, says *idler* and *signal*, by the SPDC. These two photons were impinging on two different faces of a beam splitter (BS). When the photons are distinguishable, there are four probabilities to having photons on the exit faces: two photons on the **A** exit face, two photons on the **B** exit face, idler on the **A** exit face and signal on the **B** exit

face or *vice versa*, **A**, and **B** denote two different exit faces of BS. If two detectors record the photon counts on the exit faces, there will be a coincidence between these detectors. Let us now consider a situation where two photons are indistinguishable. In this case, the two photons will always exit the beam splitter together in the same output face. Therefore, there will be no coincidence between two detectors. This phenomenon cannot be explained by classical optics and is purely a quintessentially quantum phenomenon. The HOM effect can be investigated on the two-photon OAM degrees of freedom too, which shows that the q -plate can transfer coherently the photon-photon correlation from the SAM to the OAM space. This experiment shows that the q -plate can be used in the quantum regime of light as well as in the classical regime. Let us consider the case of two independent linearly polarized signal and idler photons, one horizontal and the other vertical, going through the q -plate: each will undergo the q -plate transformation given in Eq. (5.1)

$$\widehat{QP}_\pi \cdot |1_s\rangle_{H,0}|1_i\rangle_{V,0} = \frac{i}{2} (-|1_s, 1_i\rangle_{L,2} + |1_s\rangle_{L,-2}|1_i\rangle_{R,2} + |1_s\rangle_{R,2}|1_i\rangle_{L,-2} + |1_s, 1_i\rangle_{R,-2}) \quad (5.13)$$

where $|1_s\rangle_{S,O}$ denotes the number of photon with S, O Spin and OAM states, respectively. The two outgoing photons will end up having opposite OAM values 50% of the times. If the two photons are indistinguishable the output beam at the exit face of q -plate will be

$$|\Psi_{out}\rangle = \frac{i}{\sqrt{2}} (|0\rangle_{L,-2}|2\rangle_{R,2} - |2\rangle_{L,-2}|0\rangle_{R,2}) \quad (5.14)$$

where we have used the multi photon quantum states notation. Equation (5.14) shows that the probability of having one photon in state $+2$ and other photon in -2 state is zero. The output from the q -plate is detected by a double pitch hologram and two detectors put in the two first order in order to detect the $+2$ and -2 OAM states. Then, in case of indistinguishable photons, there will be no coincidence between the detectors, while for distinguishable photons the destructive interference disappears and the coincidences between the two detectors appear. The q -plate action can be again interpreted as a mode converter, coherently transferring the two-photon quantum correlation from the SAM degree of freedom to the OAM one. The experimental setup is shown in Fig. (5.8). The coincidence between $[D_A, D_B]$ detects the state contribution of $|1\rangle_{l=2}|1\rangle_{l=-2}$. Due to the coalescence interference, for otherwise identical photons the coincidence signal is vanishing in the state outcoming from the q -plate. In order to study the transition from the case of classical behavior (distinguishable photons) to the case of full quantum interference, a variable temporal delay t_d between the H and V polarizations in the state $|\Psi_{in}\rangle$ has been introduced (Q in Fig. (5.8)). The experimental visibility of the quantum interference shown in Fig. (5.9-a) is $V_{exp} = (0.95 \pm 0.02)$. As a further

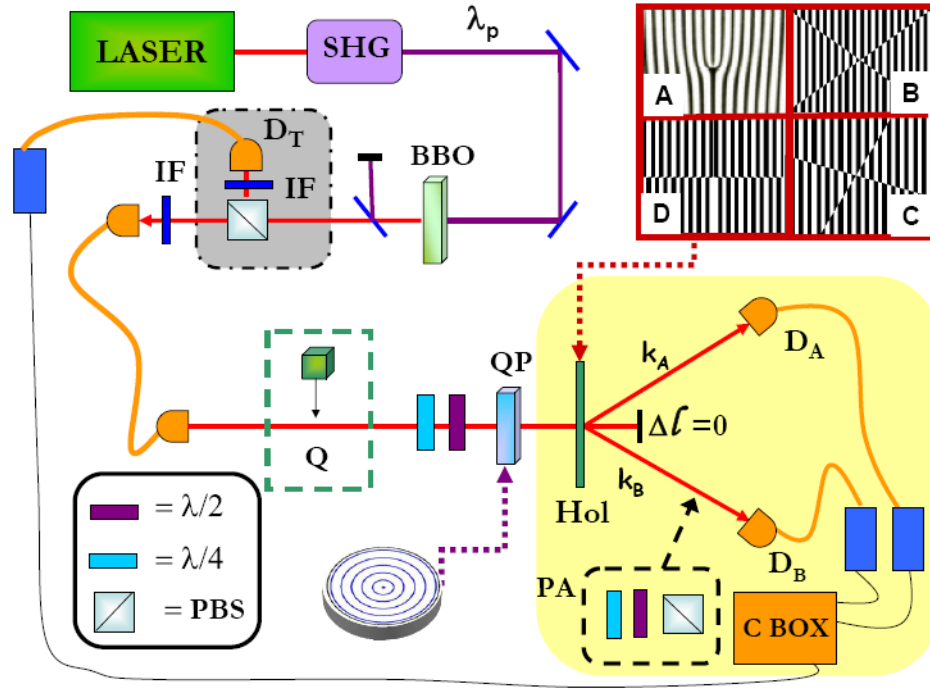


FIGURE 5.8: A Ti:Sa mode-locked laser converted by second harmonic generation (SHG) into a beam with wavelength $\lambda_p = 397.5\text{nm}$. This field pumps a nonlinear crystal of β -barium borate (BBO) which emits a single-mode biphoton state with H and V polarizations and $\lambda = 795\text{nm}$, filtered by the interference filter (IF) with $\Delta\lambda = 6\text{nm}$ and then coupled to a single mode fiber. The gray dot-dashed box has been optionally inserted to prepare a single photon state triggered by detector D_T . Birefringent quartz crystals (Q) having different thicknesses were used to introduce a controlled temporal delay between the two photons. After setting the input polarization by means of a suitably oriented quarter-wave plate, the photons were sent through the q -plate (QP) and the output OAM states were analyzed with the help of a hologram (Hol). In OAM-to-spin conversion experiments, Hol and QP were interchanged. To measure (or prepare) OAM states in the basis $l = \pm 2$, a double-fork hologram has been used (inset A), so that the OAM state of the first diffracted modes is shifted by $\Delta l = \pm 2$, while the undiffracted 0-order beam has $\Delta l = 0$. The photons on the first diffracted modes are then coupled to single mode fibers which select output states with $l = 0$ and convey them to the detectors D_A and D_B . Hence, the detection of a photon in D_A (D_B) corresponds to a photon incident on the hologram with OAM $l = +2$ ($l = -2$). The 1st-order diffraction efficiency of the hologram was $\sim 10\%$. The measurement (or preparation) of OAM in superposition states has been realized by adopting the other holograms shown in the inset. (The hologram B refers to $|d_+\rangle_l$, C to $|d_R\rangle_l$, D to $|d_-\rangle_l$, $|d_L\rangle_l$ was also analyzed by hologram C after reversing its orientation"). Due to reflection losses, the transmittance of the q -plate is $T \sim 0.90$ [33].

confirmation, we have measured the contribution of two photons with $l = +2$ by recording the coincidence counts between two detectors $[D_A, D'_A]$ placed on the output modes of a fiber-based beam splitter inserted on the same k_A diffracted mode (not shown in figure). Theoretically, the coalescence of the two photons should lead to a coincidence enhancement by a factor $\Gamma = 2$, and experimentally we found $\Gamma_{exp} = (1.94 \pm 0.02)$. For

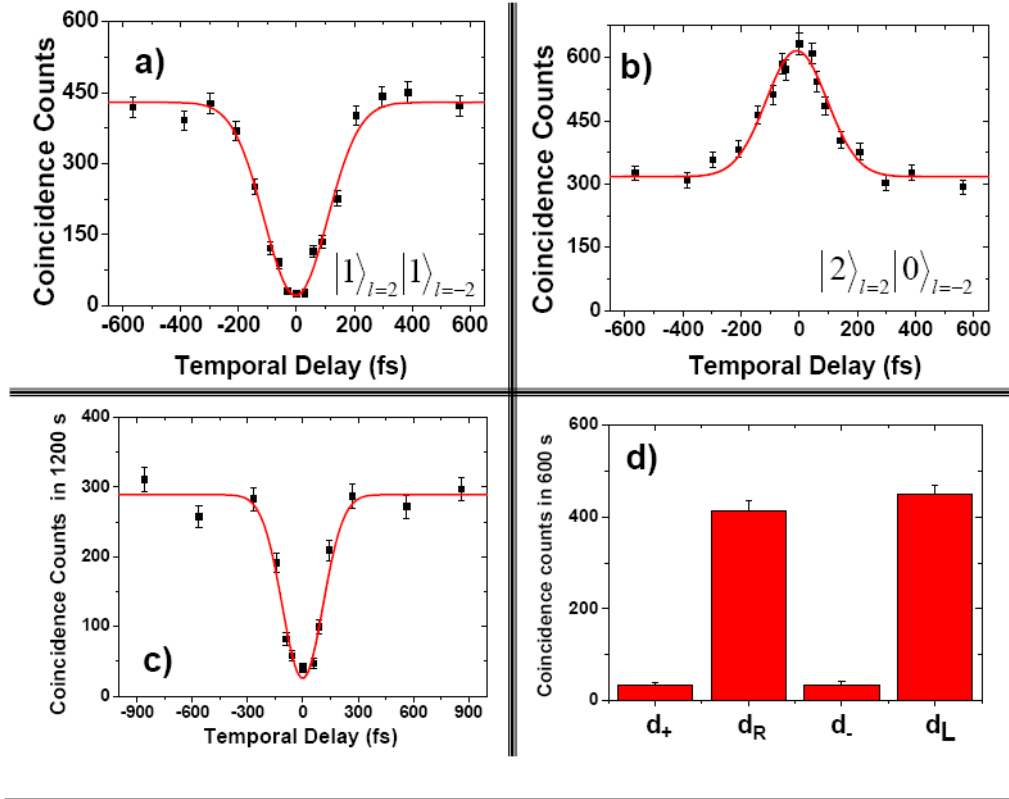


FIGURE 5.9: Coincidence counts between $[D_A, D_B]$ versus the temporal delay t_d , for the state $|\Psi_{out}\rangle$. The continuous line shows the best fit of the experimental data. (b) Coincidence counts $[D_A, D_{A'}]$ versus t_d . (c) Coincidence counts $[D_A, D_B]$ versus t_d ($V = 0.91 \pm 0.01$) for the state $|\Phi_{out}\rangle$. (d) Coincidence counts $[D_A, D_{A'}]$ in different OAM bases. [33].

the sake of completeness, we verified that even after erasing all information still contained in the polarization degree of freedom, the final state is still coherent and exhibits the same non-classical photon correlations in OAM. To this purpose, we let both the two photons pass through a horizontal linear polarizer set in a common state H . We verified again the coalescence of the photons by a measurement similar to the previous one: Fig. (5.9-c). To verify that we really obtain a coherent state and not a statistical mixture having similar OAM correlation properties, we measured the coherence between the two contributions with opposite OAM states. This was accomplished by analyzing the photons in the other OAM bases already discussed above. Therefore, our coherence verification is actually turned into a measurement of two photons in the same OAM state ($|d_+\rangle, |d_-\rangle, |d_R\rangle, |d_L\rangle$). As expected, for ($|d_+\rangle, |d_-\rangle$) the events of two photons with the same orbital states are strongly suppressed, while for ($|d_R\rangle, |d_L\rangle$) they are doubled, with an overall correlation visibility $V = (0.86 \pm 0.02)$ (Fig. (5.9 (d))). This shows that q -plates transfer not only single-photon information between polarization and OAM, but also multiphoton-encoded information (e.g. biphotons).

5.6 OAM quantum cloning (Nagali et al. [33])

An unknown qubit $|\psi\rangle$ cannot be copied without error. This is a consequence of the principles of quantum mechanics, as proved in the so-called quantum no-cloning theorem. It is however still possible to make an imperfect copy, with a maximum quantum fidelity $F = 5/6$. This corresponds to saying that the copied qubit has a $5/6$ probability of being exactly equal to the qubit to be copied and a $1/6$ probability of being orthogonal to it. The copied qubit is in mixed state that can be described by the following density matrix:

$$\hat{\rho}_{clon} = \frac{5}{6}|\psi\rangle\langle\psi| + \frac{1}{6}|\psi^\perp\rangle\langle\psi^\perp| \quad (5.15)$$

where ψ^\perp stands for the state orthogonal to ψ . There exist different demonstrated approaches to implementing the optimal quantum cloning of photons. A particularly simple one is that based on the so-called symmetrization technique, involving the HOM coalescence effect in a BS [72]. This technique has been already demonstrated with polarization [72], and now it becomes possible to replicate such results with OAM photon qubits. The working principle is based on the introduction of the photon to be cloned, carrying a OAM qubit $|\psi\rangle = \alpha|+2\rangle + \beta|-2\rangle$ in one of the two input ports of the BS, and of an ancilla photon in a totally random mixed state $\hat{\rho} = \frac{1}{2}(|+2\rangle\langle+2| + |-2\rangle\langle-2|)$ in the other input port.

The output is given by the two photons that are emerging from the same output port of the BS. The cloning will be successful only when the two photons came out together from such a port, otherwise the process fails. Therefore this implementation is a probabilistic one, and it can be shown that its success probability is $\frac{3}{8}$ (if using only one output port of the BS, it is doubled to $\frac{3}{4}$ if both ports are used). Now, the randomized photon, after being reflected in the BS, can be considered as a mixture of a photon having state $|\psi\rangle$ and state $|\psi^\perp\rangle$ with equal probabilities. Since the probability of the two photons of coming out together is doubled when the output photons are in the same state, it is easy to see that the output will correspond to two identical photons for $\frac{2}{3}$ of the times and to two orthogonal photons for $\frac{1}{3}$ of the times. Each photon of the output pair will therefore have $\frac{2}{3} \times 100\% + \frac{1}{3} \times 50\% = \frac{5}{6}$ probability of being identical to the input photon to be copied and this is just the optimal fidelity.

We have experimentally demonstrated this optimal cloning by preparing the two input photons by means of the q -plate SAM \rightarrow OAM quantum transfer devices and by analyzing the output after a OAM \rightarrow SAM transfer [34]. The randomized photon was obtained by randomizing the polarization before the transfer (by a random rotation of waveplates). The cloned photons were found to have an average fidelity of about 0.80 to

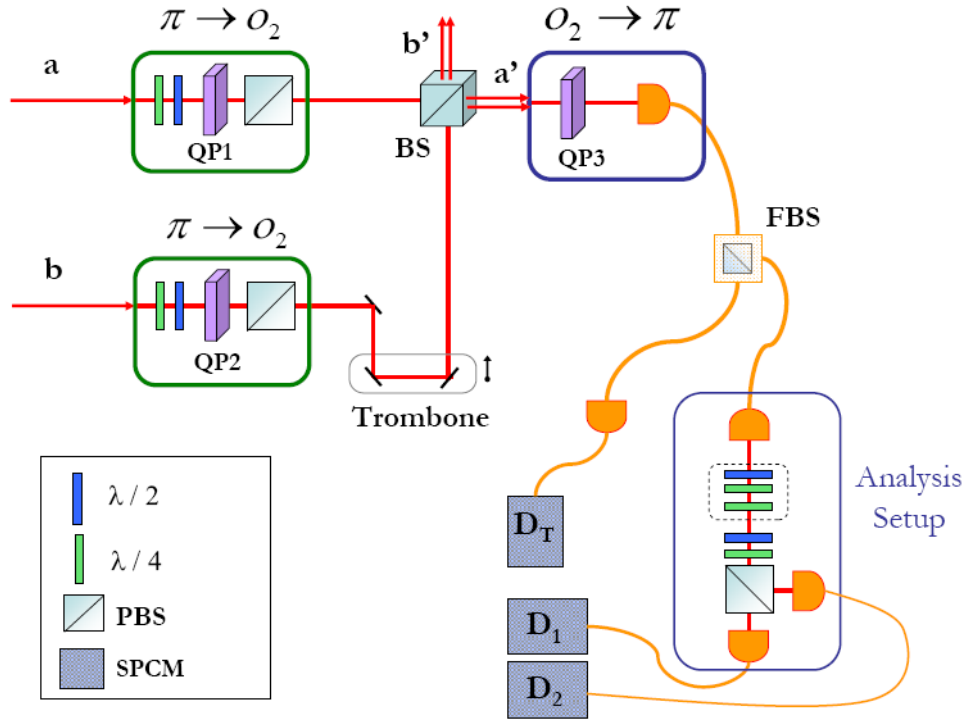


FIGURE 5.10: Experimental setup of the cloning process of the OAM states. The main source of the photons (not shown in figure) injected on modes a and b is a Ti:Sa mode-locked laser converted by second harmonic generation into a UV beam with wavelength $\lambda_p = 397.5\text{nm}$. This field pumps a nonlinear crystal of β -barium borate which emit photon pairs with H and V polarizations and $\lambda = 795\text{nm}$, filtered by the interference filter with $\Delta\lambda = 6\text{nm}$ and then coupled to a single mode fiber. The coincidence rate of the source is equal to 16kHz . The two OAM states generated by the q -plate device on modes a and b interfere on a beam splitter (BS). The two-photons state emerging on mode a' pass through the transferer $o_2 \rightarrow \pi$, is injected on a fiber integrated beam splitter (FBS) and then is analysed by a standard polarization analysis setup. [34].

the input one, fully compatible with the $\frac{5}{6}$ expectation value after taking into account the finite fidelity of the quantum transfer devices.

5.7 q -box (Slussarenko et al. [67])

A proposal for quantum computation application was also made for the q -plate, especially as a device that can not only generate, but also manipulate single-photon entangled spin-orbit states, via quantum gates. These gates are the key element for any quantum algorithm and are the devices that represents a certain linear operator that acts on the input state. A certain number of quantum gates were proposed for single-photon states, entangled in polarization and linear momentum, for example controlled-NOT (C-NOT) gate[ref], which is one of the most important and basic for any algorithm gates, or even a universal gate that has adjustable parameters and can perform any operation

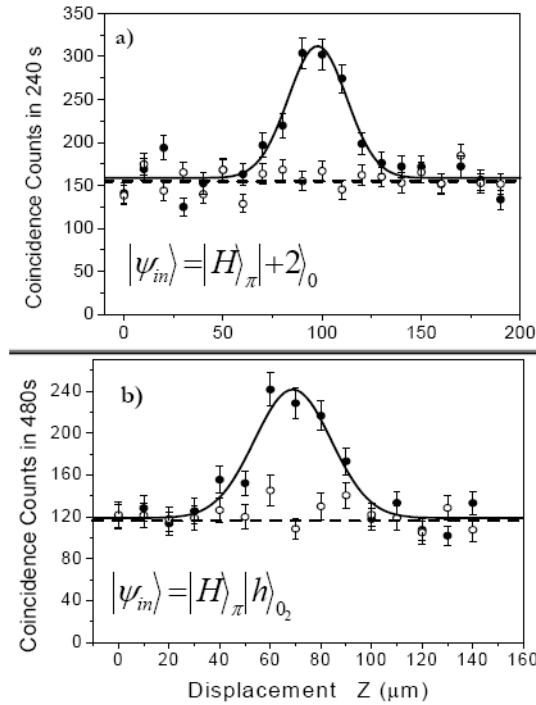


FIGURE 5.11: Experimental Hong-Ou-Mandel effect. **a)** Injection on the BS of the same LG state (black spots) and orthogonal LG states (empty spots). The solid curve represents the best fit based on theoretical prediction. **b)** Injection on the BS of the same HG state (black spots) and orthogonal HG states (empty spots) [34].

on any input state[ref]. In the 2D SAM space such unitary gate that can change the input polarization state to any other we want, is made of two quarter wave plates, one half wave plate together with a phase retardation plate. The adjustable parameters in this universal gate, four in total, are the angles of optical axes orientations of the wave plates and phase retardation of the isotropic plate. A possible implementation of universal unitary gate for the 4D spin-orbit (2D SAM and 2D restricted OAM) space can be made using q -plates. The idea is essentially the same that was used for the mode sorter, described in the section (3.5.3), and uses the spatial separation of the $\ell = 0$ and $\ell = |4|$ modes in the transverse plane. The basic element is a so-called q -box which is made of two q -plates and a unitary spin gate sandwiched between them. The radius of the wave plates of the spin gate is selected so to act only on the $\ell = 0$ mode. For having good spatial modes separation and remove any possible decoherence due to the entanglement of radial modes of the generalized LG beam (that carries different values of p quantum number) two additional lenses are required. The first one allows the spin gate, placed at its focal plane to act in the far field of the beam, while the second one returns back and removes possible radial modes entanglement. A schematic illustration of the q -box is presented in the Fig. (5.12). The input state in the spin-orbit space is first transformed by the first q -plate into $\ell = 0$ and $\ell = |4|$ modes. After that the

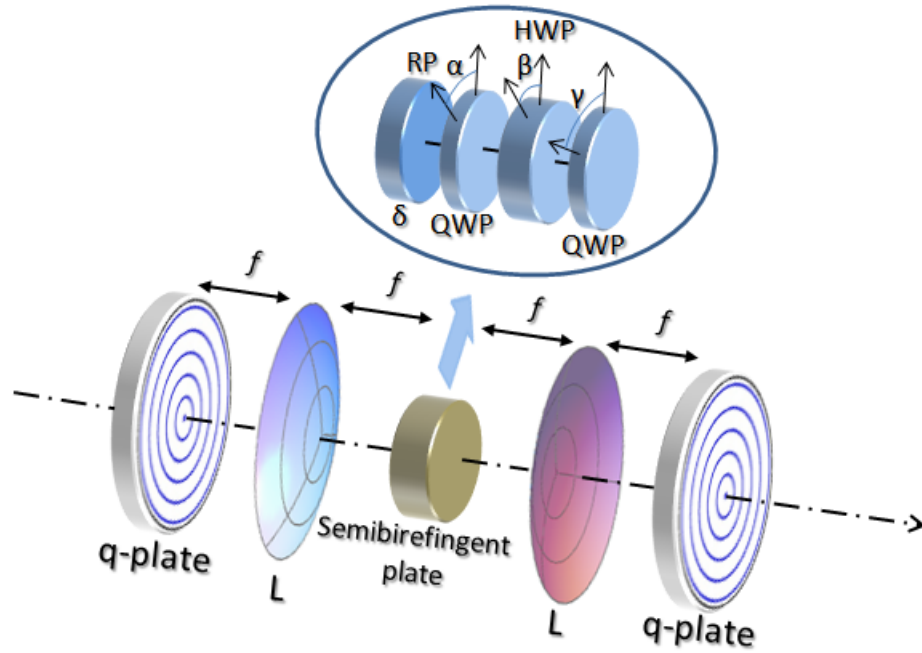


FIGURE 5.12: The scheme of the q -box. The structure of the birefringent plate is shown in the inset. QWP, HWP, and RP are the quarter-wave, the half-wave, and the retardation plates, respectively. α , β , and γ indicate rotations of the QWP, the HWP, and the RP, and δ is the retardation of the isotropic plate. The birefringent plate realizes a SAM-UUG affecting the OAM $\ell = 0$ part of the beam only and it is placed in the common focal plane of the two lenses L. The local optical axis of both q -plates is tangent to the concentric circles so that $q = 1$. The optical retardation of both q -plates is $\lambda/2$ [68].

$\ell = 0$ part polarization state is changed by the spin gate, while the $\ell = |4|$ part remains unchanged. The last q -plate recombines back the two parts, returning the overall state into the spin-orbit space. Because of the presence of the small overlapping of $\ell = 0$ and $\ell = |4|$ modes (same as in the mode sorter) the fidelity of the q -box is not 100%. This value depends on the input light state and on the radius of the spin gate, inserted into the q -box. Theoretical estimations predict that by suitable selection of the radius of the wave-plates the q -box can have minimum guaranteed fidelity of around 83% (rising up to 100% for some states). This value is in good compliance with experimental results of the mode sorter experiment. Some methods to increase the fidelity, sacrificing the intensity of the output beam were already discussed in section (3.5.3). A cascade of four q -boxes, separated by quarter and half wave plates in following order: QB \rightarrow QWP \rightarrow QB \rightarrow HWP \rightarrow QB \rightarrow QWP \rightarrow QB will make a 16-parameter unitary gate that will correspond to a 4x4 unitary matrix which is universal, meaning that by adjusting the parameters one can realize any unitary operation on the spin-orbit state of the photon. Such construction, being general one, however, is not always necessary. Many noted and important gates can be realized with fewer elements. For example, the C-NOT gate can be made with just one q -box with only one half wave plate inside.

Appendix A

Spherical wave solution of scalar wave equation

Let us consider a scalar field which satisfying the scalar wave equation

$$\left(\nabla^2 - \frac{1}{c^2} \frac{\partial^2}{\partial t^2}\right) \psi(\mathbf{x}; t) = 0 \quad (\text{A.1})$$

without lose of generality we can expand $\psi(\mathbf{x}; t)$ in the time Fourier space

$$\psi(\mathbf{x}; t) = \int_{-\infty}^{+\infty} \tilde{\psi}(\mathbf{x}; \omega) e^{-i\omega t} d\omega \quad (\text{A.2})$$

where $k = \frac{\omega}{c}$.

In the main cases, our problem has some symmetrical properties about origin. Therefore, it is convenient to have a fundamental solution in the spherical coordinate. Spherical harmonics, apart the radial part, are a complete set of solution in the spherical coordinate. So, $\tilde{\psi}(\mathbf{x}; \omega)$ can be expand in this complete basis

$$\tilde{\psi}(\mathbf{x}; \omega) = \sum_{l,m} f_{l,m}(r) Y_{l,m}(\theta, \phi) \quad (\text{A.3})$$

where $Y_{l,m}(\theta, \phi)$ are the spherical harmonics and are given by

$$Y_{l,m}(\theta, \phi) = \sqrt{\frac{(2l+1)(l-m)!}{4\pi(l+m)!}} P_l^m(\cos \theta) e^{im\phi} \quad (\text{A.4})$$

where $P_l^m(\cos \theta)$ is the associated Legendre polynomial. $f_{l,m}(r)$ is the radial functions and must satisfy the following radial equation

$$\left(\frac{d^2}{dr^2} + \frac{2}{r} \frac{d}{dr} + k^2 - \frac{l(l+1)}{r^2} \right) f_l(r) = 0 \quad (\text{A.5})$$

It is evident, from equation (A.5), that the radial functions only depend on l , so I have removed subscript m . A possible solution of radial equation is

$$f_{l,m}(r) = \frac{A_{l,m}}{r^{\frac{1}{2}}} J_{l+\frac{1}{2}}(kr) + \frac{B_{l,m}}{r^{\frac{1}{2}}} N_{l+\frac{1}{2}}(kr) \quad (\text{A.6})$$

where $J_n(x)$ and $N_n(x)$ denote first and second kind of the Bessel functions, respectively. However, it maybe proper to transform the radial solution into Hankel's functions

$$f_{l,m}(r) = A_{l,m}^{(1)} h_l^{(1)}(kr) + A_{l,m}^{(2)} h_l^{(2)}(kr) \quad (\text{A.7})$$

where Hankel's functions are given by

$$h_l^{(1,2)}(x) = \sqrt{\frac{\pi}{2x}} \left(J_{l+\frac{1}{2}}(x) \pm i N_{l+\frac{1}{2}}(x) \right). \quad (\text{A.8})$$

So, the general solution of equation (A.1) in the spherical coordinate can be written

$$\tilde{\psi}(\mathbf{x}; \omega) = \sum_{l,m} \left(A_{l,m}^{(1)} h_l^{(1)}(kr) + A_{l,m}^{(2)} h_l^{(2)}(kr) \right) Y_{l,m}(\theta, \phi) \quad (\text{A.9})$$

where the coefficients $A_{l,m}^{(1,2)}$ are to be determined by boundary conditions.

Finally, I would like to mention some interesting properties of the spherical harmonic functions. In order to introduce these concepts we reexamine the angular function of the scalar wave equation. The spherical harmonic functions are the solution of the angular differential equation

$$-\left(\frac{1}{\sin \theta} \frac{\partial}{\partial \theta} \left(\sin \theta \frac{\partial}{\partial \theta} \right) + \frac{1}{\sin^2 \theta} \frac{\partial^2}{\partial \phi^2} \right) Y_{l,m}(\theta, \phi) = l(l+1) Y_{l,m}(\theta, \phi) \quad (\text{A.10})$$

As it is well-known in the quantum mechanics this equation can be written in the following form

$$\widehat{L}^2 Y_{l,m}(\theta, \phi) = l(l+1) Y_{l,m}(\theta, \phi) \quad (\text{A.11})$$

where $\widehat{L} = \frac{1}{i} \mathbf{r} \times \nabla$ is \hbar^{-1} times the orbital angular momentum operator of mechanics. The components of \widehat{L} can be written conveniently in the combinations

$$\widehat{L}_+ = \widehat{L}_x + i\widehat{L}_y = e^{i\phi} \left(\frac{\partial}{\partial \theta} + i \cot \theta \frac{\partial}{\partial \phi} \right)$$

$$\begin{aligned}
\widehat{L}_- &= \widehat{L}_x - i\widehat{L}_y = e^{-i\phi} \left(-\frac{\partial}{\partial\theta} + i \cot\theta \frac{\partial}{\partial\phi} \right) \\
\widehat{L}_z &= -i \frac{\partial}{\partial\phi}
\end{aligned} \tag{A.12}$$

where \widehat{L}_\pm are the creation and annihilation operators, respectively. As is clear from equations (A.12), the orbital angular momentum operator acts only on the angular variables and is independent of r . It can be shown from the recursion relations for $Y_{l,m}(\theta, \phi)$ the following useful relations

$$\begin{aligned}
\widehat{L}_+ Y_{l,m}(\theta, \phi) &= \sqrt{(l-m)(l+m+1)} Y_{l,m+1}(\theta, \phi) \\
\widehat{L}_- Y_{l,m}(\theta, \phi) &= \sqrt{(l+m)(l-m+1)} Y_{l,m-1}(\theta, \phi) \\
\widehat{L}_z Y_{l,m}(\theta, \phi) &= m Y_{l,m}(\theta, \phi).
\end{aligned} \tag{A.13}$$

Appendix B

Integrals containing confluent hypergeometric functions

The confluent hypergeometric and hypergeometric function are defining by the following series

$$\begin{aligned} {}_1F_1(\alpha; \gamma; z) &= 1 + \frac{\alpha}{\gamma} \frac{z}{1!} + \frac{\alpha(\alpha+1)}{\gamma(\gamma+1)} \frac{z^2}{2!} + \dots \\ {}_2F_1(\alpha, \beta; \gamma; z) &= 1 + \frac{\alpha\beta}{\gamma} \frac{z}{1!} + \frac{\alpha(\alpha+1)\beta(\beta+1)}{\gamma(\gamma+1)} \frac{z^2}{2!} + \dots \end{aligned} \quad (\text{B.1})$$

which converges for all finite z ; α , β and γ are arbitrary parameters, of course γ must not be zero or negative integer numbers. The hypergeometric functions also have integral representations:

$$\begin{aligned} {}_1F_1(\alpha, \gamma; z) &= -\frac{1}{2\pi i} \frac{\Gamma(1-\alpha)\Gamma(\gamma)}{\Gamma(\gamma-\alpha)} \oint_{C'} e^{tz} (-t)^{\alpha-1} (1-t)^{\gamma-\alpha-1} dt \\ {}_2F_1(\alpha, \beta; \gamma; z) &= -\frac{1}{2\pi i} \frac{\Gamma(1-\alpha)\Gamma(\gamma)}{\Gamma(\gamma-\alpha)} \oint_{C'} \frac{e^{tz} (-t)^{\alpha-1} (1-t)^{\gamma-\alpha-1}}{(1-tz)^\beta} dt \end{aligned} \quad (\text{B.2})$$

where $\Gamma(x)$ is the Gamma function [42] and C' is a contour around origin and passes through point $+1$ on the real axis. However, for calculations of Hypergeometric-Gaussian type I and II modes, the following integrals will appear:

1. $J_{\alpha, \gamma}^\nu = \int_0^\infty e^{-\lambda z} z^\nu {}_1F_1(\alpha, \gamma, \kappa z) dz$

This integral will be converge if $\Re(\nu) > -1$ and $\Re(\lambda) > |\Re(\kappa)|$ (for negative α , the last condition can be replaced by $\Re(\lambda) > 0$). Replacing the integral relation

of hypergeometric function into equation we will get the following integral

$$\begin{aligned}
J_{\alpha,\gamma}^{\nu} &= \int_0^{\infty} e^{-\lambda z} z^{\nu} {}_1F_1(\alpha, \gamma, \kappa z) dz \\
&= -\frac{1}{2\pi i} \frac{\Gamma(1-\alpha)\Gamma(\gamma)}{\Gamma(\gamma-\alpha)} \oint_{C'} \int_0^{\infty} e^{-(\lambda-\kappa t)z} z^{\nu} (-t)^{\alpha-1} (1-t)^{\gamma-\alpha-1} dt dz \\
&= -\frac{1}{2\pi i} \frac{\Gamma(1-\alpha)\Gamma(\gamma)}{\Gamma(\gamma-\alpha)} \lambda^{-\nu-1} \Gamma(\nu+1) \oint_{C'} (-t)^{\alpha-1} (1-t)^{\gamma-\alpha-1} (1-\kappa t/\lambda)^{-\nu-1} dt \\
&= \Gamma(\nu+1) \lambda^{-\nu-1} {}_2F_1\left(\alpha, \nu+1, \gamma, \frac{\kappa}{\lambda}\right)
\end{aligned} \tag{B.3}$$

which I use equation (B.2) on the last simplification. There is an interesting case: where the function ${}_2F_1\left(\alpha, \nu+1, \gamma, \frac{\kappa}{\lambda}\right)$ reduces to a polynomial the integral $J_{\alpha,\gamma}^{\nu}$ can be expressed in terms of elementary functions

$$J_{\alpha,\gamma}^{\gamma+n-1} = (-1)^n \Gamma(\gamma) \frac{d^n}{d\lambda^n} (\lambda^{\alpha-\gamma} (\lambda-\kappa)^{-\alpha}) \tag{B.4}$$

$$2. J = \int_0^{\infty} e^{-\lambda z} z^{\gamma-1} {}_1F_1(\alpha, \gamma, \kappa z) {}_1F_1(\alpha', \gamma, \kappa' z) dz$$

In order to find the analytical solution for this integral. we must replace one of the confluent hypergeometric function with its integral representation equation (B.2). So, we will get the following expression

$$\begin{aligned}
J &= \int_0^{\infty} e^{-\lambda z} z^{\gamma-1} {}_1F_1(\alpha, \gamma, \kappa z) {}_1F_1(\alpha', \gamma, \kappa' z) dz \\
&= -\frac{1}{2\pi i} \frac{\Gamma(1-\alpha')\Gamma(\gamma)}{\Gamma(\gamma-\alpha')} \oint_{C'} \int_0^{\infty} (-t)^{\alpha'-1} (1-t)^{\gamma-\alpha'-1} z^{\gamma-1} e^{-z(\lambda-\kappa't)} {}_1F_1(\alpha, \gamma, \kappa z) dz dt \\
&= -\frac{1}{2\pi i} \frac{\Gamma(1-\alpha')\Gamma(\gamma)^2}{\Gamma(\gamma-\alpha')^2} \oint_{C'} \frac{(-t)^{\alpha'-1} (1-t)^{\gamma-\alpha'-1} (\lambda-\kappa't)^{\alpha-\gamma}}{(\lambda-\kappa't-\kappa)^{\alpha}} {}_1F_1(\alpha, \gamma, \kappa z) dt \\
&= \Gamma(\gamma) \lambda^{\alpha+\alpha'-\gamma} (\lambda-\kappa)^{-\alpha} (\lambda-\kappa')^{-\alpha'} {}_2F_1\left(\alpha; \alpha'; \gamma, \frac{\kappa\kappa'}{(\lambda-\kappa)(\lambda-\kappa')}\right)
\end{aligned} \tag{B.5}$$

where we have used equation (B.2).

Appendix C

Published articles related to my thesis

1. **E. Karimi**, B. Piccirillo, L. Marrucci, and E. Santamato, **Hypergeometric-Gaussian modes**, *Optics Letters*, **32**, 3053-3055, (2007).
2. **E. Karimi**, B. Piccirillo, L. Marrucci, and E. Santamato. **Improved focusing with Hypergeometric-Gaussian type-II optical modes**, *Optics Express*, **16**, 21069-21075, (2008).
3. **E. Karimi**, B. Piccirillo, L. Marrucci, and E. Santamato, **Light propagation in a birefringent plate with topological charge**, *Optics Letters*, **34**, 1225, (2009)
4. **E. Karimi**, B. Piccirillo, E. Nagali, L. Marrucci, and E. Santamato, **Efficient generation and sorting of orbital angular momentum eigenmodes of light by thermally tuned q-plates**, *Applied Physics Letters*, **94**, 231124, (2009)
5. E. Nagali, F. Sciarrino, F. De Martini, L. Marrucci, B. Piccirillo, **E. Karimi**, and E. Santamato, **Quantum information transfer from spin to orbital angular momentum of photons**, *Physical Review Letters*, **103**, 013601, (2009).
6. E. Nagali, F. Sciarrino, L. Sansoni, F. De Martini, L. Marrucci, B. Piccirillo, **E. Karimi**, E. Santamato, **Quantum interference by coherence transfer from spin to orbital angular momentum of photons**, *Proceedings of SPIE The International Society for Optical Engineering*, **7355**, 735507 (2009).
7. E. Nagali, F. Sciarrino, F. De Martini, B. Piccirillo, **E. Karimi**, L. Marrucci, and E. Santamato, **Polarization control of single photon quantum orbital angular momentum states**, *Optics Express*, **17**, 18745, (2009)

8. S. Slussarenko, **E. Karimi**, B. Piccirillo, L. Marrucci, and E. Santamato, **Universal unitary gate for single-photon spin-orbit four-dimensional states**, *Physical Review A*, **80**, 022326, (2009)
9. L. Marrucci, E. Nagali, F. Sciarrino, L. Sansoni, F. De Martini, B. Piccirillo, **E. Karimi**, and E. Santamato, **Photonic quantum information applications of patterned liquid crystals**, *Molecular Crystals and Liquid Crystals*, **in press**, (2009).
10. E. Nagali, L. Sansoni, F. Sciarrino, F. De Martini, L. Marrucci, B. Piccirillo, **E. Karimi**, and E. Santamato, **Optimal quantum cloning of orbital angular momentum qubits via Hong-Ou-Mandel coalescence**, *Nature Photonics*, **3**, 7xx, (2009).

Bibliography

- [1] R. Feynman, R. Leighton, and M. Sands. *The Feynman Lectures on Physics*. Addison Wesley, USA, 1964.
- [2] J. D. Jackson. *Classical Electrodynamics*. John Wiley, New York, 1999.
- [3] J. H. Poynting. On the transfer of energy in the electromagnetic field. *Phil. Trans. Roy. Soc. (London)*, 175:343, 1884.
- [4] L. Mandel and E. Wolf. *Optical Coherence and Quantum Optics*. Cambridge University Press, Cambridge, 1995.
- [5] R. A. Beth. Mechanical detection and measurement of the angular momentum of light. *Physical Review*, 50:115, 1936. URL <http://link.aps.org/doi/10.1103/PhysRev.50.115>.
- [6] M. V. Berry. Paraxial beams of spinning light. In *Singular optics (Ed, M. S. Soskin) Frunzenskoe, Crimea, SPIE*, 3487:6, 1998.
- [7] V. Garcés-Chávez, D. McGloin, M. J. Padgett, W. Dultz, H. Schmitzer, and K. Dholakia. Observation of the transfer of the local angular momentum density of a multiringed light beam to an optically trapped particle. *Physical Review Letters*, 91(9):093602, 2003. URL <http://link.aps.org/doi/10.1103/PhysRevLett.91.093602>.
- [8] C. López-Mariscal, J. C. Gutiérrez-Vega, G. Milne, and K. Dholakia. *Optics Express*, 14(9):4182, 2006. URL <http://www.opticsexpress.org/abstract.cfm?URI=oe-14-9-4182>.
- [9] F. Gori, G. Guattari, and C. Padovani. Bessel-gauss beams. *Optics Communication*, 64(6):491, 1987. URL <http://www.sciencedirect.com/science/article/B6TVF-46JGXM-25N/2/fca63398c5cc38a1ba818881aa02a91c>.
- [10] M. A. Bandres and J. C. Gutiérrez-Vega. Ince gaussian beams. *Optics Letters*, 29(2):144, 2004. URL <http://ol.osa.org/abstract.cfm?URI=ol-29-2-144>.

- [11] M. A. Bandres and J. C. Gutiérrez-Vega. Circular beams. *Optics Letters*, 33(2):177, 2008. URL <http://ol.osa.org/abstract.cfm?URI=ol-33-2-177>.
- [12] V. V. Kotlyar, R. V. Skidanov, S. N. Khonina, and V. A. Soifer. Hypergeometric modes. *Optics Letters*, 32(7):742–744, 2007. URL <http://ol.osa.org/abstract.cfm?URI=ol-32-7-742>.
- [13] E. Karimi, B. Piccirillo, L. Marrucci, and E. Santamato. Hypergeometric-gaussian modes. *Optics Letters*, 32(21):3053–3055, 2007. URL <http://ol.osa.org/abstract.cfm?URI=ol-32-21-3053>.
- [14] E. Karimi, B. Piccirillo, L. Marrucci, and E. Santamato. Improved focusing with hypergeometric-gaussian type-ii optical modes. *Optics Express*, 16(25):21069–21075, 2008. URL <http://www.opticsexpress.org/abstract.cfm?URI=oe-16-25-21069>.
- [15] L. Allen, M. W. Beijersbergen, R. J. C. Spreeuw, and J. P. Woerdman. Orbital angular momentum of light and the transformation of laguerre-gaussian laser modes. *Physical Review A*, 110(11):8185, 1992. URL <http://link.aps.org/10.1103/PhysRevA.45.8185>.
- [16] A. E. Siegman. *Lasers*. Mill Valley, California, 1986.
- [17] M. W. Beijersbergen, R. P. C. Coerwinkel, M. Kristensen, and J. P. Woerdman. Helical-wavefront laser beams produced with a spiral phaseplate. *Optics Communication*, 112(5-6):321, 1994. URL [http://dx.doi.org/10.1016/0030-4018\(94\)90638-6](http://dx.doi.org/10.1016/0030-4018(94)90638-6).
- [18] V. Y. Bazhenov, M. V. Vasnetsov, and M. S. Soskin. Screw dislocations in light wavefronts. *JETP Letts*, 52:429, 1990.
- [19] L. Marrucci, C. Manzo, and D. Paparo. Optical spin-to-orbital angular momentum conversion in inhomogeneous anisotropic media. *Physical Review Letters*, 96(16):163905, 2006. URL <http://link.aps.org/abstract/PRL/v96/e163905>.
- [20] N. R. Heckenberg, R. McDuff, C. P. Smith, H. Rubinsztein-Dunlop, and M. J. Wegener. Laser beams with phase singularities. *Optical and Quantum Electronics*, 24:S951, 1992. URL <http://www.springerlink.com/content/w27u43014g106286>.
- [21] M V Berry. Optical vortices evolving from helicoidal integer and fractional phase steps. *Journal of Optics A: Pure and Applied Optics*, 6(2):259, 2004. URL <http://stacks.iop.org/1464-4258/6/i=2/a=018>.

- [22] S. Sato, M. Ishigure, and H. Inaba. Optical trapping and rotational manipulation of microscopic particles and biological cells using higher-order mode nd:yag laser beams. *Electronics Letters*, 27(20):1831, 1991.
- [23] E. Higurashi, H. Ukita, H. Tanaka, and O. Ohguchi. Optically induced rotation of anisotropic micro-objects fabricated by surface micromachining. *Applied Physics Letters*, 15(17):5521, 1994. URL <http://link.aip.org/link/?APL/64/2209/1>.
- [24] A. T. O’Neil, I. MacVicar, L. Allen, and M. J. Padgett. Intrinsic and extrinsic nature of the orbital angular momentum of a light beam. *Phys. Rev. Lett.*, 88(5):053601, 2002. URL <http://link.aip.org/link/?APL/64/2209/1>.
- [25] J. Leach, H. Mushfique, R. di Leonardo, M. J. Padgett, and J. Cooper. An optically driven pump for microfluidics. *Lab on a Chip*, 6(6):735, 2006. URL <http://dx.doi.org/10.1039/b601886f>.
- [26] G. Gibson, J. Courtial, M. J. Padgett, M. Vasnetsov, V. Pas’ko, S. Barnett, and S. Franke-Arnold. Free-space information transfer using light beams carrying orbital angular momentum. *Optics Express*, 12(22):5448, 2004. URL <http://www.opticsexpress.org/abstract.cfm?URI=oe-12-22-5448>.
- [27] A. Aspect, P. Grangier, and G. Roger. Experimental tests of realistic local theories via bell’s theorem. *Physical Review Letters*, 47(7):460, 1981. URL <http://link.aps.org/doi/10.1103/PhysRevLett.47.460>.
- [28] D. Boschi, S. Branca, F. De Martini, L. Hardy, and S. Popescu. Experimental realization of teleporting an unknown pure quantum state via dual classical and einstein-podolsky-rosen channels. *Physical Review Letters*, 80(6):1121, 1998. URL <http://link.aps.org/doi/10.1103/PhysRevLett.80.1121>.
- [29] D. Bouwmeester, J. W. Pan, K. Mattle, M. Eibl, H. Weinfurter, and A. Zeilinger. Experimental quantum teleportation. *Nature*, 390(6660):575, 1997. URL <http://dx.doi.org/10.1038/37539>.
- [30] A. V. Sergeenko. *Quantum Communications and Cryptography*. Taylor and Francis Group, Washington, 2006.
- [31] A. Mair, A. Vaziri, G. Welhs, and A. Zeilinger. Entanglement of the angular momentum states of photons. *Nature*, 412(6844):313, 2001. URL <http://dx.doi.org/10.1038/35085529>.
- [32] J. Leach, B. Jack, J. Romero, M. Ritsch-Martel, R. W. Boyd, A. K. Jha, S. M. Barnett, S. Franke-Arnold, and M. J. Padgett. Violation of a bell inequality in two-dimensional orbital angular momentum state-spaces. *Optics Express*,

- 17(10):8287, 2009. URL <http://www.opticsexpress.org/abstract.cfm?URI=oe-17-10-8287>.
- [33] E. Nagali, F. Sciarrino, F. De Martini, L. Marrucci, B. Piccirillo, E. Karimi, and E. Santamato. Quantum information transfer from spin to orbital angular momentum of photons. *Physical Review Letters*, 103(1):013601, 2009. URL <http://link.aps.org/abstract/PRL/v103/e013601>.
- [34] E. Nagali, L. Sansoni, F. Sciarrino, F. De Martini, L. Marrucci, B. Piccirillo, E. Karimi, and E. Santamato. Optimal quantum cloning of orbital angular momentum qubits via hong-ou-mandel coalescence. *Nature Photonics*, 3(12):7xx, 2009. URL <http://dx.doi.org/10.1038/nphoton.2008.127>.
- [35] C. J. Bouwkamp and H. B. G. Casimir. *Physica*, 20:539, 1954.
- [36] C. Morette De Witt and J. H. D. Jensen. *Z Naturforsch*, 8a:267, 1953.
- [37] C. Cohen-Tannoudji, J. Dupont-Roc, and G. Grynberg. *Photons and Atoms: An Introduction to Quantum Electrodynamics*. John Wiley, New York, 1989.
- [38] E. Santamato. Photon orbital angular momentum: problems and perspectives. *Fortschritte der Physik*, 52(11-12):1141, 2004. URL <http://dx.doi.org/10.1002/prop.200410184>.
- [39] J. H. Crichton and P. L. Marston. The measurement distinction between the spin and orbital angular momenta of electromagnetic radiation. *Mathematical Physics and Quantum Field Theory*, 4:37, 2000.
- [40] J. Humblet. Sur le moment d'impulsion d'une onde electromagnetique. *Physica (Utrecht)*, 10:585, 1943.
- [41] L. Allen, S. M. Barnett, and M. J. Padgett. *Optical angular momentum*. Institute of Physics Publishing, Bristol, 2003.
- [42] M. Abramowitz and I. A. Stegun. *Handbook of Mathematical Functions With Formulas, Graphs, and Mathematical Tables*. National Bureau of Standards, Washington, 1972.
- [43] S. M. Barnett and L. Allen. Orbital angular momentum and non-paraxial light beams. *Optics Communication*, 110(5-6):670, 2004. URL <http://www.sciencedirect.com/science/article/B6TVF-46DFXF7-12J/2/03d46903df939ab0d7bdc567f4e78e17>.
- [44] L. Marrucci, C. Manzo, and D. Paparo. Pancharatnam-berry phase optical elements for wave front shaping in the visible domain: Switchable helical mode generation.

- Applied Physics Letters*, 88(22):221102, 2006. URL <http://link.aip.org/link/?APL/88/221102/1>.
- [45] Jr. G. A. Swartzlander. Peering into darkness with a vortex spatial filter. *Optics Letters*, 24(8):497, 2001. URL <http://ol.osa.org/abstract.cfm?URI=ol-26-8-497>.
- [46] E. Karimi, B. Piccirillo, E. Nagali, L. Marrucci, and E. Santamato. Efficient generation and sorting of orbital angular momentum eigenmodes of light by thermally tuned q-plates. *Applied Physics Letters*, 94(23):231124, 2009. URL <http://link.aip.org/link/?APL/94/231124/1>.
- [47] L. Marrucci. Generation of helical modes of light by spin-to-orbital angular momentum conversion in inhomogeneous liquid crystals. *Molecular Crystals and Liquid Crystals*, 488:148, 2008. URL <http://www.informaworld.com/10.1080/15421400802240524>.
- [48] E. Karimi, B. Piccirillo, L. Marrucci, and E. Santamato. Light propagation in a birefringent plate with topological charge. *Optics Letters*, 34(8):1225, 2009. URL <http://ol.osa.org/abstract.cfm?URI=ol-34-8-1225>.
- [49] G. F. Calvó and A. Picon. Spin-induced angular momentum switching. *Optics Letters*, 32(7):838–840, 2007. URL <http://ol.osa.org/abstract.cfm?URI=ol-32-7-838>.
- [50] M. Born and E. Wolf. *Principles of Optics*. Cambridge University Press, Cambridge, 1999.
- [51] M. J. Padgett and J. Courtial. Poincaré-sphere equivalent for light beams containing orbital angular momentum. *Optics Letters*, 24(7):430, 1999. URL <http://ol.osa.org/abstract.cfm?URI=ol-24-7-430>.
- [52] R. Simon and N. Mukunda. Minimal three-component $su(2)$ gadget for polarization optics. *Physics Letters A*, 143:165, 1990. URL [http://dx.doi.org/10.1016/0375-9601\(90\)90732-4](http://dx.doi.org/10.1016/0375-9601(90)90732-4).
- [53] R. Bhandari and T. Dasgupta. A spin-1/2 interferometer using light beams. *Physics Letters A*, 143(4-5):170, 1990. URL <http://www.sciencedirect.com/science/article/B6TVM-46SNP3G-1W2/2/48e2f1aa85c10684cfa59588d6c4b883>.
- [54] E. Karimi, S. Slussarenko, B. Piccirillo, L. Marrucci, and E. Santamato. Polarization-controlled evolution of light transverse modes and associated Pancharatnam geometric phase in orbital angular momentum. *Submitted*, 2009. URL <http://arxiv.org/abs/0909.2768v1>.

- [55] M. Fiorentino and F. N. C. Wong. Deterministic controlled-not gate for single-photon two-qubit quantum logic. *Physical Review Letters*, 93:070502, 2004. URL <http://link.aps.org/doi/10.1103/PhysRevLett.93.070502>.
- [56] S. Pancharatnam. *Collected works of S. Pancharatnam*. Oxford University Press, Oxford, 1975.
- [57] E. J. Galvez, P. R. Crawford, H. I. Sztul, M. J. Pysher, P. J. Haglin, and R. E. Williams. Geometric phase associated with mode transformations of optical beams bearing orbital angular momentum. *Physical Review Letters*, 90(20):203901, 2003. URL <http://link.aps.org/doi/10.1103/PhysRevLett.90.203901>.
- [58] R. Bhandari. Polarization of light and topological phases. *Physics Report*, 281:1, 1997. URL [http://dx.doi.org/10.1016/S0370-1573\(96\)00029-4](http://dx.doi.org/10.1016/S0370-1573(96)00029-4).
- [59] B. Richards and E. Wolf. Electromagnetic diffraction in optical systems. ii. structure of the image field in an aplanatic system. *Proceedings of the Royal Society of London. Series A. Mathematical and Physical Sciences*, 253(1274):358, 1959. URL <http://rspa.royalsocietypublishing.org/content/253/1274/358.abstract>.
- [60] K. Youngworth and T. Brown. Properties of circularly polarized vortex beams. *Optics Express*, 7(2):77, 2000. URL <http://www.opticsexpress.org/abstract.cfm?URI=oe-7-2-77>.
- [61] R. Dorn, S. Quabis, and G. Leuchs. Sharper focus for a radially polarized light beam. *Physical Review Letters*, 91:233901, 2003. URL <http://link.aps.org/doi/10.1103/PhysRevLett.91.233901>.
- [62] Q. Zhan. Properties of circularly polarized vortex beams. *Optics Letters*, 31(7):867, 2006. URL <http://ol.osa.org/abstract.cfm?URI=ol-31-7-867>.
- [63] H. Wang, L. Shi, B. Lukyanchuk, C. Sheppard, and C. T. Chong. Creation of a needle of longitudinally polarized light in vacuum using binary optics. *Nature Photonics*, 2(8):501, 2008. URL <http://dx.doi.org/10.1038/nphoton.2008.127>.
- [64] H. Wang, L. Shi, G. Yuan, X. S. Miao, W. Tan, and T. Chong. Subwavelength and super-resolution nondiffraction beam. *Applied Physics Letters*, 89(17):171102, 2006. URL <http://link.aip.org/link/?APL/89/171102/1>.
- [65] S. Slussarenko, E. Karimi, B. Piccirillo, L. Marrucci, and E. Santamato. Efficient generation and control of higher order orbital angular momentum states for classical and quantum communication process. *submitted*, 2009.
- [66] V. Karimipour, A. Bahraminasab, and S. Bagherinezhad. *Physical Review A*, 65(2):042320, 2002. URL <http://link.aps.org/doi/10.1103/PhysRevA.65.042320>.

- [67] E. Nagali, F. Sciarrino, F. De Martini, B. Piccirillo, E. Karimi, L. Marrucci, and E. Santamato. Polarization control of single photon quantum orbital angular momentum states. *Optics Express*, 17(21):18745, 2009. URL <http://www.opticsexpress.org/abstract.cfm?URI=oe-17-21-18745>.
- [68] S. Slussarenko, E. Karimi, B. Piccirillo, L. Marrucci, and E. Santamato. Universal unitary gate for single-photon spin-orbit four-dimensional states. *Physical Review A*, 80(2):022326, 2009. URL <http://link.aps.org/abstract/PRA/v80/e022326>.
- [69] N. K. Langford, R. B. Dalton, M. D. Harvey, J. L. O'Brien, G. J. Pryde, A. Gilchrist, S. D. Bartlett, and A. G. White. Measuring entangled qutrits and their use for quantum bit commitment. *Physical Review Letters*, 93(5):053601, 2004. URL <http://link.aps.org/10.1103/PhysRevLett.93.053601>.
- [70] P.G. Kwiat, K. Mattle, H. Weinfurter, A. Zeilinger, A.V. Sergienko, and Y.H. Shih. New high-intensity source of polarization-entangled photon pairs. *Physical Review Letters*, 75(24):4337, 1995. URL <http://link.aps.org/10.1103/PhysRevLett.75.4337>.
- [71] C. K. Hong, Z. Y. Ou, and L. Mandel. Measurement of subpicosecond time intervals between two photons by interference. *Physical Review Letters*, 59(18):2044, 1987. URL <http://link.aps.org/10.1103/PhysRevLett.59.2044>.
- [72] M. Ricci, F. Sciarrino, C. Sias, and F. De Martini. Teleportation scheme implementing the universal optimal quantum cloning machine and the universal not gate. *Physical Review Letters*, 92(4):047901, 2004. URL <http://link.aps.org/10.1103/PhysRevLett.92.047901>.